Uncertainty Quantification and Sensitivity Analyses of the Nonlinear Behavior of Heterogeneous Material Microstructures: Applications to Dynamic Response of Energetic Materials and Cyclic Response of a Titanium Alloy

By

Xiaoyu Zhang

Dissertation

Submitted to the Faculty of the

Graduate School of Vanderbilt University

in partial fulfillment of the requirements

for the degree of

DOCTOR OF PHILOSOPHY

in

Civil Engineering

January 31, 2021

Nashville, Tennessee

Approved:

Caglar Oskay, Ph.D.

Prodyot K. Basu, Ph.D.

Sankaran Mahadevan, Ph.D.

Ravindra Duddu, Ph.D.

Haoxiang Luo, Ph.D.

To my family

ACKNOWLEDGMENTS

First of all, I would like to express my great gratitude to my advisor Dr. Caglar Oskay. Without him, it is impossible to finish my dissertation. His vision, critical thinking and enthusiasm definitely influenced me on both my research attitude and future career. Dr. Oskay has always been supportive, patient and encouraging, and these enlightening conversations we had change the way I find, analyze and solve problems. I sincerely thank my advisor Dr. Oskay for his mentorship over the past five and half years. I also would like to thank my committee members Dr. Haoxiang Luo, Dr. Prodyot K. Basu, Dr. Ravindra Duddu and Dr. Sankaran Mahadevan for their valuable guiding on this research work.

I thank all my research group members in Multiscale Computational Mechanics Laboratory (MCML) for being along with me during the challenging and inspiring journey of PhD study. Especially, I would like to acknowledge Dr. Xiang Zhang, Dr. Ruize Hu, Dr. Shuhai Zhang, Dr. Yang Liu and Mrs. Wendy Paulson for their help in valuable research ideas and technical issues. I thank my friend Guangtao Nie, Shiyuan Zhang, Tianyao Zhang for the help we have on study and life, especially in the first two year of my Ph.D. studies.

Last but not least, I would like to express the deepest appreciation to my parents, Baozhi Zhang and Tong Zhang, for always being my backup and encouraging me whenever I need it. Their love give me the strength to go through the journey, and I am so lucky to be their son. I also want to thank my beautiful girlfriend, Wen Wen, for her companion and support in the past two years.

Finally, I acknowledge the financial support of the Air Force Office of Scientific Research, Dynamic materials and Interactions program (Grant No.: FA9550- 15-1-0202), and the financial support of the National Aeronautics and Space Administration, Space Technology Research Grants (Early State Innovation Grant No.: 80NSSC20K0294). I also acknowledge the teaching assistantship offered by the Department of Civil and Environmental Engineering.

TABLE OF CONTENTS

Page

DEDICATION iii

ACKNOWLEDGMENTS iv

1 INTRODUCTION 1

1.1 Background and Motivation 1

1.1.1 Case 1: Probabilistic Analysis of the Nonlinear Dynamic Response of Energetic Materials 2

1.1.1.1 Material Parameter Sensitivity Analysis for Energetic Materials 2

1.1.1.2 Machine-Learning Based Probabilistic Analysis Framework 3

1.1.2 Case 2: Probabilistic Analyses of the Fatigue Nucleation Behavior of a Titanium Alloy Subjected to Cyclic Loads 5

1.2 Dissertation Organization 5

2 MATERIAL AND MORPHOLOGY PARAMETER SENSITIVITY ANALYSIS IN PARTICULATE COMPOSITE MATERIALS 7

2.1 Introduction 7

2.2 Microcale Modeling of the AP-HTPB system 7

2.2.1 Binder Constitutive Model 8

2.2.2 Interface Constitutive Model 10

2.2.3 Microscale Geometry 12

2.3 Sensitivity Analysis Framework 13

2.3.1 Stratified Sampling 15

2.3.2 Gaussian Process Model 15
2.3.3 Discontinuities and Classifier 19
2.3.4 Global Sensitivity Analysis 22
2.3.4.1 Decomposition of Variance 23
2.3.4.2 Sensitivity Index 23
2.4 Numerical Examples 25
2.4.1 Material Property Sensitivity 25
2.4.1.1 microscale Model 25
2.4.1.2 Local GP Models and Classifier 29
2.4.1.3 Global Sensitivity Analysis 31
2.4.2 Microscale Geometry Sensitivity 32
2.4.2.1 Microscale Model 33
2.4.2.2 GP Surrogate Model 36
2.4.2.3 Global Sensitivity Analysis 37
2.5 Conclusion 39

3 PLASTIC DISSIPATION SENSITIVITY TO MECHANICAL PROPERTIES IN POLYCRYSTALLINE β-HMX SUBJECTED TO IMPACT LOADING 41
3.1 Introduction 41
3.2 Constitutive Model of β-HMX 41
3.2.1 CPFE formulation 42
3.2.2 Monoclinic lattice and elasticity 43
3.2.3 Flow rule and evolution laws 45
3.3 Model Verification 48
3.3.1 Parameter calibration 49
3.3.2 Verification study 51
3.4 Sensitivity Analyses 53
3.4.1 Parameters subspace 54

3.4.1.1 Elastic coefficients ranges 54
3.4.1.2 Plastic deformation properties 55
3.4.2 Single crystal sensitivity analysis 56
3.4.2.1 Elasticity coefficients 56
3.4.2.2 Plastic deformation mechanisms 58
3.4.3 Polycrystalline sensitivity analysis 61
3.4.3.1 Elasticity coefficients 63
3.4.3.2 Plastic deformation mechanisms 65
3.5 Conclusion 68
3.6 Appendix: Tensor of elastic moduli 69

4 MODELING AND NUMERICAL INVESTIGATION OF MECHANICAL TWINNING IN β-HMX CRYSTALS SUBJECTED TO SHOCK LOADING 71
4.1 Introduction 71
4.2 Constitutive Model of β-HMX 72
4.2.1 Anisotropic elasticity 74
4.2.2 Mechanical twinning model 77
4.2.3 Dislocation slip evolution 79
4.3 Parameter Calibration 80
4.3.1 Elasticity 80
4.3.2 Dislocation slip parameters 82
4.3.3 Twinning parameters 83
4.4 Analysis of twin evolution 86
4.4.1 Single crystal configuration 86
4.4.1.1 Effect of crystal orientation 86
4.4.1.2 Effect of impact velocity 89
4.4.2 Polycrystal configurations 90
4.4.2.1 Microscale structures 90

4.4.2.2 Loading velocity 94
4.5 Conclusion 96
4.5.1 General Remarks 98
4.5.2 Pressure Dependence of Elastic Moduli 99
4.5.3 Constitutive Integration Scheme 100
4.5.3.1 Evolution of target variables 100
4.5.4 Discretization 102

5 UNCERTAINTY QUANTIFICATION FOR FATIGUE NUCLEATION OF TITANIUM ALLOY MICROSTRUCTURE 107
5.1 Introduction 107
5.2 Uncertainty Quantification Framework 107
5.3 Sparse DD-EHM Model 112
5.3.1 Reduced Order Model 113
5.3.2 Dislocation Density Based Crystal Plasticity 115
5.4 Microscale Structure 117
5.4.1 SVE Morphology 117
5.4.2 Numerical Settings 121
5.4.2.1 Model Parameters 121
5.4.2.2 Load and Boundary Conditions 122
5.4.2.3 FNP and Motion Preditions 124
5.5 Fatigue Nucleation Prediction With Uncertainty 124
5.5.1 SVE ensemble size 124
5.5.2 Evolution of Dislocation Density Discrepancy 127
5.5.3 Critical Strength Distribution 129
5.6 Conclusion 132

6 Conclusion 134

BIBLIOGRAPHY 136

LIST OF TABLES

Table Page

2.1 Confusion matrix. 22

2.2 Binder and particle fixed parameters. 27

2.3 Parameter boundaries in material property sensitivity study. 28

2.4 Interfacial fixed parameters 28

2.5 Overall accuracies of classifiers 29

2.6 Parameters boundary in microscale geometry sensitivity study. 35

2.7 Fixed parameters in microscale geometry sensitivity study. 36

2.8 Calibrated six pairs of prony series. 36

3.1 Slip strength ratios. 49

3.2 Flow rule and hardening rule parameters. 49

3.3 Specimen and load configurations. 52

3.4 Parameter ranges of elasticity coefficients (unit: GPa). 55

3.5 Ranges for the plastic parameters. 56

4.1 Parameters of the elasticity model. 81

4.2 Slip strength ratios. 83

4.3 Twinning parameters. 85

5.1 Morphology parameters. 121

5.2 Slip system of HCP and BCC. 122

5.3 Flow rule parameters for HCP and BCC crystals. 122

5.4 Hardening rule parameters. 123

LIST OF FIGURES

Figure Page

2.1 Problem setting: microscale geometry and loading. 8

2.2 Shapes with different sphericity. 13

2.3 Overview of the proposed sensitivity analysis framework. 14

2.4 Comparison between stratified sampling and uniform sampling. 16

2.5 Example of GP model and discontinuity. Illustration of (a) a GP surrogate of function, $f = x \cdot \sin(x)$ trained with 6 training points; (b) a GP surrogate of function, $f = x \cdot \sin(x) + 5 \cdot H(x-5)$ trained with 6 samples; (c) two local GP surrogates of function, $f = x \cdot \sin(x) + 5 \cdot H(x-5)$ trained with 6 samples. 17

2.6 Cross-validation of the classification algorithm. 21

2.7 Dynamic response of a single AP particle reinforced HTPB. (a) The geometry and boundary conditions; (b) the loading history. 26

2.8 Prony series ranges calibration with experimental data. 27

2.9 Von Mises stress contours of single particle system failure at (a) $t = 1.04$ ms; (b) $t = 2.12$ ms; (c) $t = 3.08$ ms; (d) $t = 3.932$ ms. 30

2.10 Convergence study of GP model with respect to (a) the number of training samples with prediction distributions generated with 2 million samples; and (b) the number of prediction points with the surrogate trained with 5120 samples. 31

2.11 Confusion matrix. Class i: separation initiation near the ith step load (i $\leq$ 4). Class 5: no separation ovserved. (a) confusion matrix trained with 512 samples. (b) confusion matrix trained with 5120 samples. 32

2.12 Convergence study of GP model with respect to (a) the number of training samples with prediction distributions generated with 20 million samples; and (b) the number of prediction points with the surrogate trained with 5120 samples. 33

2.13 Geometry and loading conditions. 33

2.14 Illustration of particle size distribution. Above PDF is subjected to a bimodal distribution with $\mu_1 = 0.15$ mm^2, $\mu_2 = 0.07$ mm^2, $\sigma_1 = 0.025$ mm^2, $\sigma_2 = 0.0075$ mm^2, $w_1 = 0.6$. 34

2.15 Examples of microscale geometry with size and shape parameters at (a) lower boundaries; (b) mean values; (c) upper boundaries in Table 2.6. 35

2.16 Prony Series Calibration 37

2.17 Mesh convergence study of the representative case. (a) Mesh of the representative microstructure with 21104 elements; (b) Element number convergence. 38

2.18 Example of microscale FE simulations of multiple particle systems. (a) Temperature contour of binder at $t = 10$ ms; (b) Von Mises stress contour at $t = 10$ ms. . . 39

2.19 Convergence study of GP model with respect to (a) the number of training samples with prediction distributions generated with 40 million samples; (b) the number of prediction points with the surrogate trained with 128 samples. 40

2.20 Convergence study of GP model with respect to (a) the number of training samples with prediction distributions generated with 45 million samples; and (b) the number of prediction points with the surrogate trained with 5120 samples. 40

3.1 Schematic example of polycrystal β-HMX. x_G, y_G and z_G represent the global coordinates, while x_L, y_L and z_L represent the local coordinates. y_L axis is chosen as the unique axis (parallel to $\boldsymbol{b}$) in the monoclinic lattice structure with $\alpha = \gamma = 90^\circ$, $\beta \neq 90^\circ$. The transformation between local coordinates and global coordinates is through Euler angles (Kocks convention). 43

3.2 Transition between the dominant slip mechanisms using the power-law function $h(\tau^\alpha)$. Dislocation density is of 0.0307 micro-m^{-2} in the illustration. The lines with "$\times\times\times$", "$\circ\circ\circ$", and "$----$" represent the total shear strain rate with ζ equal to 20, 50 and 150, respectively. 47

3.3 Hardening rate-stress curve at constant strain rate 2000 s^{-1}. The hardening rate is estimated by the finite difference method, where the stress and strain data are extracted from experimental measurements by Gray et al. [52] at room temperature. 50

3.4 Stress-strain curves at different temperatures for (a) HMX in (011) direction at the constant strain rate of 2000 s^{-1} predicted by the calibrated CPFE model, (b) experimentally observed behavior of Vanadium (experimental data from [173]) at the strain rate of 2500 s^{-1} and (c) experimentally observed behavior of PBX 9501 (experimental data from [52]) at the strain rate of 2000 s^{-1}. 50

3.5 Schematic representation of experimental setting. 51

3.6 Model verification with respect to loading in (a) the $(110)_{P2_1/n}$ direction; and (b) the $(011)_{P2_1/n}$ direction. 53

3.7 Summary of (a) sensitivity indices and (b) convergence for elastic coefficients in single crystal specimen. 57

3.8 Probability distributions for peak temperature resulting from the OAT analysis of individual elastic constants for single crystal cases. 58

3.9 Variation of peak temperature over (a) C_{44}-C_{23} plane and (b) n_1-n_2 plane for single crystal specimen. 58

3.10 Summary of (a) sensitivity indices and (b) convergence for plastic parameters in single crystal specimen. 59

3.11 Probability distribution for peak temperature resulting from the OAT analysis of individual plastic parameters for single crystal specimen. 60

3.12 Polycrystal specimen geometry. For the first normal distribution of particle size, $N(\mu_1, \sigma_1)$, the weight w=0.2, μ_1=61.8 micro-m, σ_1=13.9 micro-m. For the second normal distribution $N(\mu_2, \sigma_2)$, μ_2=225.7 micro-m, σ_2=44.9 micro-m. 61

3.13 Crystal orientation histogram for the specimen in Fig. 3.12. The x axis is the normalized angle range $(0 < \psi_1/(2\pi) < 1, 0 < \phi/\pi < 1, 0 < \psi_2/(2\pi) < 1)$. 62

3.14 Von Mises stress contours at (a) t =0.25 micro-s, (b) t =0.5 micro-s, (c) t =0.75 micro-s, and (d) t =1.0 micro-s. 62

3.15 Dislocation density contours at (a) t =0.25 micro-s, (b) t =0.5 micro-s, (c) t =0.75 micro-s, and (d) t =1.0 micro-s. 63

3.16 Summary of (a) sensitivity indices and (b) convergence for elastic parameters in polycrystal specimen. 64

3.17 Probability distributions for peak temperature resulting from the OAT analysis of individual elastic constants for polycrystal specimen. 64

3.18 Variation of peak temperature over (a) C_{44}-C_{23} plane and (b) n_1-n_3 plane for polycrystal cases. 65

3.19 Computation of the nonlocal peak temperature. The dots represent integration points within the specimen discretization. The circles represent the searching areas with the critical radii. The central point (marked as red in the electronic version of the manuscript) is the position where the nonlocal average is computed. 66

3.20 Maximum temperature-time curves with different critical radii. 66

3.21 Summary of (a) sensitivity indices and (b) convergence for plastic parameters in polycrystal specimen. 67

3.22 Probability distributions for peak temperature resulting from the OAT analysis of the individual plasticity parameters for polycrystal specimen. 68

4.1 Elasticity coefficients with pressure dependency for (a) the diagonal terms; and (b) the off-diagonal terms. 81

4.2 Model verification with respect to loading in (a) the $(110)_{P2_1/n}$ direction; and (b) the $(011)_{P2_1/n}$ direction. 84

4.3 Effect of twinning on model prediction. Particle velocity of shot 1168 is predicted using current model with twinning (dislocation slip and twin) and without twinning behavior (dislocation slip only). 86

4.4 Orientation dependency of resolved shear stress in (a) the $(110)_{P2_1/n}$ direction; and (b) the $(011)_{P2_1/n}$ direction. Temporal evolution of RSS is plotted at t=0.1 μs, 0.2 μs, 0.4 μs, 0.7 μs, 1.0 μs, 1.3 μs and 1.6 μs. Location x=0 mm represents the left hand side of the specimen, and x=4.66 mm represents the HMX/PMMA interface. . 87

4.5 Temporal evolution of twin volume fraction at loading (1) 200 m/s, and (2) 500 m/s. Loading is along (011) direction. 88

4.6 Twin volume fraction in single crystal at t=1.6 μs with loading velocity 50 m/s, 100 m/s, 200 m/s, 300 m/s, 400 m/s and 500 m/s. 89

4.7 Microstructures of polycrystal configuration. Each colored region represents a single crystal particle. Impact velocity is applied on the left hand side, and the movements of top, bottom, front and back faces are constraint in their normal directions. 91

4.8 Probabilistic distribution of twin volume fraction and non-zero twin volume fraction. The twinning accumulations are schematically presented at $f = 0.1$, $f = 0.2$, $f = 0.4$ and $f = 0.6$. 92

4.9 Twin volume fraction distribution of the microstructures with (a) randomized polygonal particle geometries and (b) regularized particle geometries, and maximum principal strain with (c) andomized polygonal particle geometries and (d) regularized particle geometries at t=1.6 μs. 93

4.10 Local region of twin concentration for microstructures with (1) randomized polygonal particle geometries and (2) regularized particle geometries at t=1.6 μs. Lattice axes $\boldsymbol{a}$, $\boldsymbol{b}$ and $\boldsymbol{c}$ for each grain are plotted as well. The lattice axes are not orthogonal due to the monoclinic lattice structure. 94

4.11 Maximum twin concentration discrepancy and misorientation in microstructures with (a) randomized polygonal particle geometries and (b) regularized particle geometries. Mean and standard deviation are computed in five intervals ((0°,45°), (45°,75°), (75°,105°), (105°,135°) and (135°,180°)). 95

4.12 Stress contour of microscale structure subjected to impact loading (a) 100 m/s at t=0.25 μs, (b) 200 m/s at t=0.125 μs, (c) 300 m/s at t=0.098 μs and (d) 400 m/s at t=0.095 μs. 96

4.13 Twin volume fraction contour of microscale structure subjected to impact loading (a) 100 m/s at t=0.25 μs, (b) 200 m/s at t=0.125 μs, (c) 300 m/s at t=0.098 μs and (d) 400 m/s at t=0.095 μs. 97

4.14 Rate-dependent twin formation in the HMX polycrystal. 97

5.1 Overview of the proposed uncertainty quantification framework. 108

5.2 The two-scale problem: macro- and microscales. 113

5.3 Microstructures features. 118

5.4 Cyclic loading. 123

5.5 SVE sizes. 126

5.6 Variability of D^3 CDF. 126

5.7 (a) Distributions of $D^{\star}$ with increasing number of SVEs, and (b) convergence of max $D^{\star}$ with increasing number of SVEs. 127

5.8 Motion of D^3 distribution. 128

5.9 Temporal evolution of the shape and scale parameter. 129

5.10 Experimental S-N data. 130

5.11 P_f calibration and prediction. 131

5.12 Distribution of D^3 and critical D^3. 132

Chapter 1

INTRODUCTION

1.1 Background and Motivation

This dissertation is concerned with understanding the uncertainty and variability of the failure and nonlinear response of materials with heterogeneous microstructures at fine (i.e., microns to millimeter) scales. Material response at the heterogeneous microstructure scale is often complicated due to the variation of structure and interacting chemo-thermo-mechanical processes acting at multiple time and length scales. The corresponding mechanistic models that describe the constituent behavior reflect the degree of complexity of these mechanisms [177]. The inherited variance in the material structure and properties further complicates the problem, as the variance of the key parameters results in material responses with uncertainty. In the microscale simulations with uncertainty in the complex morphologies and material behaviors, characterization of the relative roles of the competing and interacting deformation and failure mechanisms is a significant challenge, and there is a need to attack the problem from a probabilistic point of view. In this dissertation, I devise sensitivity analysis and uncertainty quantification frameworks to investigate two separate materials subjected to two different loading conditions. In the first case, the dynamic response of energetic materials in the form of particulate crystals embedded in a polymer matrix and in polycrystalline form are investigated. In the second case, this dissertation focuses on nucleation of cracks in a titanium alloy subjected to cyclic loading. The key unifying characteristics in these problems are the significant variability in the response due to inherent randomness in the material microstructure and the lack of knowledge in the critical microstructural mechanisms and parameters that lead to the onset of failure at this scale.

1.1.1 Case 1: Probabilistic Analysis of the Nonlinear Dynamic Response of Energetic Materials

1.1.1.1 Material Parameter Sensitivity Analysis for Energetic Materials

Material parameters that reflect the mechanical properties and possible deformation mechanisms are of interest for energetic materials, such as HMX (1,3,5,7-tetranitro-1,3,5,7-tetrazocane) based energetic composites. HMX is a polymorphic molecular crystal with numerous potential deformation mechanisms, where β phase is of significance since it is the stable phase at room temperature and pressure. Dynamic behavior of HMX particles is marked by the presence of orientation dependence [37, 112, 192] and complex plastic deformation mechanisms [26, 110, 154, 184]. A significant body of work exists on numerical modeling and experimental characterization of various mechanisms within energetic particles (e.g., pore collapse, inter-granular friction, particle fracture, dislocation pile-ups [19, 35, 40, 131, 176]) in order to understand and predict the overall performance of the energetic particles under dynamic loadings. Particularly in microscale simulations that involve complex anisotropic polycrystalline particles deforming at non-uniform high rate load regimes, characterization of the relative roles of the competing and interacting deformation and failure mechanisms within the energetic particles is important [12, 31, 198].

In view of the complexity of the deformation and failure mechanisms associated with the microstructure of HMX, there is a need to systematically understand how each mechanism incorporated into a numerical model affects and contributes to the overall behavior of the material. This can be achieved by employing a robust sensitivity analysis approach along with a reliable computational simulation framework that predicts the mechanical response of the material. Crystal Plasticity Finite Element (CPFE) simulation has been proven an effective tool and commonly used in predicting the orientation dependent behavior of HMX with multiple deformation mechanisms (monoclinic elasticity, thermal activation and phonon drag slip mechanisms, twinning and hydrodynamics). The available

crystal plasticity models [7, 10, 53, 60, 182, 195] focus on describing high rate deformation in HMX using dislocation slip. However, the identification of the most consequential elasticity coefficients, and slip and dislocation evolution mechanisms within the given dynamic loading regime for single crystal and polycrystalline HMX has not been studied. Material behaviors of energetic composites subjected to shock loads has drawn great attention since it provides insights into the fundamental nature of shock wave propagation and dissipation in energetic materials [7, 10, 60, 185, 196]. However, mechanical twinning, as observed in HMX [4, 21, 45, 124] for the twinning system $(101)[10\bar{1}]$ and HMX-based composites [138, 157], has not been systematically investigated at impact rate or gun shot rate regime, although it has been identified as the dominant deformation mechanism in compression tests [3, 90]. Therefore, developing a crystal plasticity model including important features of hydrodynamic behaviors under large transient loadings, such as large volume change and high strain rate, is of interest.

1.1.1.2 Machine-Learning Based Probabilistic Analysis Framework

To understand parametric sensitivities in the general context of particulate composites [140, 151, 188, 190], a number of analysis techniques including the One-At-a-Time (OAT) [144], differential analysis/local method [137], regression analysis [24] and others [41, 117, 145, 170] have been proposed. OAT probes the vicinity of a calibrated parameter set by varying one parameter at a time while other parameters are kept constant [12, 31]. The main drawback of the OAT method is that it cannot account for the interactions between parameters since only one parameter is probed each time [144]. Differential analysis relies on differentiation of the response function with respect to each input parameter [70, 140]. Besides, numerical approaches to differentiation are often computationally costly and limited to obtaining local sensitivities [67]. Regression analysis has also been employed as a sensitivity analysis method [24, 167] including for particulate composites [151]. Regression analysis relies on an assumed relationship between inputs and outputs, which makes

the obtained results dependent upon the assumed functional form [42]. Global sensitivity analysis (GSA) [146] enable us to compare the contribution of different properties/mechanisms over the entire parameter domain through the quantified sensitivities. It also offers the capability to quantify the sensitivity of all parameters along with the interactions between them [146].

The execution of GSA requires a substantial number of forward simulations, particularly for highly varying response functions. The nonlinear dynamic simulations of particulate composite microstructures [208] are typically extremely costly from the computational perspective. Hence there is always a clear need to perform sensitivity analysis in a computationally efficient manner. One example in this regard is relying on surrogate (e.g., Gaussian Process) modeling of the dynamic thermo-mechanical behavior of the material microstructure. Gaussian Process (GP) models employing commonly used squared exponential kernel or rational quadratic kernels are well-known to exhibit significant errors when the response function has discontinuities [162]. Therefore, the capability of representing discontinuous response functions is of interest.

The goal of the current study is to investigate the dynamic response of energetic materials through sensitivity analyses to understand and characterize the role of material morphologies and properties [19, 35, 40, 131, 176] in the microscale structure. To achieve the research goal, three objectives are set.

1. Establish a sensitivity analysis framework in the context of polymer bonded explosive (PBX) microstructures subjected to transient loading.

2. Investigate the role of deformation mechanisms in polycrystal β-HMX subjected to sub-shock impact loading.

3. Establish the mechanical twinning model for the molecular crystal β-HMX, and investigate its behavior during shock wave propagation.

1.1.2 Case 2: Probabilistic Analyses of the Fatigue Nucleation Behavior of a Titanium Alloy Subjected to Cyclic Loads

This study focuses on the effect of material properties of polycrystal titanium alloy on fatigue nucleation behavior. Depending on the manufacturing process techniques, the resulting microstructures of titanium alloys exhibit significantly different features, and the inherent randomness of material microstructure results in significant uncertainty in fatigue life [8, 85, 97, 175]. The effect of microstructure on fatigue nucleation life in titanium alloy, Ti-6Al-2Sn-4Zr-2Mo (Ti-6242) is the focus of this study.

Ti-6242 is a two-phase α/β titanium alloy that has been widely used in aerospace, orthopedic, and dental applications for its high specific strength and fracture toughness. In the past decades, the effect of Ti-6242 microstructure has been investigated with respect to influential microscale features (pure α grain size, colony grain, lamellae structure, micro-texture etc.) through experiments [27, 97, 106, 147] and numerical simulations [5, 33, 175, 204, 205]. To establish the connection between the microstructure and the variation in the local response of the material, the Statistical Volume Element (SVE) concept can be applied [22, 23]. Particularly, previous investigations linked material microstructure with the extreme value distribution of Fatigue Indicator Parameters (FIP) using CPFE simulations of a large number of SVEs [15, 54, 134].

The goal of the current study is to investigate the cyclic response of Ti-6242 through probabilistic analyses to understand and characterize the role of material microstructure [19, 35, 40, 131, 176] on the microscale behavior. Particularly, the objective is to study the effect of morphology variation of Ti-6242 lamellar microstructures on fatigue nucleation life.

1.2 Dissertation Organization

The remainder of this dissertation is organized to present the efforts conducted in achieving the objectives listed above as follows:

- Chapter 2 presents the proposed sensitivity analysis framework. The framework is verified in the context of the dynamic response of Hydroxyl-terminated polybutadiene (HTPB) polymeric binder reinforced with ammonium perchlorate (AP) particles. This chapter covers the work published in Ref. [202].

- Chapter 3 performs analyses for the quantification of material parameters through the proposed framework for the energetic crystal β-HMX with focus on the deformation mechanisms depicted in the constitutive model. This chapter covers the work published in Ref. [203].

- Chapter 4 introduces the large deformation CPFE formulation for β-HMX in which multiple deformation mechanisms (anisotropic elasticity, dislocation slip, twinning and large volumetric change) are incorporated. This CPFE model is employed to predict the dynamic behaviors of β-HMX in shock regime. This chapter covers the work published in Ref. [203].

- Chapter 5 expands the proposed framework to investigate the effect of the lamellar structure variation in Titanium alloy on fatigue nucleation life.

- Chapter 6 summarizes the research work conducted and the overall contribution of this dissertation.

Chapter 2

MATERIAL AND MORPHOLOGY PARAMETER SENSITIVITY ANALYSIS IN PARTICULATE COMPOSITE MATERIALS

2.1 Introduction

This chapter focuses on the establishment of the proposed sensitivity analysis framework, including the quantification of sensitivity with the existence of discontinuity on response surfaces. The sensitivity is quantified by Sobol's indices in the proposed framework to represent relative influence of model parameters. However, the evaluation of sensitivity indices require millions of detailed microstructural simulations which is computationally expensive. In view of the computational complexity, a piece-wise continuous GP surrogate model is incorporated into the framework. The Gaussian Process (GP) models are integrated with a support vector machine (SVM) classification algorithm that identifies the discontinuities within response surfaces such that the response surface is continuous within each subdomain. The proposed framework is employed to quantify sensitivities in the failure response of PBX under dynamic loads to material properties and morphological parameters with emphasis on the failure induced by interface separation. This chapter aims to demonstrate the sensitivity analysis framework by identifying the most consequential material and morphological parameters under vibrational and impact loads.

2.2 Microcale Modeling of the AP-HTPB system

We are interested in computing the sensitivity of the dynamic response of a microscale representative volume to material parameters of the composite constituents as well as the microscale morphology. Consider a representative volume that consists of randomly positioned particles with varying particle sizes and shapes as illustrated in Fig. 2.1. Under the applied loading, the composite is taken to undergo dissipative, large thermo-mechanical

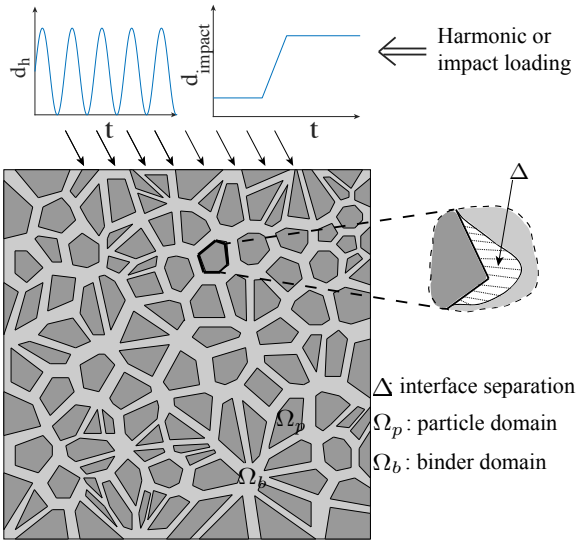

Figure 2.1: Problem setting: microscale geometry and loading.

deformations. In order to limit the complexity of the physics involved, the amplitude of the loads are taken small enough and possible chemical reactions are excluded. The interfaces between the particles and the binder are allowed to progressively degrade and debond. In view of the short loading times, the thermal process within the representative volume is assumed to be adiabatic. The particles are taken to exhibit elastic behavior under the applied loading. The constitutive models of the binder and the interfaces are described below.

2.2.1 Binder Constitutive Model

The binder is taken to be significantly softer than the particles, and assumed to exhibit viscoelastic response [68, 181]. The Cauchy stress within the binder is expressed in terms of the hereditary integral as a function of the shear relaxation modulus as

$$\boldsymbol{\sigma} = \int_0^t 2G(t,\tau)\boldsymbol{D}'(\tau)d\tau + K\frac{\ln J}{J}\boldsymbol{\delta} \tag{2.1}$$

where, $\boldsymbol{D}'(\tau)$ is the deviatoric component of the deformation-rate tensor, $\boldsymbol{D} = (\boldsymbol{L}^T + \boldsymbol{L})/2$, with $\boldsymbol{L}$ the velocity gradient tensor ($\boldsymbol{L} = \dot{\boldsymbol{F}}\boldsymbol{F}^{-1}$ with $\boldsymbol{F}$ the deformation gradient tensor), and $G(t,\tau)$ the shear relaxation modulus. The volumetric part of the deformation is taken

to behave elastically and K is the bulk modulus. J is the determinant of the deformation gradient, and $\boldsymbol{\delta}$ is the Kronecker delta.

The shear relaxation modulus, $G(t,\tau)$, is idealized using the Prony Series representation:

$$G(t,\tau) = \frac{T(\tau)}{T_{\text{ref}}} G_{h\infty} \left[1 + \sum_{i=1}^{n} p_i \exp\left(\frac{-(\xi(t) - \xi(\tau))}{q_i}\right) \right] \tag{2.2}$$

where, $G_{h\infty}$ is the steady-state shear modulus of the binder, T the temperature, T_{ref} the reference temperature, p_i and q_i are the fitting parameters of the n pairs of Prony Series prescribing the relative modulus, the relaxation time of the i_{th} Prony Series term, respectively, and:

$$\xi(t) = \int_0^t \frac{1}{a(T(\tau))} d\tau \tag{2.3}$$

where, $a(T)$ is the Williams-Landel-Ferry (WLF) empirical time-temperature shift function:

$$\log(a(T)) = \frac{A(T - T_{\text{ref}})}{B + T - T_{\text{ref}}} \tag{2.4}$$

A and B are material parameters. In view of the low conductivity and short loading time, the thermal process within the representative volume is assumed to be adiabatic. The viscoelastic dissipation induced heating under the adiabatic assumption is given by:

$$\dot{T} = \frac{1}{C_{V_b} \dot{W}_d} = \frac{2G_{h\infty}}{C_{V_b}} \frac{T(t)}{T_{\text{ref}}} \sum_{i=1}^{n} \frac{p_i}{q_i} \boldsymbol{\varepsilon}_d^i(t) : \boldsymbol{\varepsilon}_d^i(t) \tag{2.5}$$

where W_d is the dissipated work per unit reference volume, C_{V_b} the heat capacity per reference volume, and

$$\boldsymbol{\varepsilon}_d^i(t) = \int_0^t \exp\left(\frac{-(\xi(t) - \xi(\tau))}{q_i}\right) \boldsymbol{D}'(\tau) d\tau \tag{2.6}$$

2.2.2 Interface Constitutive Model

Prior experimental studies (e.g., [139, 206]) demonstrated that debonding at particle / binder interfaces is an important failure mechanism that may result in localized hot-spots in the context of energetic composites. Progressive damage accumulation and interface fracture is modeled by employing Cohesive Zone Modeling (CZM). CZM is well-known to accurately describe fracture processes particularly when the fracture path is pre-defined such as in the case of interface debonding problems [38].

In this chapter, a bilinear traction-separation law is employed in the context of CZM following Ref. [68]. Let $\lambda(\mathbf{x})$ denote a normalized equivalent displacement jump measure at an interface point, $\mathbf{x} \in S$ defined as [171]:

$$\lambda = \begin{cases} \sqrt{(\frac{\Delta_n}{\Delta_{cn}})^2 + (\frac{\Delta_t}{\Delta_{ct}})^2}, & \Delta_n \geq 0 \\ \frac{|\Delta_t|}{\Delta_{ct}}, & \Delta_n < 0 \end{cases} \tag{2.7}$$

where Δ_n and Δ_t are the normal and tangential components of the separation vector; and Δ_{cn} and Δ_{ct} are the critical normal and critical tangential separations under pure mode I and mode II conditions, respectively that result in traction free surface. Let λ_{ul} denote a history variable describing the peak normalized separation measure throughout the loading history:

$$\lambda_{ul} = \max_{\tau \in [0,t]} \lambda(\tau) \tag{2.8}$$

The damage state, d_m, at a material point is then expressed as a function of the history variable:

$$d_m = \begin{cases} 0, & 0 \leq \lambda_{ul} \leq \eta_0 \\ \frac{\lambda_{ul} - \eta_0}{(1-\eta_0)\lambda_{ul}}, & \eta_0 < \lambda_{ul} \leq 1 \\ 1, & \lambda > 1 \end{cases} \tag{2.9}$$

in which, η_0 is the elastic separation limit. The traction-separation relationship is expressed

as a function of damage, d_m, as:

$$t_{nc} = (1 - d_m)\frac{T_{\max}}{\eta_0}\frac{\Delta_n}{\Delta_{cn}} \tag{2.10}$$

$$t_{tc} = (1 - d_m)\frac{T_{\max}}{\eta_0}\frac{\Delta_t}{\Delta_{ct}} \tag{2.11}$$

where, t_{nc} and t_{tc} are normal and tangential traction components; $T_{\max}$ denotes the maximum interfacial traction.

The interpenetration between binder and particle is prevented by using the penalty contact algorithm. A linear relation between interpenetration ($|\Delta_n|$) and penalty traction p_n is:

$$p_n = \beta_p |\Delta_n| H(-\Delta_n) \tag{2.12}$$

where β_p is the penalty parameter; and H the Heaviside function. A regularized Coulomb law is employed to model the post-debonding frictional behavior along the particle-binder interface:

$$t_{tf} = \mu \frac{\dot{\Delta}_t}{\sqrt{\dot{\Delta}_t^2 + (\varepsilon)^2}} |p_n| \tag{2.13}$$

where ε is a regularization parameter, and as it approaches zero, Eq. 2.13 recovers the classical Coulomb law.The superposed dot indicates material time derivative. μ is the friction coefficient that increases with accumulating damage:

$$\mu = d_m \mu_0 \tag{2.14}$$

The overall local normal and tangential tractions considering the cohesive and the contact behavior are expressed as:

$$\boldsymbol{t}_n = [H(\Delta_n) t_{nc} + (H(\Delta_n) - 1) p_n] \hat{\boldsymbol{n}} \tag{2.15}$$

$$\boldsymbol{t}_t = [t_{tc} + (1 - H(\Delta_n))t_{tf}]\hat{\boldsymbol{t}} \tag{2.16}$$

where $\hat{\boldsymbol{n}}$ and $\hat{\boldsymbol{t}}$ are the normal and tangential unit vectors at the interface point. The decohesion process is assumed to generate negligible heat compared to the interface frictional heat. The total dissipated energy rate at the interface is assumed to be due to friction alone, which in turn leads to adiabatic temperature change as:

$$\dot{T}_{\text{int}} = \frac{t_{tf}\dot{\Delta}_t}{C_{V_{\text{int}}}} \tag{2.17}$$

where $C_{V_{\text{int}}}$ is the specific heat capacity at the interface.

2.2.3 Microscale Geometry

The morphology of the particulate composite microstructure significantly affects the failure and initiation behavior in energetic materials [71, 72, 116, 174]. Despite the recognition of morphology as a key factor influencing material dynamic behaviors, the relative importance/sensitivities of morphological parameters with respect to the behavior of interest remains to be systematically investigated and quantified. In the current study, the microscale morphology is probabilistically parameterized by the following: (1) particle size distribution, (2) particle area fraction distribution, and (3) particle sphericity (i.e., particle shape) distribution.

The particle area fraction and size distribution significantly affect the particle/binder interfacial behavior and the interaction between particles [11, 125]. For instance, the burning rate tailorability of propellants and explosive materials is partially controlled by particle size distributions [168]. In this study, the size of a particle is quantified directly as the area occupied by the particle.

Energetic particles vary significantly in shape and complexity which directly influence the particle-particle and particle-binder interactions. The impact of particle shape in localized increases in temperature has been reported in Refs. [34, 71, 116]. In the current

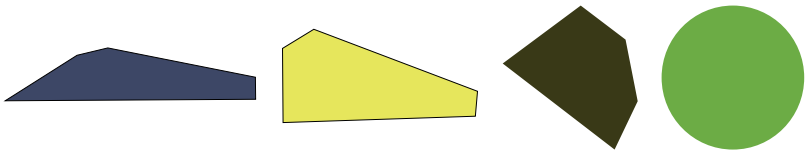

(a) $s = 0.62$ (b) $s = 0.75$ (c) $s = 0.85$ (d) $s = 1$

Figure 2.2: Shapes with different sphericity.

chapter, particle shapes are idealized as polygons, and the shape distribution is defined by the distribution of the parameter "sphericity". The sphericity is defined as the ratio of the perimeter of a sphere with equivalent particle size to perimeter of the polyhedron:

$$s = \frac{P_{eq}}{L_{edge}} \tag{2.18}$$

where $P_{eq} = 2\sqrt{\pi A}$, with A the particle size, L_{edge} the perimeter of the polyhedron. The sphericity value for each particle varies in the range $(0, 1)$. Sphericity near zero represents a thin and long shape, while near unit sphericity represents a shape that is very similar to a circle. Different shapes controlled by different sphericities are illustrated in Fig. 2.2. In the context of numerical verifications, the sphericity distribution within the particulate composite is taken to be Gaussian:

$$f(s) = N(\mu_s, \sigma_s) \tag{2.19}$$

where, μ_s and σ_s are the sphericity expectation and variance, respectively.

2.3 Sensitivity Analysis Framework

The proposed framework is established based the idea that parameter sensitivities of particulate materials should be quantified in a global sense (i.e., across the entire parameter space) to understand the role that each parameter plays on the corresponding failure mechanisms, and in the presence of discontinuous response surfaces under the applied loading.

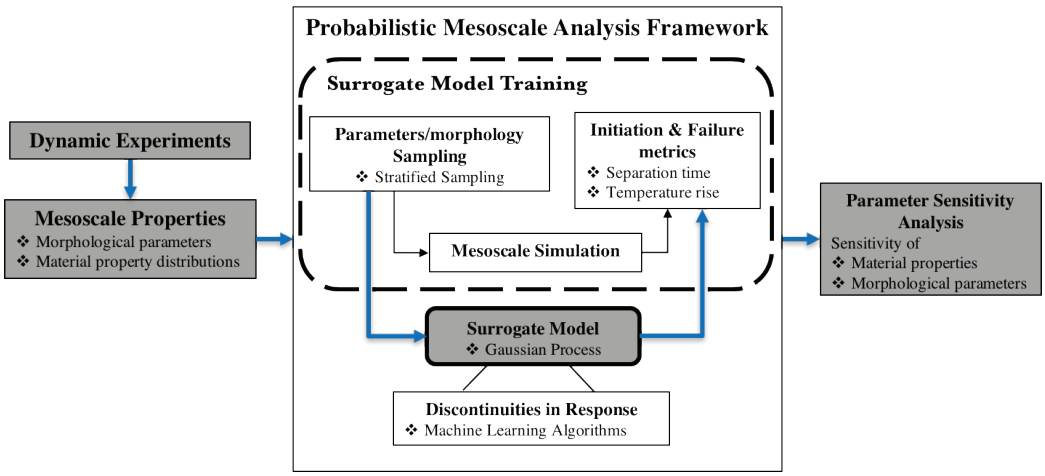

Figure 2.3: Overview of the proposed sensitivity analysis framework.

The proposed framework is schematically illustrated in Fig. 2.3.

The proposed framework relies on a parametric description of the microscale morphology as well as the constitutive response of the constituents (i.e., inclusion, binder, interface). The morphological and constitutive parameters are taken to be random variables. In order to perform sensitivity analysis, a set of samples is drawn to cover the entire subspace of physically plausible parameters. In order to avoid the necessity of performing direct microscale simulations for each sample point within the set, the proposed framework relies on adequately trained surrogate modeling (Gaussian Process, or GP) that relates the parameters to the response surface of a chosen microscale metric (e.g., interface separation, temperature rise, initiation). The sensitivity assessment is based on the Global Sensitivity Analysis (GSA) method. In GSA, the variance in the model output (i.e., microscale metric) results from the variance in the model input parameters (i.e., material parameters and the morphology), as well as the variance induced by the model input interactions. In this study, the contributions of the variance in each input to the variance in the output is characterized using the first order sensitivity and total effect indices. First order index represents the contribution to the output variance from the parameter itself, while total effect index also includes the interactions between the parameter and the other parameters.

2.3.1 Stratified Sampling

The sampling of the parameter space is performed such that the following two requirements are satisfied: (1) The samples must cover the entire parameter space. This is in view of the fact that we seek to compute the sensitivity of the parameters across the entire parameter space, in contrast to local sensitivities. (2) The total number of samples must be as small as possible for computational efficiency, in view of the computational complexity of the microscale simulations. In the current study, the Stratified Sampling method [120] is employed. Stratified sampling ensures certain subspaces are not overrepresented or underrepresented. The idea of stratified sampling is to partition the parameter space to multiple non-overlapping subspaces, and to ensure that a set of samples from each subspace is drawn. Sampling within each subspace allows probing the local characteristics of the response function throughout the parameter space.

The benefit of employing the stratified sampling method is graphically illustrated in Fig. 2.4. In Fig. 2.4a, stratified sampling is applied to generate 100 randomly distributed samples in a two dimensional parameter space. The entire region is evenly divided as $10 \times 10 = 100$ subspaces with one sample per subspace. In Fig. 2.4b, uniform sampling was employed to draw 100 samples. The uniform sampling method fails to generate samples in 38 of the subspaces probed by stratified sampling, and fails to sample from large swaths of the parameter space. Alternative sampling approaches such as Sobol sequences [158] and other quasi Monte Carlo methods that uniformly sample the entire parameter space could also be employed with similar efficiency compared with the stratified sampling.

2.3.2 Gaussian Process Model

In view of the significant computational cost of performing microscale dynamic simulations, probing the entire parameter space within the context of sensitivity analysis through microscale simulations as a forward solver is computationally prohibitive. In this study, we employ Gaussian Process modeling as the surrogate forward simulator. In this approach,

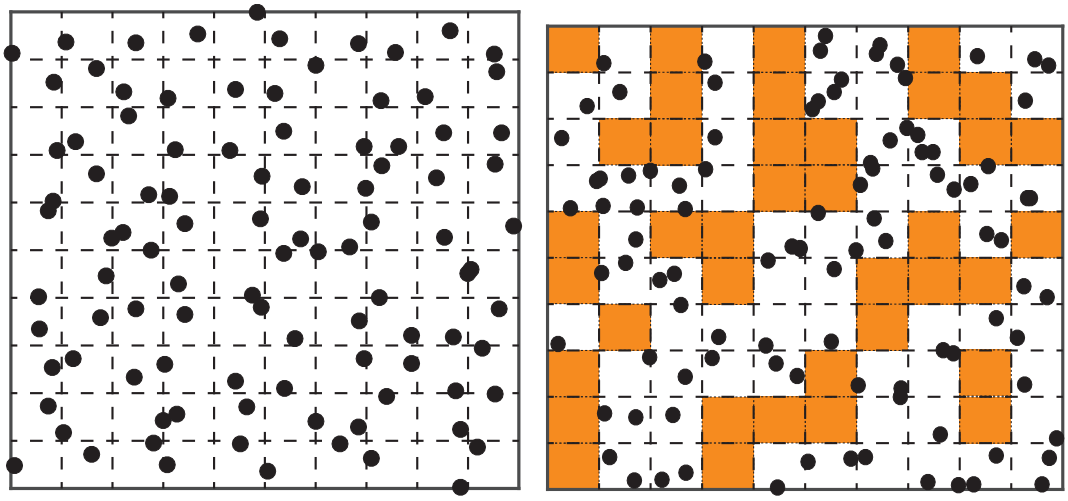

(a) Stratified sampling. (b) Uniform sampling

Figure 2.4: Comparison between stratified sampling and uniform sampling.

a small suite of microscale simulations are performed with randomly sampled parameters to generate discrete values of the response function, called training points. The training points are employed to construct the surrogate model, which is in turn employed to predict the response with randomly sampled prediction points.

Gaussian process (or Kriging) is a method of interpolation for which the interpolated values are modeled by a Gaussian process governed by prior covariance. The Gaussian process method is probabilistic, and it generates a distribution instead of a single prediction value at the prediction point. The variance of the prediction distribution is related to the proximity of the prediction point input (i.e., the parameter set that correspond to the prediction point) and the training point inputs as illustrated in Figure 2.5a.

The GP model is expressed in the following form:

$$G_p(\boldsymbol{u}) = \boldsymbol{h}(\boldsymbol{u})^T \cdot \boldsymbol{\beta} + Z(\boldsymbol{u}) \tag{2.20}$$

where $\boldsymbol{u} = (u^1, u^2, ..., u^d)$ denotes the vector of input parameters, each of which is a random variable, d denotes the number of parameters (i.e., the dimensionality of the problem), $\boldsymbol{h}$ is the trend of the model, $\boldsymbol{\beta}$ is the vector of trend coefficients, and Z is a stationary

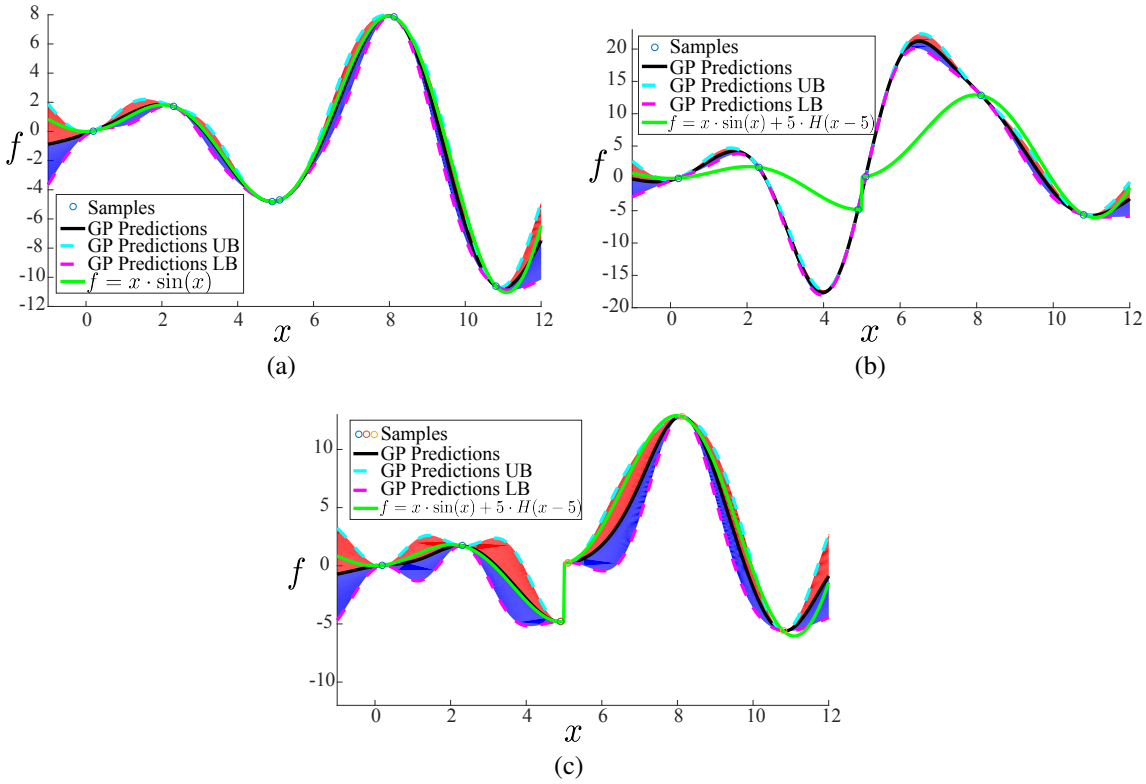

Figure 2.5: Example of GP model and discontinuity. Illustration of (a) a GP surrogate of function, $f = x \cdot \sin(x)$ trained with 6 training points; (b) a GP surrogate of function, $f = x \cdot \sin(x) + 5 \cdot H(x-5)$ trained with 6 samples; (c) two local GP surrogates of function, $f = x \cdot \sin(x) + 5 \cdot H(x-5)$ trained with 6 samples.

Gaussian process with zero mean. The trend of the model is taken to be up to second order polynomial regression model in this study, and higher order polynomial trend could be achieved via increasing the number of training samples.

The covariance between sample outputs is defined as

$$Cov[Z(\boldsymbol{a}), Z(\boldsymbol{b})] = \sigma_z^2 \cdot R(\boldsymbol{a}, \boldsymbol{b}) \tag{2.21}$$

where σ_z^2 is the process variance and $R(\cdot,\cdot)$ is the correlation function between two input points $\boldsymbol{a}$ and $\boldsymbol{b}$. Squared-exponential function, a commonly used correlation function is

employed:

$$R(\boldsymbol{a},\boldsymbol{b}) = \exp[-\sum_{i=1}^{d} \theta_i (a_i - b_i)^2] \tag{2.22}$$

where $\theta_i \in \boldsymbol{\theta} = (\theta_1, ..., \theta_d)$ is a parameter that indicates the correlation between the points within dimension i, a_i and b_i are the i_{th} components of $\boldsymbol{a}$ and $\boldsymbol{b}$, respectively.

The expectation value and variance of the GP model prediction distribution at input point $\boldsymbol{u}$ are expressed as:

$$\mu_G(\boldsymbol{u}) = \boldsymbol{h}(\boldsymbol{u}) \cdot \boldsymbol{\beta} + \boldsymbol{r}(\boldsymbol{u})^T \boldsymbol{R}^{-1} (\boldsymbol{g} - \boldsymbol{F}\boldsymbol{\beta}) \tag{2.23}$$

$$\sigma_G^2(\boldsymbol{u}) = \sigma_z^2(\boldsymbol{u}) - \begin{bmatrix} \boldsymbol{h}(\boldsymbol{u})^T & \boldsymbol{r}(\boldsymbol{u})^T \end{bmatrix} \begin{bmatrix} \boldsymbol{0} & \boldsymbol{F}^T \\ \boldsymbol{F} & \boldsymbol{R} \end{bmatrix}^{-1} \begin{bmatrix} \boldsymbol{h}(\boldsymbol{u}) \\ \boldsymbol{r}(\boldsymbol{u}) \end{bmatrix} \tag{2.24}$$

where $\boldsymbol{r}(\boldsymbol{u})$ is a vector containing the covariance between $\boldsymbol{u}$ and each of the n training points ($\boldsymbol{u}_1$, ..., $\boldsymbol{u}_n$), $\boldsymbol{R}$ is $n \times n$ matrix containing the correlation between each pair of training points, $\boldsymbol{g}$ is the vector of response outputs at each of the training points, and $\boldsymbol{F}$ is $n \times q$ matrix with rows $\boldsymbol{h}(\boldsymbol{u}_i)^T$, where q is the number of trend function terms for each row.

The process variance σ_z^2 and character parameter $\boldsymbol{\theta}$ are determined through maximum likelihood estimation. Taking the log of the probability of observing the response values $\boldsymbol{g}$ given the covariance matrix $\boldsymbol{R}$:

$$\log[p(\boldsymbol{g}|\boldsymbol{R})] = -\frac{1}{n}\log|\boldsymbol{R}| - \log(\hat{\sigma}_z^2) \tag{2.25}$$

where $|\boldsymbol{R}|$ indicates the determinant of $\boldsymbol{R}$, and $\hat{\sigma}_z^2$ is the optimal value of the variance given an estimate of $\boldsymbol{\theta}$ and is defined by

$$\hat{\sigma}_z^2 = -\frac{1}{n}(\boldsymbol{g} - \boldsymbol{F}\boldsymbol{\beta})^T \boldsymbol{R}^{-1} (\boldsymbol{g} - \boldsymbol{F}\boldsymbol{\beta}) \tag{2.26}$$

Maximizing Eq. 2.25 gives the maximum likelihood estimate of $\boldsymbol{\theta}$, which in turn defines

σ_z^2.

2.3.3 Discontinuities and Classifier

The response of particulate composites under dynamic loading conditions are marked by the presence of discontinuities induced by the discrete failure events that are functions of both material and morphological parameters. In contrast, the Gaussian Process models employing squared-exponential covariance functions or rational quadratic kernels exhibit significant errors when the response function is discontinuous [162]. Figure 2.5b illustrates the GP approximation of a function similar to that shown in Fig. 2.5a, but that contains a discontinuity. With the same training samples used in Fig. 2.5a, the GP model shown in Fig. 2.5b fails to accurately represent the discontinuous function.

In this chapter, a piece-wise continuous GP model is proposed to account for the presence of discontinuities in the response functions. The piece-wise continuous GP model is built by employing the support vector machine (SVM) - a classification algorithm to solve the model selection problem.

Let $\Theta \subset \mathbb{R}^d$ denote the parameter space, which yields a discontinuous response function, $y(\boldsymbol{u})(\boldsymbol{u} \in \Theta)$. The response function is assumed to be continuous within q subdomains $(\Theta_a \subset \Theta; a = 1, ..., q)$ separated by $(m-1)$ dimensional hyperplanes. The corresponding piecewise continuous GP approximation of the response function is expressed as:

$$GP(\boldsymbol{u}) = \sum_{a=1}^{q} N_a(\boldsymbol{u}) GP_a(\boldsymbol{u}) \tag{2.27}$$

in which GP_a denotes the continuous GP approximation valid within Θ_a; and N_a is a piecewise constant shape function:

$$N_a(\boldsymbol{u}) = \begin{cases} 1, & \text{if} \quad \boldsymbol{u} \in \Theta_a \\ 0, & \text{elsewhere} \end{cases} \tag{2.28}$$

Figure 2.5c illustrates a piece-wise continuous GP model in predicting the discontinuous function shown in Fig. 2.5b. The continuous parts on both sides of the discontinuity of the function are captured within the $\mu_G \pm 3\sigma_G$ interval by the two local surrogates.

The primary difficulty in the construction of the proposed surrogate model in Eq. 2.27 is that the parameter subdomains Θ_a are not known a-priori. We seek to identify the separator hyperplanes between the parameter subdomains based on a classification algorithm of the machine learning theory [86]. SVM is a discriminative classifier formally defined by a separating hyperplane/decision boundary [166]. For given set of input points $(\boldsymbol{u}_1, ..., \boldsymbol{u}_n)$ with their corresponding outputs $(\boldsymbol{y}_1, ..., \boldsymbol{y}_n)$, $\boldsymbol{\phi}$ is a mapping function from the input space to a hypothesis and potentially infinite-dimensional feature space [149] in which the inner product is $\langle \boldsymbol{\phi}(\boldsymbol{u}_i), \boldsymbol{\phi}(\boldsymbol{u}_j) \rangle$ such that the training set is linearly separable. The hyperplane is found through the following optimization problem:

$$\max_{\boldsymbol{w},b} \quad \min_{i} \left\{ \boldsymbol{y}_i \left[\langle \boldsymbol{w}, \boldsymbol{\phi}(\boldsymbol{u}_i) \rangle - b \right] \right\}$$

where $\langle \cdot, \cdot \rangle$ represents inner product, $\boldsymbol{w}$ is a vector, and b is a real number. The expression $(\langle \boldsymbol{w}, \boldsymbol{\phi}(\boldsymbol{u}_i) \rangle - b)$ is the distance between $\boldsymbol{u}_i$ and the decision boundary. The sign of $\boldsymbol{y}_i \{ \langle \boldsymbol{w}, \boldsymbol{\phi}(\boldsymbol{u}_i) \rangle - b \}$ is positive for the correct classifications and negative for the incorrect classifications. If all data sets are linearly separable, $\gamma = \min \left\{ \boldsymbol{y}_i \left[\langle \boldsymbol{w}, \boldsymbol{\phi}(\boldsymbol{u}_i) \rangle - b \right] \right\}$ is positive. It is proven in [29] that the decision function

$$f(\boldsymbol{u}) = \text{sign}(\langle \boldsymbol{w}, \boldsymbol{\phi}(\boldsymbol{u}) \rangle - b) \tag{2.29}$$

is equivalent to

$$f(\boldsymbol{u}) = \text{sign}(\sum_{i=1}^{n} \alpha_i \boldsymbol{y}_i \langle \boldsymbol{\phi}(\boldsymbol{u}_i), \boldsymbol{\phi}(\boldsymbol{u}) \rangle - b). \tag{2.30}$$

From this expression, it can be observed that only those points with non-zero α_i (called support vector) determine the hyperplane. The dot product between data point vectors,

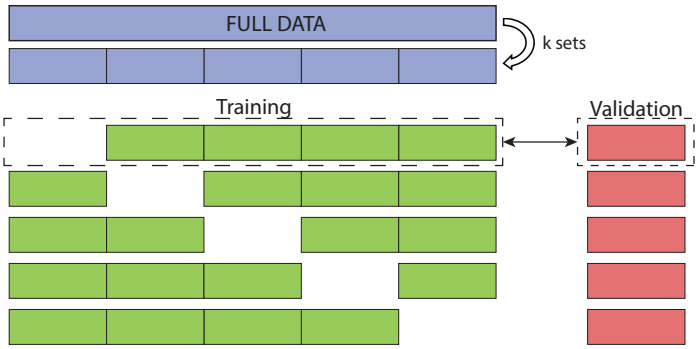

Figure 2.6: Cross-validation of the classification algorithm.

$\boldsymbol{\phi}(\boldsymbol{u}_i)$ and $\boldsymbol{\phi}(\boldsymbol{u}_j)$, is written as $K_{ij} = \langle \boldsymbol{\phi}(\boldsymbol{u}_i), \boldsymbol{\phi}(\boldsymbol{u}_j) \rangle$. Eq. 2.30 becomes:

$$f(\boldsymbol{u}) = \text{sign}(\sum_{i=1}^{n} \alpha_i \boldsymbol{y}_i \boldsymbol{K}(\boldsymbol{u}_i, \boldsymbol{u}_j) - b). \tag{2.31}$$

where $\boldsymbol{K}$ is the kernel matrix. In current study, quadratic kernel $K(\boldsymbol{u}_i, \boldsymbol{u}_j) = (\langle \boldsymbol{u}_i, \boldsymbol{u}_j \rangle + 1)^2$ is employed.

An additional and equally important problem is the identification of the number of discontinuities, q, within the parameter space. While not straightforward, those problems that exhibit unknown number of discontinuities could be addressed through cluster analysis in data mining, such as the elbow method [57], X-means clustering [126], Akaike information criterion [143], the silhouette method [142]. In the examples in this chapter, the number of discontinuities are dictated by the physics of the problem and assumed to be known a-prior.

The performance of the classifier is assessed by *k*-folder cross-validation, which is a non-exhaustive cross-validation method [84] as illustrated in Fig. 2.6. The full set of input parameters is separated into k sets of equal size. An arbitrary subset is taken as the *validation set*, whereas the remaining $(k-1)$ sets are employed as *training sets*. The training sets are employed to construct the classifier. The validation set is then employed to assess whether the predicted classification (i.e., the associated parameter subdomain of each input, $\boldsymbol{u}_i$) is accurate. This process is repeated k times by assigning a different subset as the validation set.

Table 2.1: Confusion matrix.

	Positive (Predict)	Negative (Predict)
Positive (Actual)	***True***	***False***
Negative (Actual)	***False***	***True***

Confusion matrix (i.e., error matrix) is produced by cross-validation to quantify the performance of a classifier (Table 2.1). Confusion matrix is a specific table layout that allows visualization of the performance of an algorithm. Each row of the confusion matrix represents the true class (i.e., the parameter subdomain), while each column of the confusion matrix represents the prediction of the classifier. For example, the $(i, j)_{\text{th}}$ element in the confusion matrix indicates the number or percentage of cases which belong to i_{th} parameter subdomain while predicted as j_{th} parameter subdomain. The diagonal terms represent the number or percentage of correct predictions of the classifier. For k-folder cross-validation, k confusion matrices are generated and summed to construct the overall confusion matrix.

2.3.4 Global Sensitivity Analysis

Among various sensitivity analysis methods, Global Sensitivity Analysis (GSA) has the ability to collect information from the entire input domain instead of local points, which makes the quantitive measurement of the sensitivity over the entire domain possible. The primary idea of GSA is to divide the uncertainty or variance of model output into different sources of uncertainty or variance of model inputs, and the contributions from different sources are quantified by sensitivity indices.

The most sensitive parameter is identified through the GSA framework in both sense of self-contribution and parameter interactions, and insensitive parameters are set as constant in the view of computational complexity. In the view of multiple potential failure mechanisms, GSA provide the ability to understand the dominant mechanisms behind the complex input-output relationships over the input space, and eliminate the trivial influence

from insensitive parameters. The parameter sensitivities obtained from GSA are parameter space dependent, considering that failure mechanisms are dominant at different parameter subspaces, and GSA focuses on the output uncertainty over the desired parameter space.

2.3.4.1 Decomposition of Variance

Arbitrary target function $y = f(\boldsymbol{u}) = f(u^1, ..., u^d)$ is decomposed as [159]

$$f(u^1, ..., u^d) = f_0 + [\sum_{i=1}^{d} \phi_i(u^i) + \sum_{i_1=1}^{d-1} \sum_{i_2=i_1+1}^{d} \phi_{i_1,i_2}(u^{i_1}, u^{i_2}) + ... + \phi_{1,2,...,d}(u^1, ..., u^d)] \quad (2.32)$$

where

$$\begin{cases} f_0 = \int f(\boldsymbol{u}) \prod_{i=1}^{d} [p_i(u^i) du^i] = E(y) & (2.33) \\ \phi_i(u^i) = \int f(\boldsymbol{u}) \prod_{j \neq i} [p_j(u^j) du^j] - f_0 = E_{u^{-i}}(y|u^i) - f_0 & (2.34) \\ \phi_{i_1,i_2}(u^{i_1}, u^{i_2}) = \int f(\boldsymbol{u}) \prod_{j \neq i_1, i_2} [p_j(u^j) du^j] - \phi_{i_1}(u^{i_1}) - \phi_{i_2}(u^{i_2}) - f_0 & (2.35) \end{cases}$$

with $p_i(u^i)$ the probably distribution function (PDF) of u^i, thus $\int f(\boldsymbol{u}) \prod_{j \neq i} [p_j(u^j) du^j]$ is $E_{u^i}(y|u^i)$ by definition. The constant f_0 is the expectation value of y. $\phi_i(u^i)$ represents the contribution of u_i to f only from itself, while $\phi_{i_1,i_2}(u^{i_1}, u^{i_2})$ represents the contribution from the interaction between u^{i_1} and u^{i_2} to f. The variance of y is obtained:

$$\text{Var}(y) = \int [f(u^1, ..., u^d) - f_0]^2 \prod_{i=1}^{d} [p_i(u^i) du^i] \quad (2.36)$$

The parameters are taken to be independent (i.e., uncorrelated) random variables, which ensures the uniqueness of the the decompositions stated above [159].

2.3.4.2 Sensitivity Index

Sensitivity index is a measurement of the parameter sensitivity/importance to the model output variance. Sensitivity indices quantify the contribution of the parameter itself and the

interaction between the parameter and other parameters across the entire input domain. The first order index quantifies the contribution to output variance from the parameter itself, i.e., the first order terms in Eq. 2.32, while total effect index also includes the higher order terms in Eq. 2.32, i.e., the interactions between the parameter and the other parameters. Substituting Eq. 2.36 into Eq. 2.32:

$$1 = \sum_{i=1}^{d} S_i + \sum_{i_1=1}^{d-1} \sum_{i_2=i_1+1}^{d} S_{i_1 i_2} + \ldots + S_{1,2,\ldots,d} \tag{2.37}$$

where the first order sensitivity index S_i is defined [159]:

$$S_i = \frac{\mathrm{Var}(\phi_i(u^i))}{\mathrm{Var}(y)} = \frac{\mathrm{Var}_{u^i}(E_{u^{-i}}(y|u^i))}{\mathrm{Var}(y)} \tag{2.38}$$

The notation u^{-i} represents all possible u^j for $j \neq i$. $\mathrm{Var}_{u^i}(E_{u^{-i}}(y|u^i))$ is the variance of the expectation of y given u^i . $E_{u^{-i}}(y|u^i)$ is computed by varying u^{-i} for a fixed u^i, whereas $\mathrm{Var}_{u^i}(E_{u^{-i}}(y|u^i))$ is calculated by varying u^i.

The total effect index, S_i^T, is expressed as:

$$S_i^T = 1 - \frac{\mathrm{Var}_{u^{-i}}(E_{u^i}(y|u^{-i}))}{\mathrm{Var}(y)} \tag{2.39}$$

where $E_{u^i}(y|u^{-i})$ is the expectation of y given u^{-i}. The total effect index S_i^T is the sum of first order index and corresponding higher order terms [64]:

$$S_i^T = S_i + \sum_{j}^{d} S_{ij} + \sum_{j_1=1}^{d-1} \sum_{j_2=j_1+1}^{d} S_{ij_1j_2} + \ldots + S_{1,2,\ldots,d} \tag{2.40}$$

where S_{ij} represents the interaction between u^i and u^j, $S_{ij_1j_2}$ represents the interactions between u^i, u^{j_1} and u^{j_2}, $S_{1,2,\ldots,d}$ is the interactions between all input parameters. The interaction terms in the total effect index is non-zero despite the fact that the parameter distributions are taken to be uncorrelated [92]. The numerical computation of sensitivity

indices is performed using the Monte-Carlo based procedure proposed by Saltelli et al. [146]. The sum of total effect indices have the following property:

$$\sum_{i=1}^{d} S_i^T \geq 1 \tag{2.41}$$

This is due to the fact that the interaction between u^i and u^j is accounted for in both S_i^T and S_j^T.

2.4 Numerical Examples

The sensitivity analysis framework has been exercised to study two cases: (1) The dynamic response of a single AP particle embedded in HTPB binder. Particularly, the investigation focuses on the sensitivity of interfacial separation observed under impact loading to the parameters that describe the constitutive behavior of the binder and the interface. (2) The dynamic response of a multi-particle microstructure subjected to ultrasonic vibration loading to study the size and morphology sensitivity of the temperature rise within the microstructure.

2.4.1 Material Property Sensitivity

The dynamic response of energetic materials is sensitive to the particle/binder interface, since the interfacial separation, upon debonding, leads to temperature rise induced by frictional heating and dissipation within the binder. In the current numerical study, material properties, especially interfacial parameters, are investigated using the proposed framework.

2.4.1.1 microscale Model

In this study, a fixed microstructure that consists of a single AP particle embedded in the HTPB binder is considered. The microscale geometry and corresponding boundary conditions are illustrated in Fig. 2.7a. The 3 mm $\times$ 2 mm rectangular composite specimen

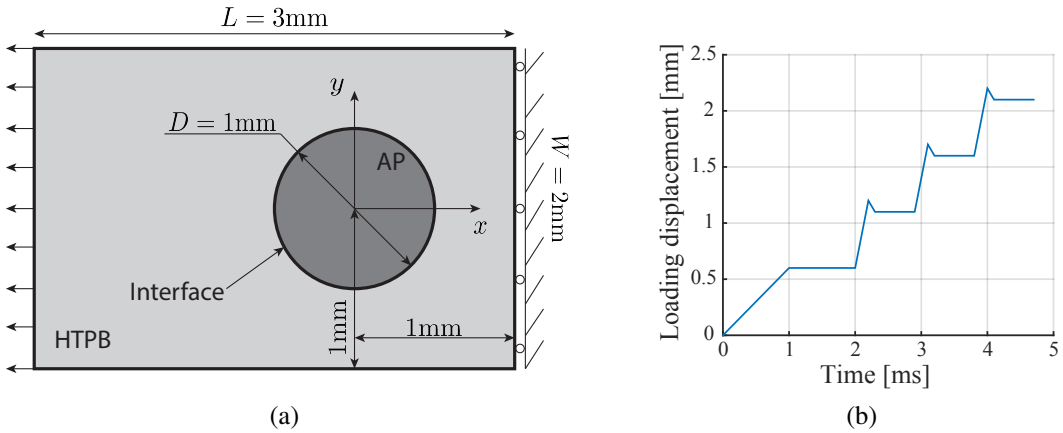

(a) (b)

Figure 2.7: Dynamic response of a single AP particle reinforced HTPB. (a) The geometry and boundary conditions; (b) the loading history.

includes a circular AP particle with a diameter of 1 mm. One edge of the specimen is fixed, while high rate impact loading is applied along the other edge. The displacement-controlled loading profile is shown in Fig. 2.7b, which consists of four step loadings. The loading rate in the first step is 600 mm/s, whereas the remaining three are applied at 3000 mm/s rate. The loading profile is similar to a tensile Kolsky bar test that includes a quasi-static preload, followed by the applied load amplitude and multiple reflections. Under the applied loading, the AP particle is assumed to behave elastically. The HTPB binder undergoes viscoelastic deformation, and the interface progressively debonds based on the cohesive zone model described above. The response function of interest is the time to onset of interface separation defined as the time when the maximum separation reaches half of the particle diameter.

The AP particle Young's modulus and Poisson's ratio are obtained from [96]. The density ρ_{AP} is 1.95×10^{-3}, and the specific heat capacity per unit volume $C_{V_{AP}}$ is $2.121 \text{mJ}/\text{mm}^3\text{K}$ [59].

Fifteen material parameters fully describe the thermo-mechanical deformation in the binder. The viscoelastic response is approximated using a four-component Prony Series model. The parameter set is split into two subsets. The first set consists of those parameters a-priori considered to be insensitive with respect to the response function, or are fixed. The

Table 2.2: Binder and particle fixed parameters.

Parameter	ρ_h	ν_h	C_{V_h}	T_{ref}	A	B	E_{AP}	ρ_{AP}
Unit	g/mm^3		$\text{mJ}/\text{mm}^3\text{K}$	K			MPa	g/mm^3
Value	$0.95 \cdot 10^{-3}$	0.45	1.987	253	-15	102	$1.95 \cdot 10^4$	$1.95 \cdot 10^{-3}$
Parameter	$C_{V_{AP}}$	ν_{AP}	p_3	p_4	q_1	q_2	q_3	q_4
Unit	$\text{mJ}/\text{mm}^3\text{K}$		MPa	MPa	ms	ms	ms	ms
Value	2.121	0.3	25	13	$2 \cdot 10^{-5}$	$2 \cdot 10^{-4}$	$2 \cdot 10^{-3}$	$2 \cdot 10^{-2}$

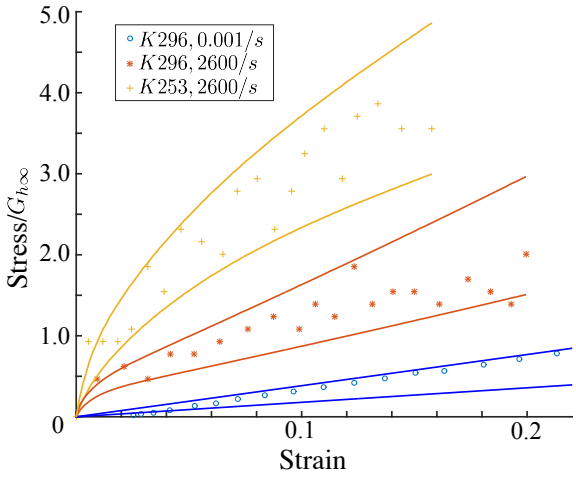

Figure 2.8: Prony series ranges calibration with experimental data.

density of the HTPB binder, ρ_h, is $0.95 \times 10^{-3}\text{g}/\text{mm}^3$. The Poisson's ratio of HTPB is taken to be 0.45, the same as that of Sylgard 184 [148, 164]. The specific heat capacity per unit volume, C_{V_h} is $1.987\text{mJ}/\text{mm}^3\text{K}$ [59]. The reference temperature T_{ref} and temperature shift factors A, B are kept consistent with Ref. [68]. The values of the fixed parameters are summarized in Table 2.2. The remainder of the parameters (i.e., the second set) are taken to be sensitive to the response function and employed as variables in the sensitivity study. The specific distributions of the parameters are unknown (due to lack of sufficient experiments to characterize the distributions). The parameters are therefore assumed to follow uniform distributions, which only require lower and upper bounds. The parameter ranges within the second set are identified based on experimental data and calibrated from stress-strain curves at different temperature and loading rates. Figure 2.8 shows the identification of the upper and lower bounds for the viscoelastic parameters (p_1, p_2, G_{h_∞}) by fitting bounds to the

Table 2.3: Parameter boundaries in material property sensitivity study.

Parameter	p_1	p_2	$G_{h\infty}$	$T_{\max}$	Δ_{cn}	Δ_{ct}	μ_0	w_{int}	ρ_{int}
Unit	MPa	MPa	MPa	MPa	mm	mm		mm	g/m^3
Upper bd	80	48	$1.95 \cdot 10^{-3}$	2.9	5	0.25	0.3	0.3	$3 \cdot 10^{-3}$
Lower bd	65	27	$0.95 \cdot 10^{-3}$	1.35	0.5	0.1	0.2	0.2	$2 \cdot 10^{-4}$

Table 2.4: Interfacial fixed parameters

Parameter	η_0	ε	β_s	$C_{V_{\text{int}}}$
Unit			MPa/mm	$\text{mJ}/\text{mm}^3\text{K}$
Value	0.014	10^{-5}	1900	2.054

HTPB experimental stress-strain curves based on the data from Ref. [20]. The parameter ranges for the viscoelastic parameters employed in the sensitivity analysis are shown in Table 2.3.

Ten parameters describe the thermo-mechanical behavior and the progressive debonding along the particle-binder interface. Similar to the binder case, the parameter set is split into two subsets. The first set consists of those parameters a-priori considered to be insensitive with respect to the response function, or are fixed. The elastic limit η_0 is reported in [68]. The regularization parameter ε, which is introduced from the numerical efficiency point of view, is determined as 1×10^{-5} by a numerical parametric study in which the error caused by the regularization is not greater than 0.2% compared to the classical Coulomb law. The interfacial stiffness β_s is experimentally obtained by measuring the slope of the stress-strain curve [68]. The interfacial heat capacity $C_{V_{\text{int}}}$ is taken as the average of the two material phases (AP and HTPB), i.e., $C_{V_{\text{int}}} = 2.054\text{mJ}/\text{mm}^3\text{K}$. The values of the fixed parameters are summarized in Table 2.4. The remainder of the parameters are taken to be sensitive to the response function and employed as variables in the sensitivity study. The maximum traction $T_{\max}$, the critical normal separation Δ_{cn}, the critical tangential separation Δ_{ct}, the interfacial width w_{int}, the interfacial density ρ_{int}, and the friction coefficient μ_0 are included as variables in the sensitivity study. Parameter ranges of the cohesive zone model are selected based on the properties of the PBXs investigated in

Table 2.5: Overall accuracies of classifiers

Classifier	Linear SVM	Simple Tree	Coarse KNN[1]	LD[2]
Accuracy	94.4%	81.4%	95.3%	90.4%
Prediction Speed [obj/s[4]]	$\sim$ 28000	$\sim$ 96000	$\sim$ 33000	$\sim$ 72000
Classifier	Quadratic SVM	Medium Tree	Medium KNN	QD[3]
Accuracy	98.2%	96.6%	96.6%	91.0%
Prediction Speed [obj/s]	$\sim$ 25000	$\sim$ 120000	$\sim$ 57000	$\sim$ 52000

[1] k-Nearest Neighbor
[2] LD represents linear discriminant
[3] QD represents quadratic discriminant
[4] obj/s represents objective (or number of function evaluations) per second

Refs. [11, 58, 68, 130, 160, 187] and listed in Table 2.3.

In summary, three binder parameters (i.e., p_1, p_2 and G_{h_∞}) and six interfacial parameters (i.e., $T_{\max}$, Δ_{cn}, Δ_{ct}, w_{int}, ρ_{int}, and μ_0) for a total of nine parameters are included in the current sensitivity study.

2.4.1.2 Local GP Models and Classifier

Under the applied step-wise loading, interface separation (as a function of material parameters) tends to cluster near the load steps. This results in a multi-modal distribution of time-to-separation as further discussed below. In order to accurately approximate this behavior using surrogate modeling, we employed the piecewise continuous GP model (Eq. 2.27). The classifier SVM provides higher accuracy than some of the other classifiers (e.g. decision tree, k-Nearest Neighbor Classifier, discriminant analysis) at the cost of added computational complexity, as shown in Table 2.5.

A five-part GP model has been constructed to predict the sensitivity of the nine material parameters on the failure behavior of the composite. The five-part model corresponds to the parameter subspaces that result in failure near the four step loads, in addition to the subspace that result in no interface separation.

In Fig. 2.9, Von Mises stress contours are plotted from four representative simulations at the state of interface failure (i.e., separation time). The contour plots indicates a change

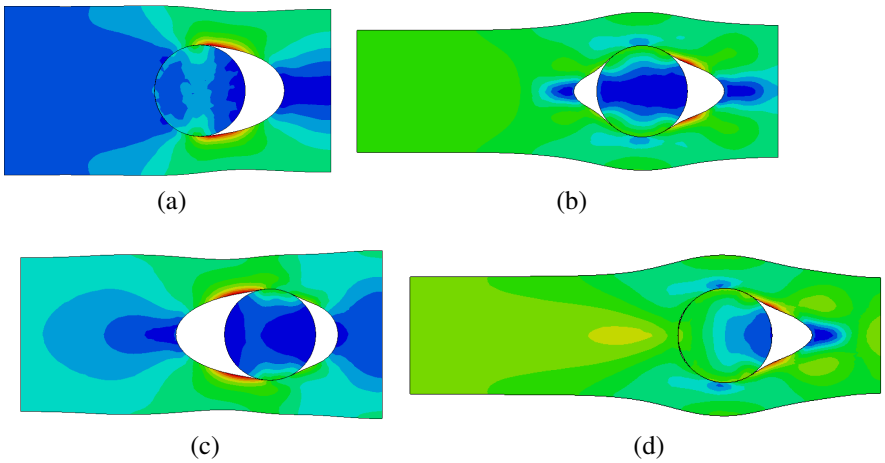

Figure 2.9: Von Mises stress contours of single particle system failure at (a) $t = 1.04$ ms; (b) $t = 2.12$ ms; (c) $t = 3.08$ ms; (d) $t = 3.932$ ms.

in interface separation characteristics in addition to separation time as a function of constituent parameters. The proposed five-part GP model is trained by a suite of training points that are obtained through the dynamic analysis of the microstructure using the finite element method with randomly sampled parameters using the stratified sampling method. The accuracy of the GP model has been assessed by verifying the convergence as a function of the number of training points, and the number of prediction points, as well as by verifying the accuracy of subspace classification through the confusion matrix.

Figure 2.10a illustrates the convergence of the GP model as a function of the number of training points employed. The figure shows the prediction of time-to-separation PDFs based on three piecewise continuous GP models trained by 256, 512, 5120 microscale simulations. The PDFs were generated using 20 million prediction points for all three models. While the model trained by 256 training points demonstrates significant discrepancy, the models trained by 512 and 5120 indicates close match. In the remainder of the numerical study, we employ the GP model trained by 5120 training points. Figure 2.10b shows the convergence of the GP model predictions as a function of the number of prediction points. The figure demonstrates that the GP model predictions converge after a relatively large number of prediction points are employed ($\sim$2 million). It is important to note that the

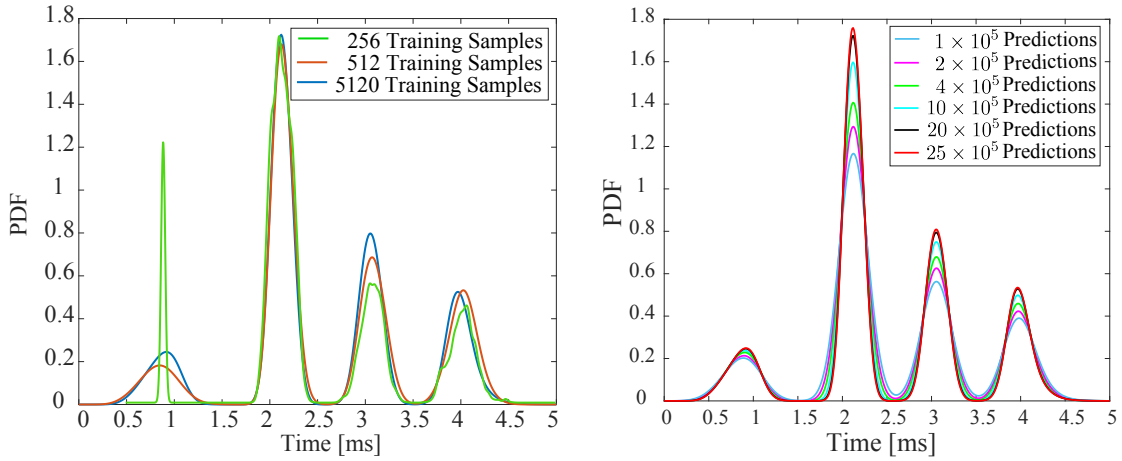

Figure 2.10: Convergence study of GP model with respect to (a) the number of training samples with prediction distributions generated with 2 million samples; and (b) the number of prediction points with the surrogate trained with 5120 samples.

figure illustrates those prediction points that lead to separation. The distributions with low number of prediction points demonstrates a higher ratio of cases in which separation does not initiate.

The performance of the SVM classifier is assessed by the confusion matrix which is generated by a 10-folder cross-validation as shown in Fig. 2.11.

In Fig. 2.11b, all the diagonal terms (indicating correct classification) are greater than 90%, which indicates that the classifier correctly predicts the appropriate parameter subspace with over 90% accuracy. Increasing accuracy is observed as the number of training points increases from 512 (Fig. 2.11a) to 5120 (Fig. 2.11b) employing quadratic SVM classifier.

2.4.1.3 Global Sensitivity Analysis

The parameter boundaries which define the parameter space of interest are provided in Table 2.3. The most sensitive parameters using the first order sensitivity and total effect sensitivity are identified according to the indices of each parameter.

Sensitivity indices, the quantitive representation of parameter contribution to interfacial

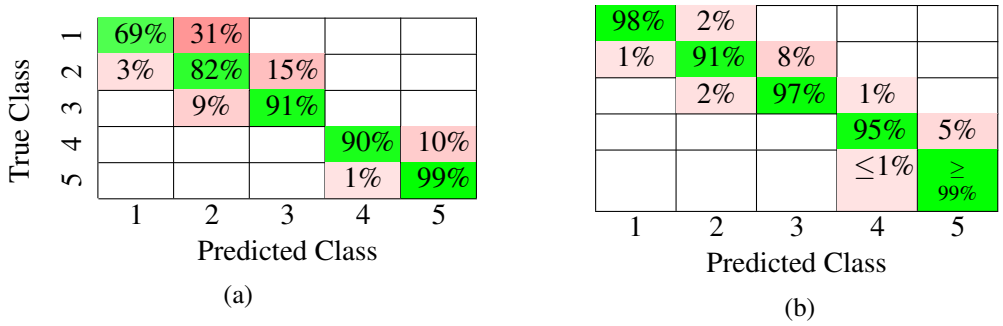

Figure 2.11: Confusion matrix. Class i: separation initiation near the ith step load (i ≤ 4). Class 5: no separation ovserved. (a) confusion matrix trained with 512 samples. (b) confusion matrix trained with 5120 samples.

separation, are shown in Fig. 2.12a. Interface strength $T_{\max}$ is the dominant parameter based on self-contribution as well as parameter interactions. The critical normal separation and G_{h_∞} are also identified as significant uncertainty sources in this system. The higher order interactions between multiple factors significantly increase the sensitivities of Δ_{cn} and G_{h_∞}. Compared to critical normal separation, the critical tangent separation is an insensitive parameter, despite the presence of shear stress concentration as reported in [68]. Prony Series and other interfacial parameters are observed to be insensitive factors as well. Figure 2.12b demonstrates the convergence of the sensitivity measures as a function of the number of prediction samples. The figure indicates convergence with approximately 20 million prediction samples.

2.4.2 Microscale Geometry Sensitivity

The local temperature rise ("hot spots") induced by local microstructure response in multiple particle systems under dynamic loading is of interest, since hot spots are among the failure mechanisms in energetic materials. In the current numerical study, the microscale geometry characteristics of the particulate composite, for example, particle size and particle shape, are parameterized and investigated using the GSA framework.

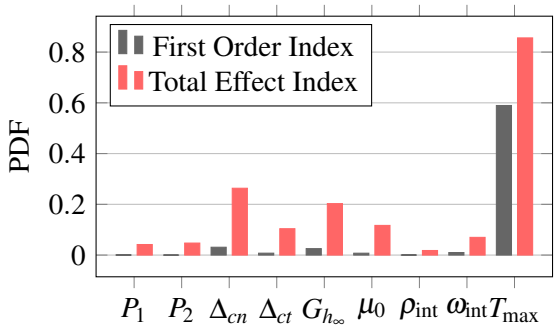

(a) Sensitivity indices for material properties.

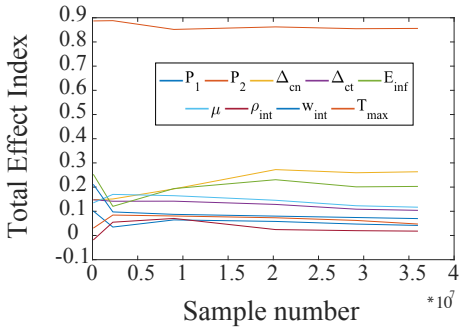

(b) Convergence of S_i^T.

Figure 2.12: Convergence study of GP model with respect to (a) the number of training samples with prediction distributions generated with 20 million samples; and (b) the number of prediction points with the surrogate trained with 5120 samples.

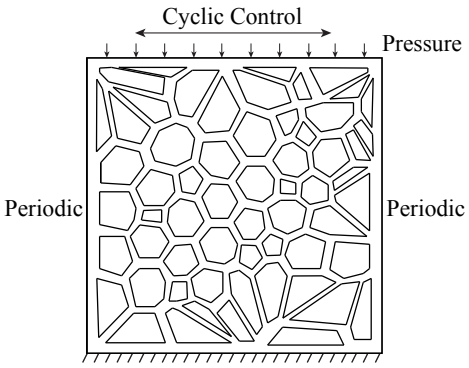

Figure 2.13: Geometry and loading conditions.

2.4.2.1 Microscale Model

In this numerical study, the thermo-mechanical dynamic behavior of a multiple particle AP-HTPB composite specimen under ultrasonic vibration loading is investigated to assess the contribution of geometric parameters on the temperature rise in the specimen. The specimen is idealized as a 3 mm $\times$ 3 mm rectangle with multiple polygons (idealized particles) embedded as shown in Fig. 2.13. The bottom edge is fixed, and the periodic boundary condition is applied on the side edges. Static pressure, $p = 200$ KPa, and a harmonic loading, $d_h = A_v \cdot \sin(2\pi f \cdot t)$, are both applied on the top surface as external excitation. $A_v = 0.03$ mm is the loading amplitude, and $f = 40$ kHz is the ultrasonic

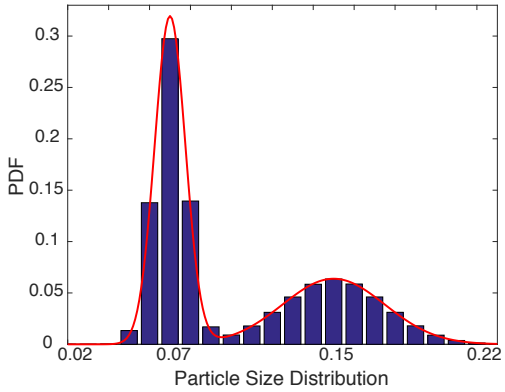

Figure 2.14: Illustration of particle size distribution. Above PDF is subjected to a bimodal distribution with $\mu_1 = 0.15$ mm^2, $\mu_2 = 0.07$ mm^2, $\sigma_1 = 0.025$ mm^2, $\sigma_2 = 0.0075$ mm^2, $w_1 = 0.6$.

frequency.

Microscale geometry of particulate composites is defined by the particle size distribution, the particle shape distribution, and the particle area fraction. The microscale geometry of AP-HTPB system is assumed to be controlled by the above parameterized distribution parameters and constructed by Neper [136], a polycrystalline microstructure generation software. The geometry of the particles obtained from Neper is adjusted to reach the desired area fraction, and the binder model is applied on the gap between the AP particles to include the interaction of particles through the soft HTPB binder. The cohesive zone element is inserted between particle and binder to reproduce the interfacial behavior.

In the context of numerical verifications, a bimodal particle size distribution is assumed [13]:

$$f(A) = w_1 \cdot N(\mu_1, \sigma_1) + (1 - w_1) \cdot N(\mu_2, \sigma_2) \tag{2.42}$$

where w_1 is the weight for the first mode. μ_1 and σ_1 are the mean and variance of the normal distribution of the first mode. μ_2 and σ_2 are the mean and variance of the second mode, as illustrated in Fig. 2.14.

Sensitivities of five microstructure parameters that define the microscale geometry (particle size distribution means μ_1, μ_2, bimodal weight ω_1, particle sphericity distribution

Table 2.6: Parameters boundary in microscale geometry sensitivity study.

Parameter	μ_1	μ_2	μ_s	ω_1	η
Unit	mm^2	mm^2			
Upper bd	0.2	0.07	0.9	1.0	0.9
Lower bd	0.1	0.04	0.8	0.5	0.7

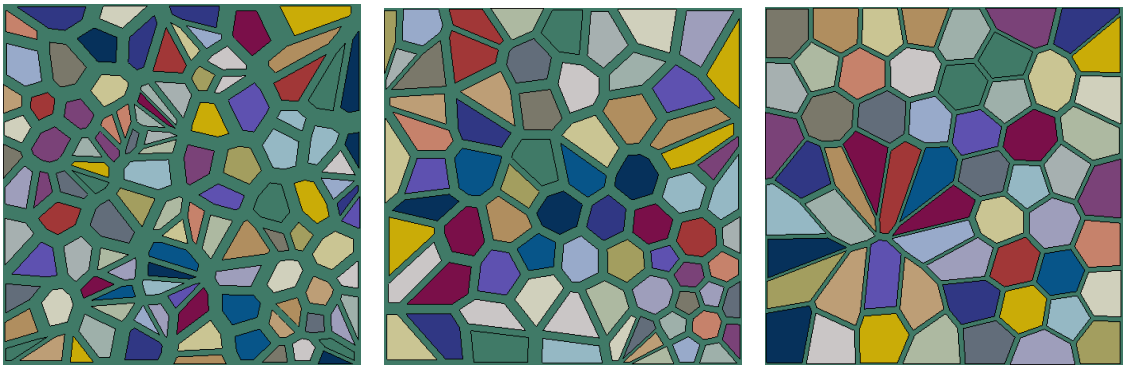

(a) (b) (c)

Figure 2.15: Examples of microscale geometry with size and shape parameters at (a) lower boundaries; (b) mean values; (c) upper boundaries in Table 2.6.

mean μ_s, and area fraction η) are investigated. Similar to the previous example, uniform distribution is assumed for each parameter. The values of parameter ranges are selected according to experimental and numerical energetic microstructure data available in the literature [11, 168, 87, 13, 32, 115, 32, 178, 69] and listed in Table 2.6. Variations of these five parameters directly influence the microscale geometry, and three examples in Fig. 2.15 are employed to demonstrate the influence of the parameters on the resulting microscale geometry. The variance of the first mode and second mode, σ_1 and σ_2 are kept as 0.025 mm and 0.0075, respectively. The variance of sphericity σ_s is selected as 0.15.

Material parameters except the Prony Series (i.e., AP particle properties, interface parameters) set in the previous example are used in the current study as well. Six interfacial parameters and the steady-state shear modulus employed before are assumed to be constants and shown in Table 2.7. Six pairs of Prony Series are employed to represent the viscoelastic behavior of HTPB binder and calibrated from experimental data [20]. The calibrated stress-strain curves using six pairs of Prony Series are plotted in Fig. 2.16, and

Table 2.7: Fixed parameters in microscale geometry sensitivity study.

Parameter	$T_{\max}$	Δ_{cn}	Δ_{ct}	μ_0	w_{int}	ρ_{int}	$G_{h\infty}$
Unit	MPa	mm	mm		mm	g/m^3	MPa
Value	2.91	0.11	0.264	0.2	10^{-3}	$1.45 \cdot 10^{-3}$	2.5

Table 2.8: Calibrated six pairs of prony series.

Parameter	p_1	p_2	p_3	p_4	p_5	p_6
Value	33	30	25	13	8	3
Parameter	q_1	q_2	q_3	q_4	q_5	q_6
Value	$1.04 \cdot 10^{-7}$	$2.1 \cdot 10^{-5}$	$1.66 \cdot 10^{-3}$	$1.05 \cdot 10^{-2}$	$5 \cdot 10^{-2}$	$2.1 \cdot 10^{-1}$

corresponding moduli and relaxation times are shown in Table 2.8.

In order to ensure that the element discretization is sufficient to capture the dynamic response, a mesh convergence study with respect to the target response functions (i.e., temperature) is performed. For a representative case as shown in Fig. 2.17a, the specimen is deformed under ultrasonic loading for 1 ms. The maximum temperature after 1 ms as the response function of the mesh convergence study changes with mesh refinement and its convergence trend is plotted in Fig. 2.17b. When the number of elements reaches to around 6,000, the maximum temperature in the specimen after the ultrasonic excitation is loaded for 1 ms is stable. All forward microscale simulations employ a level of discretization similar to the converged model described in this study.

2.4.2.2 GP Surrogate Model

Although high temperature may exist at multiple local sites within the microstructure, as shown in Fig. 2.18, the maximum temperature within the specimen is chosen as the response function. A GP surrogate is trained to substitute the complex microscale FE simulation (Fig. 2.18). The convergence with respect to the number of training samples is guaranteed by constructing four GP models with 32, 64, 96, and 128 microscale simulations as training points. Four prediction distributions constructed with GP models trained by different sample sizes are compared and the convergence is observed, as shown in Fig. 2.19a. The PDFs were generated using forty million prediction points for all four models. These

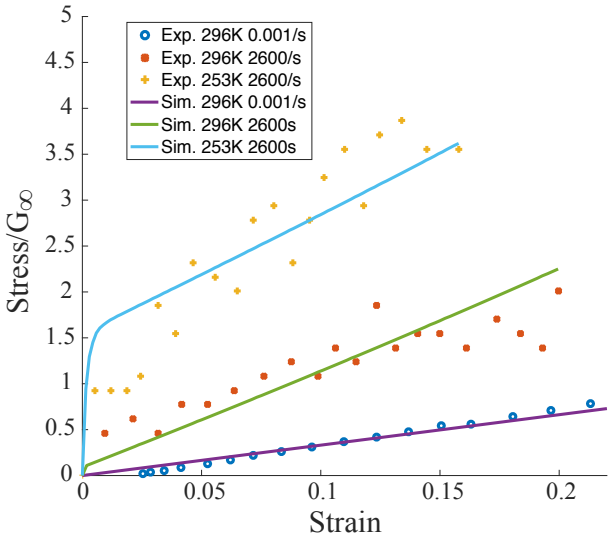

Figure 2.16: Prony Series Calibration

four distributions are not identical, but three of them (produced by GP models trained with 64, 96, 128 samples) are similar and can be regarded as converging. In current study, the GP model with 64 training simulations is employed.

Similar to the previous study, the convergence of prediction distributions should be guaranteed before checking the convergence of the number of training samples. Forty million prediction points are necessary to generate the converged prediction distribution, as shown in Fig. 2.19b.

2.4.2.3 Global Sensitivity Analysis

Five microscale geometry parameters that represent the microstructure characteristics are investigated through the proposed sensitivity analysis framework. Sensitivity indices quantifying contributions from parameters and interactions are obtained, and the dominant parameter is identified.

The sensitivity indices obtained from the GSA framework are shown in the Fig. 2.20a. The results indicate that the area fraction is the dominant parameter that contributes to the temperature rise in the dynamic simulations. The dominant effect of area fraction is primarily due to the higher stress concentrations observed in particles in close proximity

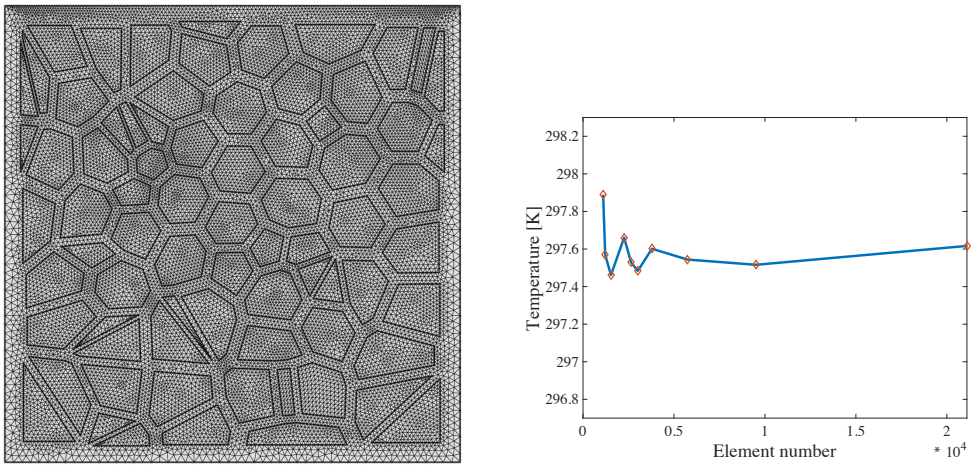

(a) (b)

Figure 2.17: Mesh convergence study of the representative case. (a) Mesh of the representative microstructure with 21104 elements; (b) Element number convergence.

to one another. It is interesting to note that the sphericity parameter appears to have little influence on the localized heating characteristics. This result is surprising since higher stresses are expected near low sphericity particles. This result is attributed to the fact that the parameter range for sphericity is kept relatively narrow in the sensitivity study. This is to avoid the need to employ very fine discretization near narrow edges of the particles. From the physical perspective, it can be speculated that very fine asperities of the particles break off at the early stages of the dynamic loading, rounding the particle geometries prior to the onset of localized heating. Comparing the total and first order sensitivity indices, the contributions of the parameter interactions appear to be significant for particle mean sizes, the weight and sphericity expectation parameters. The larger particle mean size exhibits larger influence than the smaller particle mean size to the maximum temperature within the particulate composite. Figure 2.20b demonstrates the convergence of the sensitivity measures as a function of the number of prediction samples. The figure indicates convergence with approximately 20 million prediction samples.

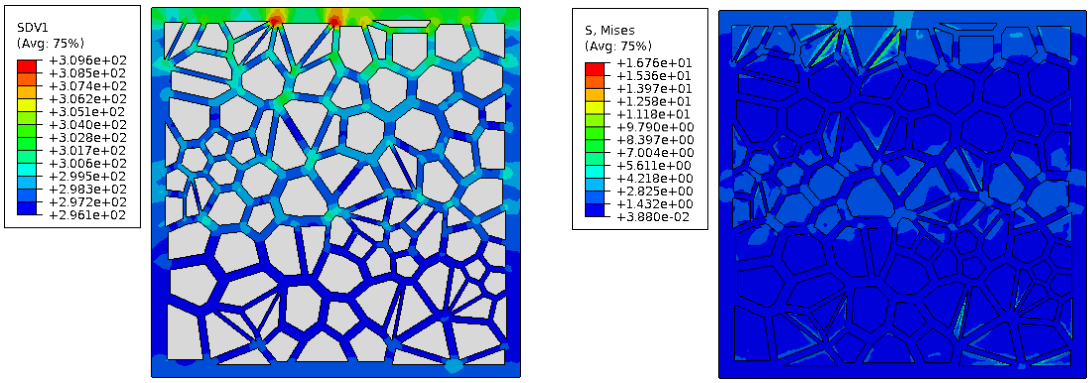

(a) (b)

Figure 2.18: Example of microscale FE simulations of multiple particle systems. (a) Temperature contour of binder at $t = 10$ ms; (b) Von Mises stress contour at $t = 10$ ms.

2.5 Conclusion

This chapter presented a new global sensitivity analysis framework for problems that exhibit discontinuous response functions. The proposed approach has been applied to investigate the role of material and morphological properties of particulate energetic composite materials subjected to dynamic loading conditions. In particular, the following conclusions are drawn: (1) the piece-wise continuous GP model with SVM classier to characterize the continuous subdomains provide a computationally accurate and efficient approach to characterize sensitivities in the presence of response function discontinuities; (2) Interface strength and particle volume fraction are found to be the most influential parameters in the loading regime and microscale morphologies investigated in this study.

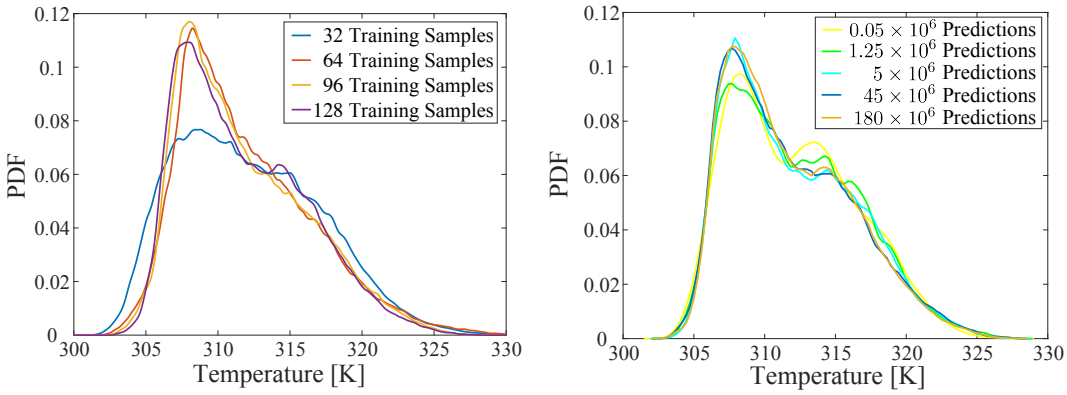

(a) (b)

Figure 2.19: Convergence study of GP model with respect to (a) the number of training samples with prediction distributions generated with 40 million samples; (b) the number of prediction points with the surrogate trained with 128 samples.

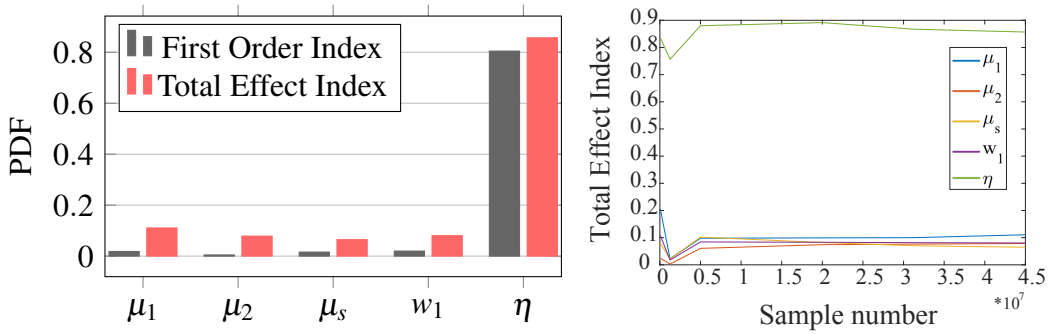

(a) SIs in geometry sensitivity study.

(b) Convergence of S_i^T.

Figure 2.20: Convergence study of GP model with respect to (a) the number of training samples with prediction distributions generated with 45 million samples; and (b) the number of prediction points with the surrogate trained with 5120 samples.

Chapter 3

PLASTIC DISSIPATION SENSITIVITY TO MECHANICAL PROPERTIES IN POLYCRYSTALLINE β-HMX SUBJECTED TO IMPACT LOADING

3.1 Introduction

This chapter focuses on analyzing the anisotropic elasticity and plastic deformation of β-HMX single crystal and polycrystalline subjected to impact loadings. Through the sensitivity analysis studies, monoclinic elastic constants have been analyzed by quantifying their contributions to the material response over a large parameter space. Parameters that control the plastic deformation mechanisms are also analyzed through the sensitivity analysis framework. In particular, two slip mechanisms (thermal activation and phonon drag) and dislocation evolutions (generation and annihilation) are considered as the primary contributing sources to the overall shear strain rate. This investigation help us characterize the orientation dependence and plastic deformation mechanisms of β-HMX crystal, and identify the significance of elasticity and plasticity properties in the dynamic behaviors.

3.2 Constitutive Model of β-HMX

The elasto-plastic response of HMX crystals is modeled using the Crystal Plasticity Finite Element (CPFE) approach, considering that crystallographic slip is an important deformation mechanism in the plastic stage under the moderate impact load regime. The constitutive model employed in this study describes the isothermal and large plastic deformation of the HMX polycrystal. The large deformation kinematic formulation is based on the framework of Marin [100]. A brief overview of this framework is provided below.

3.2.1 CPFE formulation

Consider the body of the polycrystalline solid in its current configuration denoted as $\mathbb{B}$. The initial configuration of the body is denoted as $\mathbb{B}_0$. The motion from $\mathbb{B}_0$ to $\mathbb{B}$ follows the map $\boldsymbol{x} = \boldsymbol{\phi}(\boldsymbol{X},t)$, where $\boldsymbol{x}$ and $\boldsymbol{X}$ represent positions in the current and initial configurations, and t is time. The deformation gradient, $\boldsymbol{F} = \partial \boldsymbol{x}/\partial \boldsymbol{X}$, is decomposed using the classical multiplicative split:

$$\boldsymbol{F} = \boldsymbol{F}^e \cdot \boldsymbol{F}^p = \boldsymbol{V}^e \cdot \boldsymbol{R}^e \cdot \boldsymbol{F}^p \tag{3.1}$$

where $\boldsymbol{F}^e$ is the elastic part of the deformation gradient, $\boldsymbol{F}^p$ represents the plastic deformation which is modeled by dislocation evolution and shear stress induced slip in the crystallographic slip systems. Polar decomposition of $\boldsymbol{F}^e$ generates $\boldsymbol{R}^e$ and $\boldsymbol{V}^e$, where $\boldsymbol{R}^e$ is the orthogonal tensor defining the rotation and reorientation of the grains, $\boldsymbol{V}^e$ is the left stretch tensor representing the pure elastic stretch of the lattice.

Two intermediate configurations, $\bar{\mathbb{B}}$ and $\widetilde{\mathbb{B}}$, are introduced. In what follows, all quantities with tilde and over bar respectively indicate representation in the $\widetilde{\mathbb{B}}$ and $\bar{\mathbb{B}}$ configurations. Plastic update is performed in the intermediate and stress free configuration $\widetilde{\mathbb{B}}$, which is obtained through unloading the elastic stretch, $(\boldsymbol{V}^e)^{-1}$, from current configuration $\mathbb{B}$. The use of two configurations provides a better setting for elastic-viscoplastic behavior, in contrast with a single intermediate configuration approach typically employed for rigid-viscoplastic behavior. The above finite deformation crystal plasticity model is specialized to the case of small elastic strains:

$$\boldsymbol{V}^e = \boldsymbol{1} + \boldsymbol{\epsilon}^e, \qquad \dot{\boldsymbol{V}}^e \approx \dot{\boldsymbol{\epsilon}}^e, \qquad (\boldsymbol{V}^e)^{-1} \approx \boldsymbol{1} - \boldsymbol{\epsilon}^e \tag{3.2}$$

where $\boldsymbol{\epsilon}^e$ is the elastic strain tensor.

The stress-strain relationship is expressed as $\boldsymbol{\tau} = \widetilde{\mathbb{C}}^e : \boldsymbol{\epsilon}^e$, where $\boldsymbol{\tau} = (\det \boldsymbol{F})\boldsymbol{\sigma}$ is the

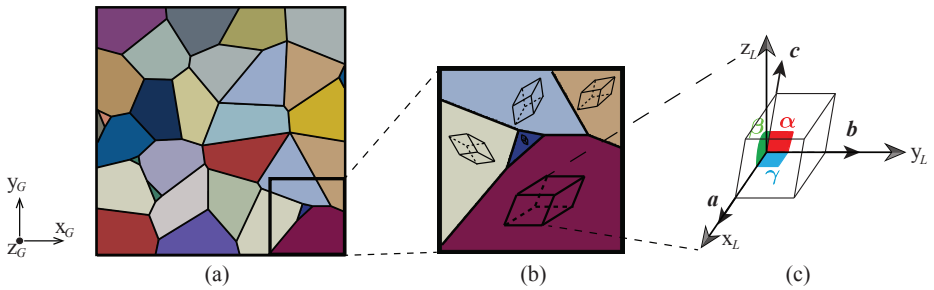

Figure 3.1: Schematic example of polycrystal β-HMX. x_G, y_G and z_G represent the global coordinates, while x_L, y_L and z_L represent the local coordinates. y_L axis is chosen as the unique axis (parallel to $\boldsymbol{b}$) in the monoclinic lattice structure with $\alpha = \gamma = 90°$, $\beta \neq 90°$. The transformation between local coordinates and global coordinates is through Euler angles (Kocks convention).

Kirchhoff stress, $\boldsymbol{\sigma}$ is the Cauchy stress, and $\widetilde{\mathbb{C}}^e$ is the elasticity tensor. For the plasticity behavior, the resolved shear stress (RSS) on the α^{th} slip system, τ^α, is defined by the Schmid's law:

$$\tau^\alpha = \widetilde{\boldsymbol{S}} : \text{sym}(\widetilde{\boldsymbol{C}}^e \cdot \widetilde{\boldsymbol{Z}}^\alpha) \approx \boldsymbol{\tau} : \text{sym}(\widetilde{\boldsymbol{Z}}^\alpha) = \boldsymbol{\tau} : \widetilde{\boldsymbol{Z}}^\alpha \tag{3.3}$$

where $\widetilde{\boldsymbol{S}}$ is the 2^{nd} Piola-Kirchhoff stress, and $\widetilde{\boldsymbol{C}}^e = \boldsymbol{V}^{eT}\boldsymbol{V}^e$ is the right Cauchy-Green tensor. $\widetilde{\boldsymbol{Z}}^\alpha = \widetilde{\boldsymbol{s}}^\alpha \otimes \widetilde{\boldsymbol{m}}^\alpha$ is the Schmid tensor in the α^{th} slip system. $\widetilde{\boldsymbol{s}}^\alpha$ and $\widetilde{\boldsymbol{m}}^\alpha$ are the unit vectors along the slip direction and normal to the slip plane, respectively.

3.2.2 Monoclinic lattice and elasticity

The HMX single crystals are aggregated to form a polycrystalline microstructure with random orientations. The microscale geometry of polycrystal β-HMX is schematically illustrated in Fig. 3.1a, where each polygonal grain represents a single crystal with a prescribed crystal orientation as shown in Fig. 3.1b.

β-HMX crystals exhibit low symmetry with a monoclinic structure (Fig. 3.1c). In this chapter, y_L axis is chosen as the unique axis (parallel to $\boldsymbol{b}$ axis), and x_L axis is parallel to $\boldsymbol{a}$ axis, while z_L axis deviates from the $\boldsymbol{c}$ axis [129]. For β-HMX crystal, the lattice can be represented using either of two unit cells, $P2_1/n$ and $P2_1/c$, with two molecules per unit cell. In the current chapter, all coefficients are given in $P2_1/c$ space group. The

transformation relationship between the two space groups are provided in Ref. [105].

For crystals of low symmetry, such as the monoclinic lattice, deviatoric and hydrostatic components of the response are coupled. Furthermore, at high rate loading conditions, temperature and pressure dependence of the elastic moduli tensor may be prominent [185]. Under moderate impact loading conditions considered in this study, volume change is smaller compared to the plastic deformation, and pressure/temperature variation is relatively small. Thirteen independent coefficients are necessary to fully describe the anisotropic elastic properties of the monoclinic lattice. The elasticity tensor $\widetilde{\mathbb{C}}^e$ for the lattice is expressed in the matrix form as:

$$[\widetilde{\mathbb{C}}^e] = \begin{bmatrix} C_{11} & C_{12} & C_{13} & 0 & C_{15} & 0 \\ C_{12} & C_{22} & C_{23} & 0 & C_{25} & 0 \\ C_{13} & C_{23} & C_{33} & 0 & C_{35} & 0 \\ 0 & 0 & 0 & C_{44} & 0 & C_{46} \\ C_{15} & C_{25} & C_{35} & 0 & C_{55} & 0 \\ 0 & 0 & 0 & C_{46} & 0 & C_{66} \end{bmatrix} \tag{3.4}$$

The elements of the tensor are expressed in the Voigt notation.

For computational convenience, the above elasticity tensor is decomposed to deviatoric and volumetric parts. The deviatoric and volumetric parts of the constitutive law becomes [100]:

$$\begin{aligned} \text{dev}\boldsymbol{\tau} &= \widetilde{\mathbb{C}}^e_d : \text{dev}\boldsymbol{\epsilon}^e + \widetilde{\boldsymbol{H}}^e \text{tr}(\boldsymbol{\epsilon}^e) \\ p_\tau &= (\widetilde{\boldsymbol{H}}^e)^T : \text{dev}\boldsymbol{\epsilon}^e + \widetilde{M}^e \text{tr}(\boldsymbol{\epsilon}^e) \end{aligned} \tag{3.5}$$

where $\boldsymbol{\tau} = \text{dev}\boldsymbol{\tau} + p_\tau \widetilde{I}$, $\widetilde{I}$ is the second order identity, $\widetilde{\mathbb{C}}^e_d$ is the deviatoric part of the elasticity tensor, $\widetilde{\boldsymbol{H}}^e$ is the second order deviatoric-isochoric elastic coupling tensor, and $\widetilde{M}^e$ is the elastic volumetric coefficient. Following Ref. [100], vector representations of the deviatoric stress and strain are expressed using five independent components. The corresponding matrix forms of $\widetilde{\mathbb{C}}^e_d$, $\widetilde{\boldsymbol{H}}^e$ and $\widetilde{M}^e$ derived with respect to the crystal axes of the monoclinic lattice are shown in the appendix.

3.2.3 Flow rule and evolution laws

The form of the kinematic equation includes both the thermal activation and phonon drag mechanisms of dislocation slip. This is due to the fact that the velocity of a dislocation that moves through an array of obstacles such as the internal crystal boundaries [3] is determined by the time required to bypass the obstacles and the time required to move from one obstacle to another [43, 62, 82]. When the dislocation motion is relatively slow (1e-6 m/s - 1 m/s), the dislocation motion is thermally activated, and local obstacles of various types and the Peierls lattice barrier control glide resistance. At faster speeds (>1 m/s), the dislocation motion is drag-dependent, and only weakly depends on obstacles [62]. Hence, the slip rate in slip system α is expressed as:

$$\dot{\gamma}^{\alpha} = \Big(\frac{1}{\dot{\gamma}_w^{\alpha}} + \frac{1}{\dot{\gamma}_r^{\alpha}}\Big)^{-1} \tag{3.6}$$

where $\dot{\gamma}_w^{\alpha}$ and $\dot{\gamma}_r^{\alpha}$ respectively represent the contributions from thermal activation and phonon drag.

The thermally activated slip evolution is expressed as:

$$\dot{\gamma}_w^{\alpha} = \begin{cases} \big(\frac{\dot{\gamma}_{wo}^{\alpha}}{\sqrt{\rho_n}}\big)\Big[\exp\big(-\frac{\Delta G^{\alpha}(\tau^{\alpha})}{\kappa\theta}\big) - \exp\big(-\frac{\Delta G^{\alpha}(-\tau^{\alpha})}{\kappa\theta}\big)\Big] + h(\tau^{\alpha}), & \text{if} \quad |\tau^{\alpha}| \le g^{\alpha} \\ \big(\frac{\dot{\gamma}_{wo}^{\alpha}}{\sqrt{\rho_n}}\big)\text{sign}(\tau^{\alpha})\Big[1 - \exp\big(-\frac{2c_G{\mu^{\alpha}}}{\kappa\theta}\big)\Big] + h(\tau^{\alpha}), & \text{if} \quad |\tau^{\alpha}| > g^{\alpha} \end{cases} \tag{3.7}$$

where $\dot{\gamma}_{wo}^{\alpha}$ is the reference shear strain rate, κ is a constant and θ is temperature. ρ_n is a dimensionless dislocation density measure normalized by the reference dislocation density ρ_{ref} ($\rho_n = \rho/\rho_{\text{ref}}$). $\Delta G^{\alpha}(\tau^{\alpha})$ is given by:

$$\Delta G^{\alpha}(\tau^{\alpha}) = c_G{\mu^{\alpha}}\Big[1 - \Big(\frac{\tau^{\alpha}}{g^{\alpha}}\Big)^{p}\Big]^{q} \tag{3.8}$$

where c_G, p, q are constants, μ^α is the shear modulus resolved in the α^{th} slip system [46]:

$$\mu^\alpha = \boldsymbol{Z}_0^\alpha : \mathbb{C}^e : \boldsymbol{Z}_0^\alpha; \qquad \boldsymbol{Z}_0^\alpha = \boldsymbol{s}_0^\alpha \otimes \boldsymbol{m}_0^\alpha \tag{3.9}$$

g^α is the slip strength of the slip system α, and takes the form:

$$g^\alpha = r^\alpha (g_o + s\sqrt{\rho}) \tag{3.10}$$

where, s and g_o are model parameters, and r^α is the ratio of the slip system strength g^α and the reference slip system strength $g^{(010)[100]}$ ($r^{(010)[100]} = 1$).

The transition from thermal activation to phonon drag is controlled by the penalty function:

$$h(\tau^\alpha) = \text{sign}(\tau^\alpha)(\frac{\tau^\alpha}{g^\alpha})^\zeta \tag{3.11}$$

where ζ is a parameter set to be a large number. The penalty function $h(\tau^\alpha)$ ensures that the phonon drag component of slip is predominant in the presence of overstress (i.e. $\tau^\alpha > g^\alpha$), and it smoothly transitions between the two mechanisms of slip. Figure 3.2 illustrates the role of h on the shifting between the dominant slip mechanism as a function of RSS. At low amplitude of RSS compared with the slip system strength, thermal activation is the dominant slip mechanism, whereas at higher amplitudes of RSS, phonon drag is dominant. In Fig. 3.2, the dislocation density and temperature are taken to be constant (ρ=0.0307 micro-m^{-2} and θ=297 K). The other parameters are set to values indicated in the verification studies below. The smoothness of the transition from thermal activation-dominated to phonon drag-dominated slip is governed by the power constant ζ. For relatively large values of ζ, the behavior is very similar to the unregularized behavior, whereas an appropriate choice for ζ provides a smoother transition, allowing better stabilization in the numerical implementation of the model.

The drag operates as the dislocation bows between obstacles before it cuts or bypasses

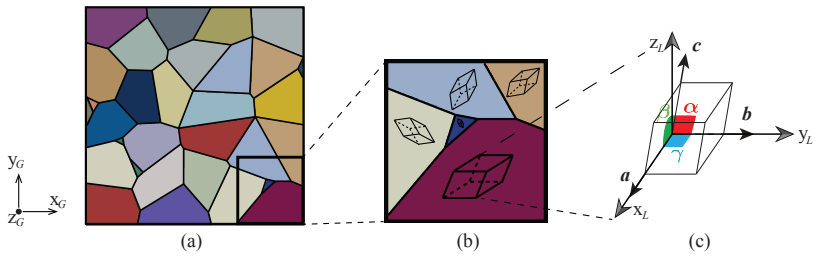

Figure 3.2: Transition between the dominant slip mechanisms using the power-law function $h(\tau^\alpha)$. Dislocation density is of 0.0307 micro-m^{-2} in the illustration. The lines with "$\times\times\times$", "$\circ\circ\circ$", and "$----$" represent the total shear strain rate with ζ equal to 20, 50 and 150, respectively.

them. For the glide of dislocations between sets of obstacles, the slip rate is:

$$\dot{\gamma}_r^\alpha = \dot{\gamma}_{ro}\rho_n\Big[1-\exp\big(-\frac{\tau^\alpha}{D_r}\big)\Big] \quad \text{where} \quad D_r = D_{ro}\frac{\theta}{\theta_0} \tag{3.12}$$

where $\dot{\gamma}_{ro}$ is the reference shear strain rate, D_{ro} is the reference drag stress, and θ_0 is the reference temperature.

The evolution of slip strength is controlled by the dislocation density evolution which, under dynamic loading, evolves through generation and annihilation mechanisms:

$$\frac{d\rho}{d\gamma} = \frac{d\rho^+}{d\gamma} + \frac{d\rho^-}{d\gamma} \tag{3.13}$$

The dislocation generation term [107, 119] is expressed as $d\rho^+/d\gamma = n_1\sqrt{\rho}$. The dynamic recovery term [107] is described by the evolution model $d\rho^-/d\gamma = -n_2\dot{\gamma}^{-\frac{1}{n_3}}\rho$, where n_1, n_2 and n_3 are material parameters, and the net slip system shearing rate is $\dot{\gamma} = \sum_{\alpha=1}^{N}|\dot{\gamma}^\alpha|$.

Under the dynamic loading conditions considered in this study, the dissipation induced by the viscoplastic slip results in localized heating through the adiabatic assumption. The adiabatic temperature evolution is expressed as:

$$c_V\dot{\theta} = \eta\sum_{\alpha=1}^{N}\tau^\alpha\dot{\gamma}^\alpha \tag{3.14}$$

where c_V is the specific heat, and η is the Taylor-Quinney parameter.

It is important to note that earlier works have attributed mechanical deformation in HMX primarily to twinning [3, 90] facilitated by the relatively large size of the molecular crystal (compared to smaller crystals, where twinning is not as prevalent [66]). More recently, through microhardness indentation experiments, Gallagher et al. [45] observed that slip also plays an important role in the deformation of HMX particles. From the standpoint of crystal plasticity modeling, relatively scarce information is available to fully describe mechanical deformation of HMX particles using twinning alone. Of note is the work by [193], who modeled twinning on the $(101)[10\bar{1}]$ as an additional slip system idealized using the same flow and hardening evolution laws as for slip. To the best of the authors' knowledge, the other crystal plasticity modeling studies (e.g., [6, 7, 53, 195, 10, 60, 180, 182, 185, 186]) focused on describing high rate deformation in HMX using slip alone. In view of the potential importance of twinning in describing the mechanical response of HMX, additional development of experimentally-validated CPFE models that include deformation twinning is needed and will be subject of future studies.

3.3 Model Verification

To ensure that the forward model for the energetic material captures the dynamic response with sufficient accuracy, we calibrated the model parameters to values available in the literature and compared the model predictions with those provided in Ref. [10, 107, 109], as well as the experimental results by Dick et al. [37]. The current constitutive model of β-HMX has been verified to assess the effects of (1) specializing the formulation to small elastic strains, and (2) the use of the additional power-law function $h(\tau^\alpha)$. The verified model predictions serve as the starting point for the sensitivity analyses.

Table 3.1: Slip strength ratios.

Slip system	$(010)[100]$	$(011)[100]$	$(01\bar{1})[\bar{1}00]$	$(\bar{1}02)[010]$	$(001)[100]$
Ratio r^{α}	1	0.963	0.963	0.933	1.68
Slip system	$(\bar{1}02)[201]$	$(011)[0\bar{1}1]$	$(0\bar{1}1)[0\bar{1}\bar{1}]$	$(\bar{1}\bar{1}1)[\bar{1}0\bar{1}]$	$(1\bar{1}\bar{1})[101]$
Ratio r^{α}	0.376	0.931	0.931	0.701	0.701

Table 3.2: Flow rule and hardening rule parameters.

Parameter	$\dot{\gamma}_{wo}$	c_G	g_0	s	p	q	$\dot{\gamma}_{ro}$	D_{ro}
Value	1	11.47	103	0.1666	1	1	2.5	1160
Unit	micro-s^{-1}	K/MPa	MPa	MPa· micro-m			micro-s^{-1}	MPa
Parameter	n_1	n_2	n_3	c_V	η	θ_0	ρ_0	ρ_{ref}
Value	37.99	62	4.98	1	0.9	293	0.0307	0.452
Unit	micro-m^{-1}			kJ/(kg · K)		K	micro-m^{-2}	micro-m^{-2}

3.3.1 Parameter calibration

The thirteen constants of the anisotropic tensor of elastic moduli of the monoclinic lattice are set to those calculated by Sewell et al. [153] through MD simulations. The density and specific heat of β-HMX crystals are set to 1.9 g/cm^3 and 1 kJ/(kg·K), respectively. The lattice structure of β-HMX is described by four cell parameters: a, b, c and β. These parameters are typically pressure dependent [30]. In view of moderate load amplitudes, the lattice parameter are taken as constants (a=6.54 Å, b=11.05 Å, c=8.70 Å, and β=124.3°).

The CPFE model incorporates ten slip systems [7] for the monoclinic lattice structure of β-HMX in the $P2_1/c$ space group as summarized in Table 3.1. Slip systems and the corresponding strength ratios (r^{α}) are summarized in Table 3.1.

Table 3.2 presents the values of the parameters associated with slip and CRSS evolution in the crystal plasticity model. The values of the model parameters are set to those proposed in Ref. [10]. The parameter n_2 for dynamic recovery is not provided in the aforementioned reference. Experimental data for HMX necessary to calibrate n_2 is not available. We estimated the value of n_2 by comparing the hardening rate of PBX 9501, whose main component (95% wt) is β-HMX. For PBX 9501 that was compressed at the room temperature (25°C) at a constant strain rate of 2000 s^{-1} [52], the hardening rate ($\partial\sigma/\partial\gamma$) as a

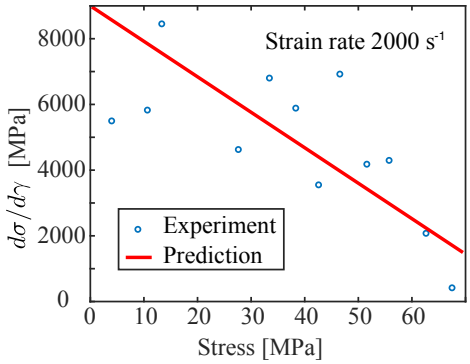

Figure 3.3: Hardening rate-stress curve at constant strain rate 2000 s^{-1}. The hardening rate is estimated by the finite difference method, where the stress and strain data are extracted from experimental measurements by Gray et al. [52] at room temperature.

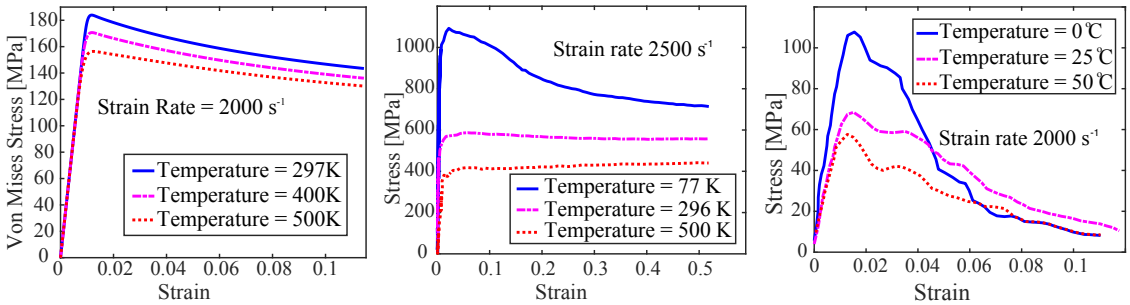

Figure 3.4: Stress-strain curves at different temperatures for (a) HMX in (011) direction at the constant strain rate of 2000 s^{-1} predicted by the calibrated CPFE model, (b) experimentally observed behavior of Vanadium (experimental data from [173]) at the strain rate of 2500 s^{-1} and (c) experimentally observed behavior of PBX 9501 (experimental data from [52]) at the strain rate of 2000 s^{-1}.

function of stress at a constant slip rate 2000 s^{-1} is compared with the model predictions using n_2=62 in Fig. 3.3.

Figure 3.4 shows temperature dependence of the constitutive behavior of the calibrated CPFE model compared with PBX 9501 and a BCC crystal, which exhibit qualitatively similar temperature dependence of yielding. As observed in Fig. 3.4b, the stress-strain curves for Vanadium at different temperatures reported in Ref. [173] show that higher temperatures reduce the yield strength of the material. A similar trend, in Fig. 3.4c, has been observed for PBX 9501 as measured by Gray et al. [52]. The constitutive law employed in

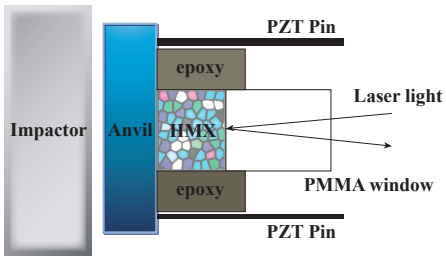

Figure 3.5: Schematic representation of experimental setting.

the current study also exhibits a reduction in the yield strength with temperature as shown in Fig. 3.4a.

3.3.2 Verification study

The capabilities of the crystal plasticity model as well as its implementation have been verified by comparing its predictions to a similar model and experimental observations described in Ref. [37]. The assessment of the current model was performed in the context of the dynamic behavior of single crystal β-HMX specimens subjected to gas gun shots.

The setup of this verification study is shown in Fig. 3.5. An initial velocity is applied on the impactor (2024 Al). The dynamic wave passes to HMX specimen through the anvil (X-cut quartz anvil for impact velocity $\sim$300 m/s, and Kel-F [1] anvil for impact velocity $>$500 m/s). PMMA was chosen as the window material due to the fact that its shock impedance is close to but slightly lower than that of HMX. The slight impedance mismatch results in a rarefaction wave back to the HMX specimen after the incident wave hits the material interface. The specimen and load configurations of the six experiments are listed in Table 3.3 where sample type represents the loading direction in $P2_1/n$ space group. The thicknesses of the HMX specimens varies from 1.23 mm to 4.66 mm. Initial velocities of the impactor are approximately 300 m/s except for "Shot 1182" which was approximately 520 m/s.

Menikoff et al. [112] used linear Hugoniot with Mie-Gruneisen Equation Of State

[1] (Kel-F is the 3M Company brand name for polytrifluorchlorethylene)

Table 3.3: Specimen and load configurations.

Shot no.	Sample type	Thickness (mm)	Impactor Velocity (m/s)
1180	110	1.23	318.5
1166	110	3.18	306.8
1182	110	3.57	520.9
1181	011	1.39	316.0
1068	011	3.00	314.0
1168	011	4.66	313.2

(EOS) for the impactor and anvils, and the shock state in the anvil is used to set the initial conditions that drive the simulations. In the current study, explicit dynamic simulations have been performed without detailed shock analysis. The loading is applied as prescribed constant velocity on the left edge of the specimen. The amplitude of the applied velocity is determined using the measured impactor velocity through the impedance matching technique, in which linear Hugoniot relationships are employed for the impactor, anvils and HMX [112, 16]. The PMMA window near the right edge of the specimen is modeled using the nonlinear viscoelastic constitutive law developed by Schuler and Nunziato [150].

In the current verification study, a quasi-one-dimensional model is employed. Dislocation density field is taken to be uniform prior to the onset of the dynamic load. The FE model contains a line of 3D hexahedral element with a total length 8.6 mm. This length ensures that there is no wave reflection during the simulation duration (1.6 micro-s). The viscoelastic PMMA window is bonded to the HMX specimen. Periodic boundary conditions are applied at the top/bottom and front/back boundaries. Barton et al. [10] observed a discrepancy between the times of arrival in the predictions and experiments due to the dependence of elastic parameters to pressure and temperature and reported the prediction results with a time shift. In the current simulations a time shift of 0.08 micro-s is used.

Verification data are collected from three shots along $(110)_{P2_1/n}$ direction and three shots along $(011)_{P2_1/n}$ direction. The predictions of the current model, predictions in Ref. [10] and experimental measurements are compared in Fig. 3.6. Overall, a reason-

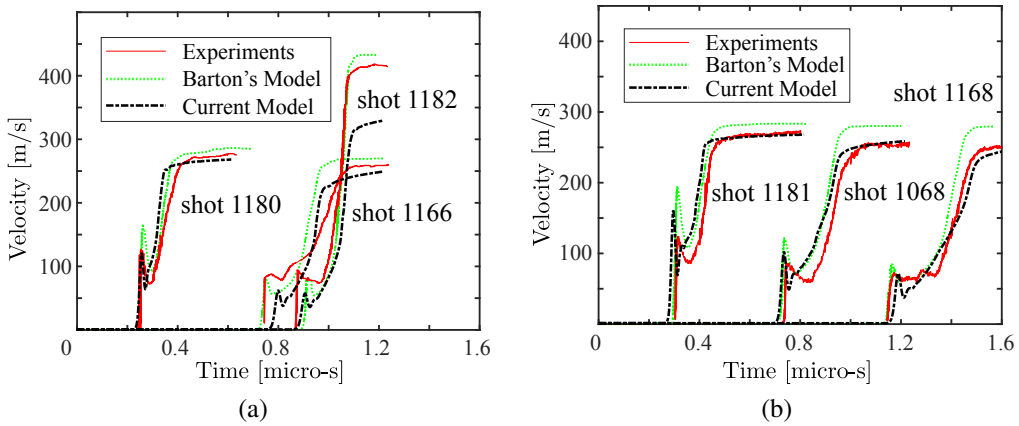

Figure 3.6: Model verification with respect to loading in (a) the $(110)_{P2_1/n}$ direction; and (b) the $(011)_{P2_1/n}$ direction.

able agreement between the predictions and experimental data particularly for the impactor velocity of 300 m/s is observed. This indicates that the proposed model adequately captures viscoplastic response mechanisms. The experimentally observed peaks of the plastic waves (particle velocity at the HMX-PMMA interface) are captured by the current model in all shots ($< 5\%$ error) with the impactor velocity around 300 m/s. A larger discrepancy has been observed in shot 1182. A possible reason for this discrepancy is that the higher initial velocity of the impactor (520.9 m/s) in this shot results in the formation of a stronger shock. Capturing the propagation of the stronger shock requires incorporation of the Equations-of-State (EOS) for the materials into their constitutive models.

3.4 Sensitivity Analyses

Employing the verification study and the associated model parameters as baseline, we performed sensitivity analyses to understand the relative roles of the material parameters and viscoplastic mechanisms on the response of β-HMX subjected to impact loading. The analyses are performed in the context of impact response of a single crystal, as well as polycrystalline microstructures.

3.4.1 Parameters subspace

The sensitivity analyses have been performed to understand the behavior of a range of parameters that define the elastic and plastic behavior of the energetic crystals. In the subsequent analyses, we restrict the parameter subspaces to a range centered around the set of parameters calibrated for the numerical verification study. The parameter ranges are selected such that the parameter subspace reasonably spans the experimental observations and computationally feasible, i.e., surrogate models can be constructed with a reasonable number of training simulations.

3.4.1.1 Elastic coefficients ranges

Ranges of the elasticity coefficients are estimated through the available experimental measurements and molecular simulations. Zaug [194] determined thirteen elastic constants via Impulsive Stimulated Light Scattering (ISLS) after the ultrasonic sound speed measurements in single crystal β-HMX at various temperatures. Stevens and Eckhardt [163] measured the complete elasticity tensor for crystalline β-HMX by scattering from a variety of acoustic phonons. Sun et al. [165] used the Impulsive Stimulated Thermal Scattering (ISTS) method to resolve the thirteen elastic constants from acoustic velocity measurements using samples cut parallel to three different crystal planes. Sewell et al. [152] employed two primary simulation cells with 48 and 96 molecular respectively to calculate the thirteen elasticity constants. Sewell et al. [153] also used atomistic simulations to calculate the isothermal elastic properties of HMX crystal. Cui et al. [30] investigated the mechanical properties (elastic coefficients, Young's modulus, shear modulus and others) of β-HMX at different temperature and pressure by performing isothermal-isobaric molecular dynamics simulations.

In Zaug's experiments, five (C_{11}, C_{33}, C_{55}, C_{15}, C_{35}) of the thirteen coefficients were well determined while others were not. C_{33}, C_{55} and C_{15} have significant discrepancies with the molecular dynamics predictions [153]. Among the remaining coefficients, C_{22} and C_{46}

Table 3.4: Parameter ranges of elasticity coefficients (unit: GPa).

Parameter	C_{33}	C_{44}	C_{55}	C_{66}	C_{12}	C_{13}	C_{23}	C_{15}	C_{25}
Zaug [194]	17.6	2.9	6.6	3.8	4.0	13.0	6.6	0.6	-1.5
Sewell [152]	17.8	9.1	9.2	9.8	5.9	8.4	8.2	-1.1	3.2
Sewell [153]	23.4	9.2	11.1	10.1	9.6	13.2	13.0	-0.1	4.7
Stevens [163]	12.44	4.77	4.77	4.46	6.37	10.5	6.42	-1.1	0.83
Sun [165]	18.24	9.92	7.69	10.67	9.65	9.75	12.93	-0.61	4.89
Cui [30]	13.2	6.41	4.04	4.68	3.75	4.66	5.07	-0.15	-2.71
Upper boundary	24.0	10.0	12.0	11.0	10.0	18.0	13.0	1.0	5.0
Lower boundary	11.0	2.0	4.0	3.0	3.0	4.0	5.0	-5.0	-3.0

are within a reasonably tight range. Hence, four coefficients (C_{11}, C_{35}, C_{22}, C_{46}) are taken as constants and excluded from sensitivity studies. C_{33}, C_{44}, C_{55}, C_{66}, C_{12}, C_{13}, C_{23}, C_{15} and C_{25} are regarded as variables whose ranges are selected to span the values available in the literature and summarized in Table 3.4.

3.4.1.2 Plastic deformation properties

Compared with the elastic constants, identification of appropriate parameter subspaces for plastic behavior is more challenging. This is due to the fact that different models available in the literature employ different internal state variables and evolution forms to describe the slip and strength evolution, and that relatively small number of studies focused on accurate characterization of these parameters. The current crystal plasticity model consists of 16 parameters to describe the slip evolution by thermal activation ($\dot{\gamma}^{\alpha}_{wo}$, c_G, p, q, ζ), slip evolution by phonon drag ($\dot{\gamma}^{\alpha}_{ro}$, D_{ro}, θ_o), hardening evolution (g_o, s), adiabatic temperature evolution (c_V, η) and dislocation evolution (n_1, n_2, n_3, ρ_0). In what follows, we focus on the investigation of the phonon drag, thermal activation and dislocation evolution mechanisms. ζ controls the smoothness of the transition of dominant slip mechanism. It is employed for convergence control in this study and set to $\zeta = 150$. The reference temperature θ_o is set as constant (i.e., the room temperature). p and q, which influence low-rate hardening behavior, are also taken as constants (set to unity). The remaining 8 parameters ($\dot{\gamma}^{\alpha}_{wo}$, c_G, $\dot{\gamma}^{\alpha}_{ro}$, D_{ro}, ρ_o, n_1, n_2, n_3) are considered as variables in the sensitivity analysis stud-

Table 3.5: Ranges for the plastic parameters.

Parameter	$\dot{\gamma}_{wo}$	c_G	$\dot{\gamma}_{ro}$	D_{ro}	ρ_0	n_1	n_2	n_3
Unit	micro-s^{-1}	K/MPa	micro-s^{-1}	MPa	micro-m^{-2}	micro-m^{-1}		
Upper bound	1.5	12.5	3.75	1740	0.046	56.99	93	7.47
Lower bound	0.5	5.735	1.25	580	0.0153	18.99	31	2.49

ies below. In view of limited information available, we set the range for each parameter to be $[50\%\mu, 150\%\mu]$, where μ is the calibrated values shown in Table 3.2, with the exception of c_G and ρ_0. The upper limit of c_G is slightly reduced since high values require very significant time step size reduction for convergence in CPFE simulations. The upper and lower bounds for the parameters are summarized in Table 3.5.

3.4.2 Single crystal sensitivity analysis

The response of single crystal β-HMX subjected to impact loading described in Section 4 is employed to investigate the parametric sensitivities. In the first case, the anisotropic elastic properties in β-HMX single crystal are investigated to understand the role that crystal elasticity plays in the material dynamic behavior. In the second case, the relative roles of the viscoplastic deformation mechanisms are investigated by considering the experimental setup for shot 1166 shown in Table 3.3. In both cases, sensitivities are assessed based on the maximum rise in temperature within the specimen.

3.4.2.1 Elasticity coefficients

Approximately 3,000 forward simulations were performed with parameters randomly sampled from parameter ranges shown in Table 3.4 assuming uniform distribution for each parameter. Approximately 272 million predictions were then generated using the surrogate model to collect information of the response surface over the entire parameter space. In this study, only the elastic parameters are considered as variables, whereas all plastic parameters are set to values in Table 3.2.

First order and total effect sensitivity indices computed for elastic coefficients are shown

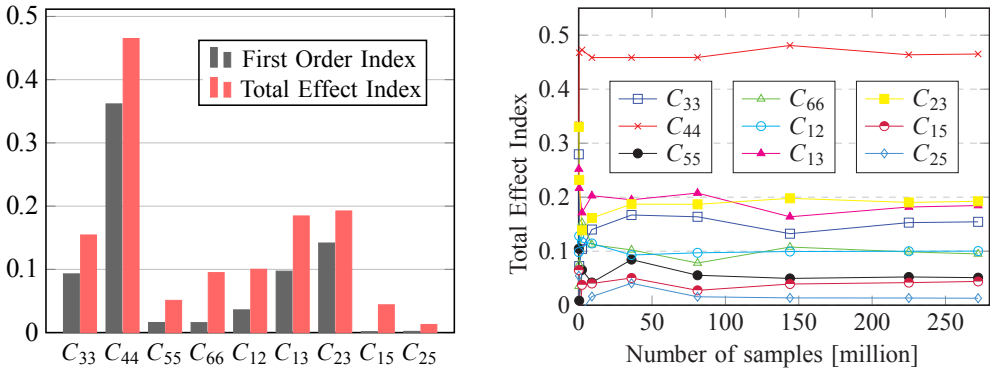

Figure 3.7: Summary of (a) sensitivity indices and (b) convergence for elastic coefficients in single crystal specimen.

in Fig. 3.7a. The figure indicates C_{44} (or C_{2323} in expended notation) is the most sensitive parameter in terms of the maximum temperature rise. The temperature rise is due to the plastic processes (Eq. 3.14), and thermoelastic heating is neglected in the analyses. C_{55}, C_{15} and C_{25} have negligible influence on the plasticity and peak temperature under the impact load in $(110)_{P2_1/n}$ direction. The convergence for each index as a function of number of prediction points is shown in Fig. 3.7b.

Figure 3.8 demonstrates the sensitivities of the nine elastic constants (displayed as probability distributions) computed using the One-at-A-Time (OAT) method with the same surrogate model in GSA. In the OAT method, the sensitivity of a single parameter is computed by sampling that parameter from within its range, while keeping all other parameters fixed at the mean. OAT therefore provides "local" variability of the response as a function of that parameter. In contrast with GSA which identifies C_{13} as the third sensitive parameter based on both FOI and TEI, varying C_{13} alone generates the largest temperature variation ($\approx$14 K). This discrepancy points to the fact that characterization of the variation in the response surfaces locally (such as captured by the OAT method) provides an incomplete description and assessment of sensitivity. Separately varying the parameters C_{25}, and C_{55} does not produce significant temperature variation ($<$3 K), which is consistent with the results shown

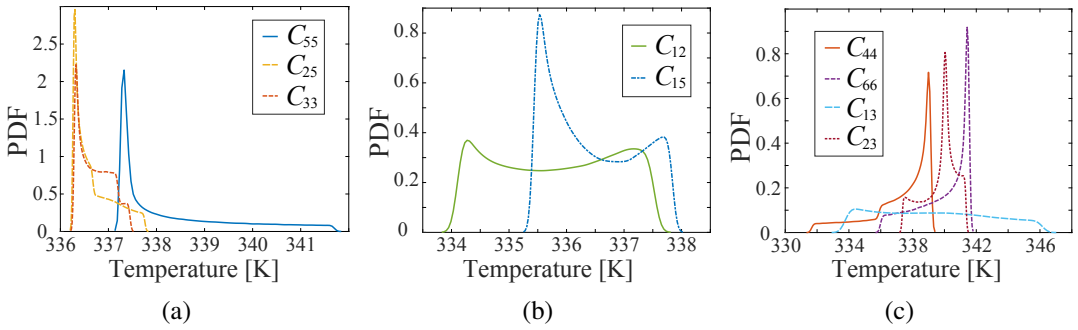

Figure 3.8: Probability distributions for peak temperature resulting from the OAT analysis of individual elastic constants for single crystal cases.

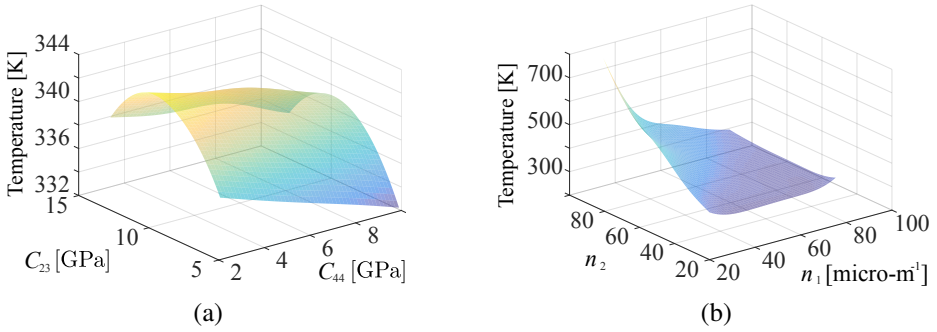

Figure 3.9: Variation of peak temperature over (a) C_{44}-C_{23} plane and (b) n_1-n_2 plane for single crystal specimen.

in Fig. 3.7a.

Interaction between C_{44} and C_{23}, the two most sensitive parameters identified by GSA, are further investigated by plotting the variation of peak temperature over the C_{44}-C_{23} plane, as shown in Fig. 3.9a. Within the given parameter range, the temperature distribution with respect to C_{23} is convex for a fixed C_{44}, whereas the variation with C_{44} is linear for a fixed C_{23} value. The fairly uniform variation of the temperature field indicates only a mild interaction between the two most sensitive elastic constants. The peak of this surface occurs near (C_{44}, C_{23}) = (2.0, 10.0) with maximum temperature around 343 K.

3.4.2.2 Plastic deformation mechanisms

Approximately 3,500 microscale simulations were performed as the training set of the GP model that has the target function of maximum temperature rise under the applied

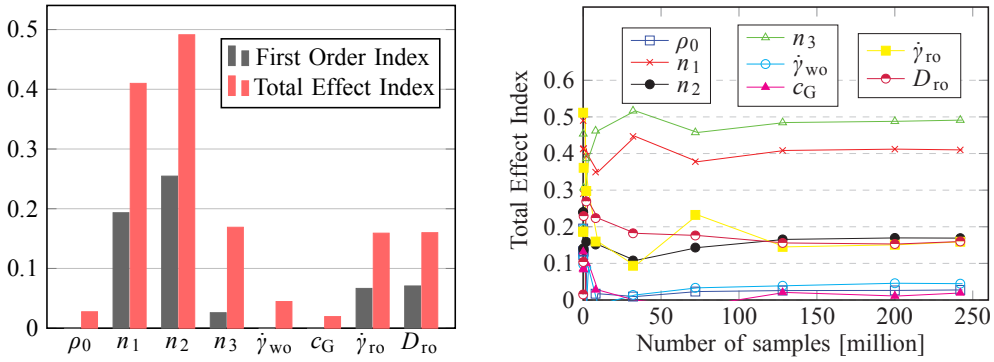

Figure 3.10: Summary of (a) sensitivity indices and (b) convergence for plastic parameters in single crystal specimen.

impact load. 242 million predictions were then generated by the surrogate to study the variation of the target function and compute the sensitivity indices. In this study, only the plastic parameters are considered as variables, whereas elastic constants are set to values calculated by Sewell et al. [153].

Figure 3.10a shows the sensitivity indices for all eight plastic parameters. The convergence of the sensitivity values as a function of the number of prediction points is shown in Fig. 3.10b.

The dislocation annihilation coefficient n_2 and the dislocation generation coefficient n_1 are identified as the most influential parameters. The significance of dislocation evolution parameters indicates that the material impurities or defects govern the plastic deformation in terms of temperature rise regardless of which of the slip mechanism is predominant. The parameters, c_G and $\dot{\gamma}_{wo}$ that control the thermal activation mechanism, have little effect, which indicates that under given impact velocity (≈300 m/s), thermal activation does not contribute significantly to the plastic deformation compared with the phonon drag mechanism, and this is consistent with Ref. [62]. Furthermore, the initial density of dislocation prior to the onset of the impact loading appears to have insignificant effect on the plastic behavior of the crystal. It is important to note that the void collapse mechanism under shock loading was observed to be sensitive to initial dislocation density in Ref. [10]. Void

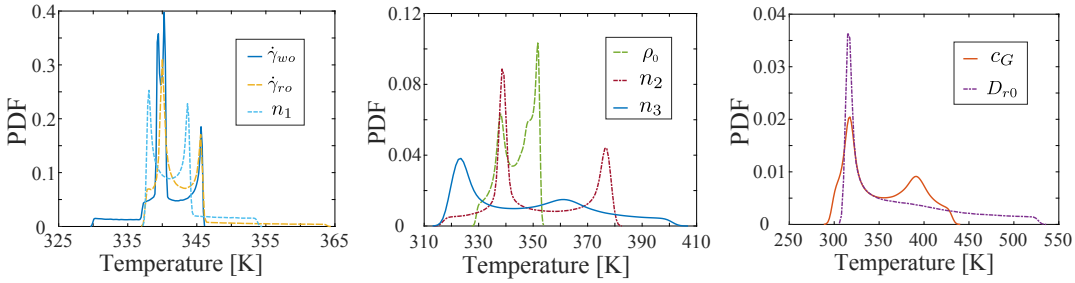

Figure 3.11: Probability distribution for peak temperature resulting from the OAT analysis of individual plastic parameters for single crystal specimen.

collapse behavior therefore appears to be substantially different than the shear dominated viscoplastic process probed in this study

The peak temperature distribution for each parameter obtained by the OAT method is plotted in Fig. 3.11. Near the calibrated parameter set, varying D_{r0} generates the largest temperature variation (of approximately 200 K). However, D_{r0} is identified as the fourth sensitive parameter using the TEI and the third sensitive parameter using the FOI. The two most sensitive parameters identified by TEI, n_1 and n_2, generates small temperature variations ($\approx$15 K and 70 K) compared with D_{ro} in the OAT analysis. These discrepancies show that the plastic processes are sensitive to the change and interaction of material parameters, which makes the GSA meaningful as it accounts for the parameter variance and relation. Varying the parameter $\dot{\gamma}_{w0}$ does not produce significant temperature rise ($\approx$15 K) consistent with GSA results. As c_G directly amplifies or reduces the activation energy, it also offsets the ratio τ^{α}/g^{α} at which the transition from thermal activation mechanism to phonon drag mechanism occurs.

The variation of peak temperature over the n_1-n_2 plane is plotted in Figure 3.9b. The maximum temperature occurs near the (n_1, n_2) = (20, 100) corner, which indicates that lower n_1 (i.e., less dislocation generation) and higher n_2 (i.e., more dislocation annihilation) generate more severe plastic deformation whose work is represented by temperature rise up to 800 K subjected to the given load. Compared with the mild interaction observed in

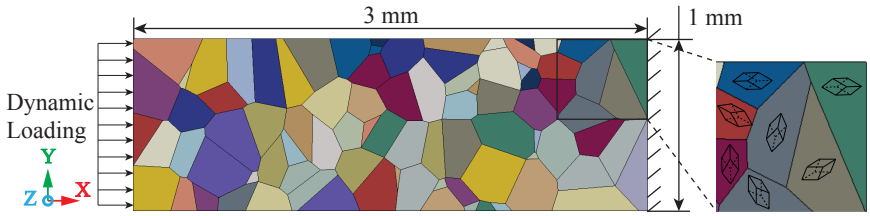

Figure 3.12: Polycrystal specimen geometry. For the first normal distribution of particle size, $N(\mu_1, \sigma_1)$, the weight w=0.2, μ_1=61.8 micro-m, σ_1=13.9 micro-m. For the second normal distribution $N(\mu_2, \sigma_2)$, μ_2=225.7 micro-m, σ_2=44.9 micro-m.

Figure 3.9a, the shape of temperature variation as a function of the two parameters also indicate that there is a strong interaction effect in this case. This is also apparent from the relatively large discrepancies between the first order and total effect indices shown in Fig. 3.10a.

3.4.3 Polycrystalline sensitivity analysis

Parameter sensitivity analysis within a polycrystalline microstructure is also of significant interest, as such an analysis explains the behavior at the scale of a particle. In this section, we investigate the sensitivity of elasticity and plasticity within polycrystalline HMX subjected to impact loading.

Figure 3.12 shows the morphology, loading and boundary conditions of the microstructure considered in this study. The mesh of the microstructure consists of 33,530 wedge elements to capture the localized stress evolution and heat generation. The size of the numerical specimen is 3 mm $\times$ 1 mm that is made of 91 single crystals with random orientations sampled from uniform random distribution. The impact loading is applied from the left edge of the specimen, where the edge velocity is linearly increased from rest to 250 m/s in 10 ns and kept constant thereafter. The total duration of each microscale simulation is 1 micro-s, with time step size of 1e-6 micro-s. The geometry is modeled as a quasi 2D domain with three dimensional discretization constrained in the third (out of plane) direction with a single set of elements along the thickness direction.

The size of the grains are sampled from a bimodal distribution, which is constructed

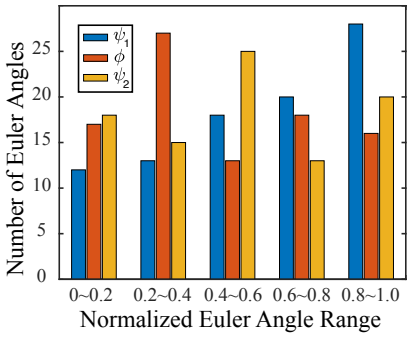

Figure 3.13: Crystal orientation histogram for the specimen in Fig. 3.12. The x axis is the normalized angle range ($0 < \psi_1/(2\pi) < 1, 0 < \phi/\pi < 1, 0 < \psi_2/(2\pi) < 1$).

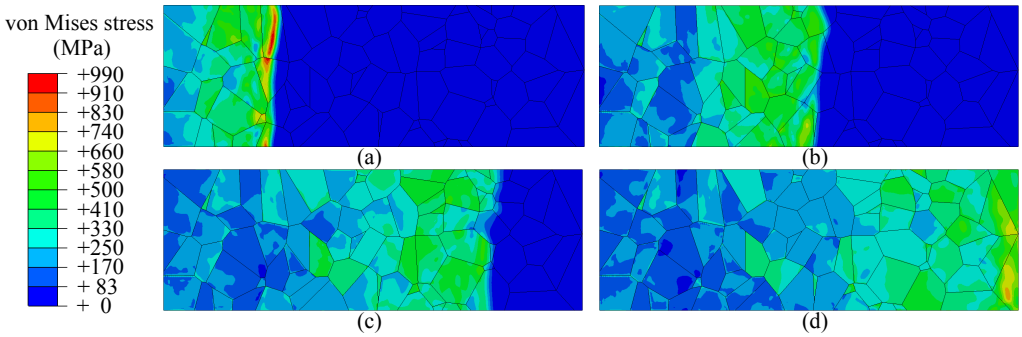

Figure 3.14: Von Mises stress contours at (a) t =0.25 micro-s, (b) t =0.5 micro-s, (c) t =0.75 micro-s, and (d) t =1.0 micro-s.

according to the following available experimental data and numerical investigations [60, 138, 157, 193]. Previous studies in energetic crystals point to a strong crystal size effect on the hot spot formation and initiation sensitivity, where the temperature rise is correlated with the square root of the crystal diameter [2, 3]. The current study does not consider a size-dependent constitutive behavior. The Euler angles (Kocks convention) defining the orientation of a crystal is assumed to be independent of each other, and subjected to a uniform random distribution within the given range ($0 < \psi_1 < 2\pi$, $0 < \phi < \pi$ and $0 < \psi_2 < 2\pi$). The normalized histogram of the Euler angles of all crystals of the polycrystal specimen is shown in Fig. 3.13.

Figure 3.14 illustrates the stress contours as the stress wave progresses through the polycrystal specimen generated using the model parameters stated in Section 4. Local stress concentrations are apparent particularly along grain boundaries and triple junctions.

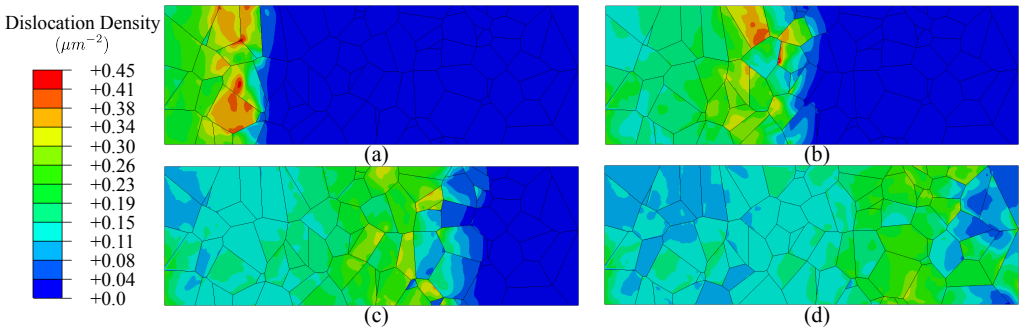

Figure 3.15: Dislocation density contours at (a) t =0.25 micro-s, (b) t =0.5 micro-s, (c) t =0.75 micro-s, and (d) t =1.0 micro-s.

The dislocation density generation and annihilation continuously drive local increase or decrease of the material strength, slip and plastic work in a complex fashion. Evolution of dislocation density distribution over the specimen is shown in Fig. 3.15. The misorientation between adjacent grains leads to the concentration of dislocations along grain boundaries and within particles.

Similar to the previous study, the primary response function of interest is the peak temperature within the domain, which represents the most critical dissipative state across the microstructure. In what follows, the microstructural morphology is fixed and we focus on the analysis of the effects of elastic and plastic properties of the polycrystal.

3.4.3.1 Elasticity coefficients

Approximately 2,000 forward microscale simulations are performed with randomly sampled parameters to serve as training data set for the GP model, and 140 million predictions were made using the surrogate to compute sensitivity indices.

Figure 3.16a shows the sensitivity indices for the elastic parameters along with sensitivity convergence plot as a function of sample size. The plot clearly indicates that C_{33} is the most sensitive parameter under given impact loading. C_{33} is the lone volumetric component among these nine coefficients, and the corresponding high sensitivity is due to the confinement effect induced by the boundary condition employed in the lateral direction.

OAT variabilities of the elastic parameters are plotted in Fig. 3.17. C_{13} and C_{66} sep-

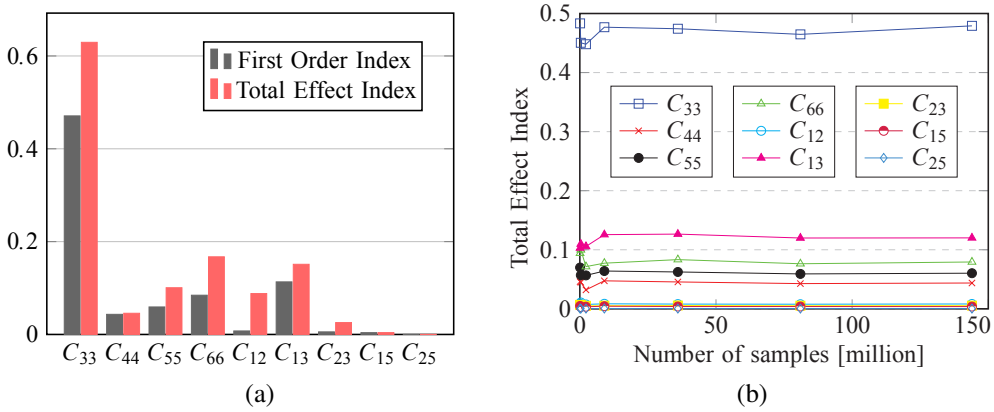

Figure 3.16: Summary of (a) sensitivity indices and (b) convergence for elastic parameters in polycrystal specimen.

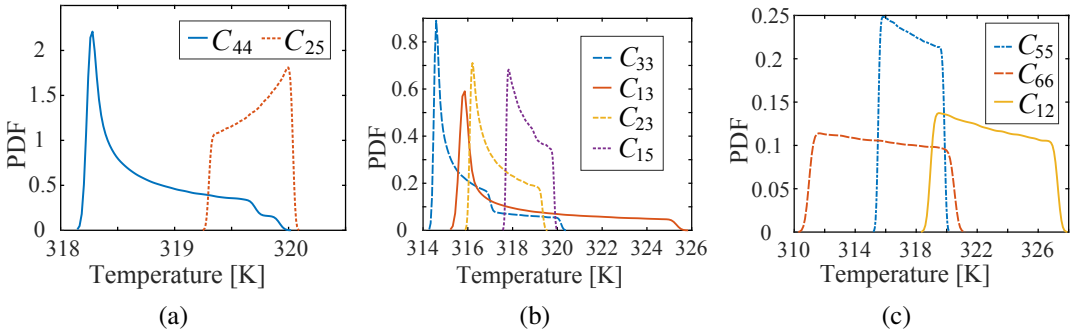

Figure 3.17: Probability distributions for peak temperature resulting from the OAT analysis of individual elastic constants for polycrystal specimen.

arately generate the largest temperature variations (∼11 K) even though they are far less sensitive compared with C_{33} across the parameter subspace investigated in this study. Separately varying the parameter C_{15}, C_{25} and C_{44} does not produce significant temperature rise (<3 K), which is consistent with the corresponding low sensitivity indices in Fig. 3.16a. The variation of peak temperature over C_{33}-C_{66} plane is shown in Fig. 3.18a. Similar to the single crystal case, the plot indicates a convex shape with varying C_{66} for fixed C_{33} and a linear variation with C_{33} for a fixed C_{66}. In the present case, the curvature does vary with the value of C_{33}, which indicates some interactive effects between the two most influential parameters.

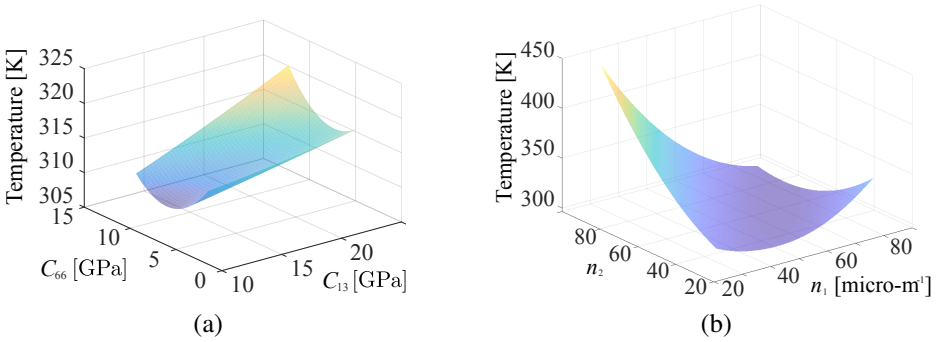

Figure 3.18: Variation of peak temperature over (a) C_{44}-C_{23} plane and (b) n_1-n_3 plane for polycrystal cases.

3.4.3.2 Plastic deformation mechanisms

Plastic deformation within the polycrystal microstructure includes the crystallographic slip within each crystal, and the interaction between the crystals. The initial dislocation density range is taken to be larger ([0.0307 micro-m^{-2}, 3.07 micro-m^{-2}]) in view of the high potential variability of this parameter as a function of processing conditions.

In the current case, we have employed a nonlocal definition of the primary response function (i.e., peak temperature) to ensure that numerical singularities introduced due to irregular element shapes or artificial viscosity do not pollute the sensitivity results. The response function is described as the distance-weighted average maximum temperature over a circular domain. As shown in Fig. 3.19, the peak nonlocal temperature at an arbitrary position $\hat{x}$ is computed as the weighted temperature over neighbor elements within the circular domain defined by the critical radius R_c. The nonlocal weight $w(x,\hat{x})$ of temperature at x with respect to the center $\hat{x}$ is expressed using the Wendland Radial Basis function:

$$w(x,\hat{x}) = \begin{cases} \left(1-\frac{||x-\hat{x}||}{R_c}\right)^4 \left(4\frac{||x-\hat{x}||}{R_c}+1\right), & ||x-\hat{x}|| <= R_c \\ 0, & ||x-\hat{x}|| > R_c \end{cases} \tag{3.15}$$

The time evolution of the peak nonlocal temperatures (i.e., the maximum nonlocal temperature over the entire domain of the specimen) obtained using different critical radii are

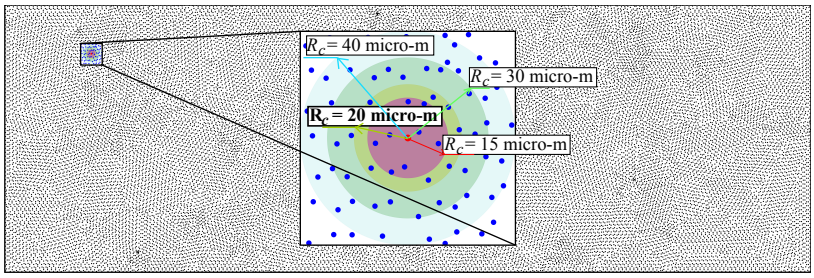

Figure 3.19: Computation of the nonlocal peak temperature. The dots represent integration points within the specimen discretization. The circles represent the searching areas with the critical radii. The central point (marked as red in the electronic version of the manuscript) is the position where the nonlocal average is computed.

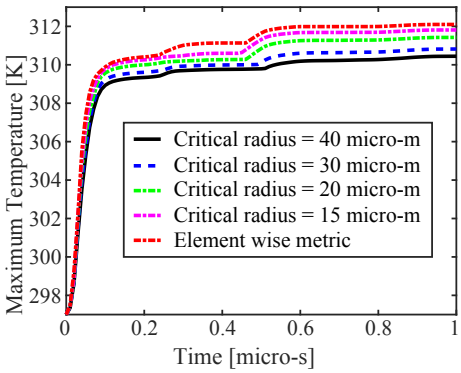

Figure 3.20: Maximum temperature-time curves with different critical radii.

shown in the Fig. 3.20. The results are generated using the model parameters stated in Section 4. The element size used in the discretization of the domain is approximately 10 micro-m. The general trend of the time evolution of the peak nonlocal temperature does not significantly change by the nonlocal radius, indicating that the numerical singularities do not appear to significantly affect the peak temperature even when local (i.e., element-wise) peak temperature is chosen as the response function. The magnitude of the temperatures naturally reduce with increasing nonlocal radius. The sensitivity analysis below employs a nonlocal radius of 20 micro-m.

The sensitivities were assessed based on 128 million predictions using the surrogate model trained with approximately 1280 FE simulations. The sensitivity indices and index convergence are shown in Fig. 3.21.

The results of the sensitivity indices are consistent with those from the single crystal

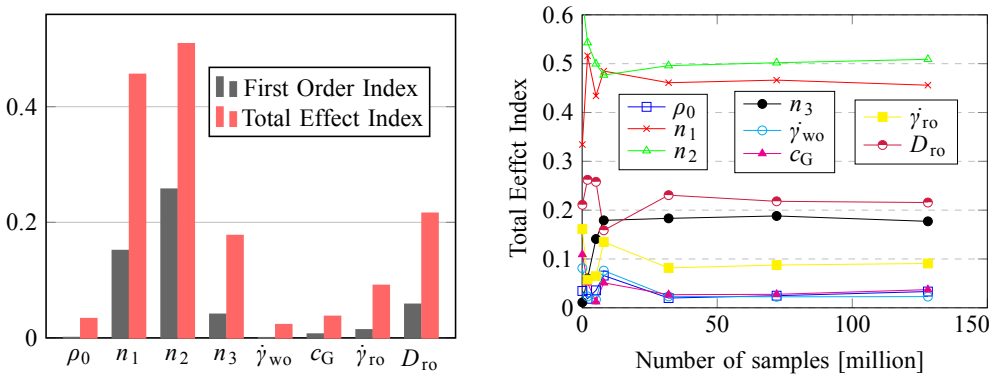

Figure 3.21: Summary of (a) sensitivity indices and (b) convergence for plastic parameters in polycrystal specimen.

analyses that the dislocation generation (n_1) and annihilation (n_2 or n_3) along with phonon drag mechanisms ($\dot{\gamma}_{ro}$ and D_{ro}) primarily describe the plastic deformation and dissipation processes that occur under the applied dynamic loading. The distribution functions computed based on the OAT approach (Fig. 3.22) also indicate that, while the overall contributions and variabilities differ from those computed based on the GSA, the effects of phonon drag and dislocation density evolution are dominant. The key dislocation density evolution parameters that describe the generation and annihilation terms interact in a nonlinear fashion to describe the overall dissipative response and consequent temperature rise in the microstructure, as shown in Fig. 3.18b. An interesting observation is that less dislocation generation (small n_1) and more dislocation annihilation (larger n_2 or n_3) lead to larger plastic deformation. This is due to the fact that the transition to phonon drag mechanism is significantly influenced by the ratio τ^α/g^α while smaller slip strength leads to earlier transition.

Both OAT and GSA in single crystal and polycrystal specimen indicate that the thermal activation mechanism has little contribution to the temperature at the current time scale and load amplitude, while the phonon drag mechanism, instead, has much larger slip rate and dominates the shear deformation.

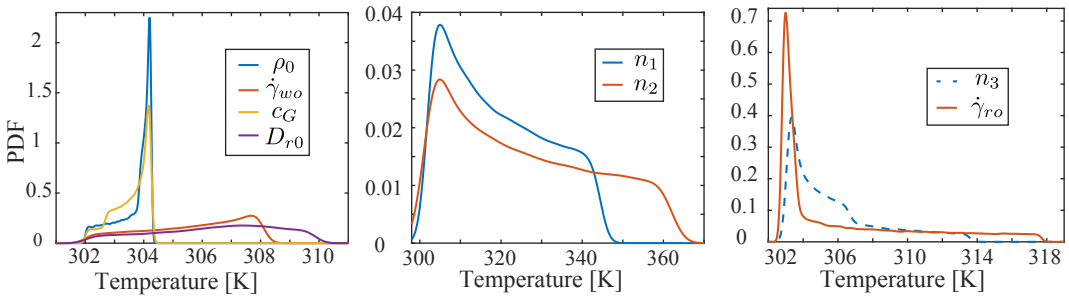

Figure 3.22: Probability distributions for peak temperature resulting from the OAT analysis of the individual plasticity parameters for polycrystal specimen.

3.5 Conclusion

This chapter presented the investigations of sensitivity of the response of crystalline β-HMX with respect to anisotropic elasticity constants and crystal plasticity properties under given impact loading through the proposed parameter sensitivity analysis framework. The results show that the anisotropic elasticity coefficients in the monoclinic crystalline have a modest effect on the energy dissipation and temperature rise dominated by sensitivities of a few coefficients. Among the two primary slip mechanisms, phonon drag appears dominant within the load rate amplitude regimes considered in this study. The dominating and non-dominating coefficients, slip mechanisms or dislocation evolution kinetics are identified through both OAT and GSA method, and the discrepancy between results are observed. The initial dislocation density appears to be not particularly influential. The quantified sensitivities of these mechanisms point to the main deformation mechanisms contributing to the complicated physical phenomena observed at microscale. The outcomes of the present analyses will be employed to suggest evolution laws that can capture the localized behavior by only including the physics contributing to the behavior of interest.

3.6 Appendix: Tensor of elastic moduli

The vector representations of the deviatoric stress and strain are expressed with five independent components as [101]:

$$\begin{aligned}
\text{dev}\boldsymbol{\tau} \rightarrow \{\tau'\} &= \{\frac{1}{\sqrt{2}}(\tau'_{11}-\tau'_{22}) \qquad \sqrt{\frac{2}{3}}\tau'_{33} \qquad \sqrt{2}\tau'_{12} \qquad \sqrt{2}\tau'_{13} \qquad \sqrt{2}\tau'_{23}\}^T \\
\text{dev}\boldsymbol{\epsilon}^e \rightarrow \{\varepsilon^{e\prime}\} &= \{\frac{1}{\sqrt{2}}(\varepsilon^{e\prime}_{11}-\varepsilon^{e\prime}_{22}) \qquad \sqrt{\frac{2}{3}}\varepsilon^{e\prime}_{33} \qquad \sqrt{2}\varepsilon^{e\prime}_{12} \qquad \sqrt{2}\varepsilon^{e\prime}_{13} \qquad \sqrt{2}\varepsilon^{e\prime}_{23}\}^T
\end{aligned} \tag{3.16}$$

The deviatoric and hydrostatic components of the constitutive law are written in the matrix notation as:

$$\begin{aligned}
\{\tau'\} &= [\widetilde{\mathbb{C}}^e_d]\{\varepsilon^{e\prime}\} + \{\widetilde{H}^e\}\text{tr}(\boldsymbol{\epsilon}^e) \\
p_\tau &= \{\widetilde{H}^e\}^T\{\varepsilon^{e\prime}\} + \widetilde{M}^e\text{tr}(\boldsymbol{\epsilon}^e)
\end{aligned} \tag{3.17}$$

where $[\cdot]$ indicates the matrix representation of a tensor. The contracted forms of the fourth order deviatoric elasticity tensor $\widetilde{\mathbb{C}}^e_d$, the deviatoric-isochoric elastic coupling tensor $\widetilde{\boldsymbol{H}}^e$ and the elastic volumetric coefficient $\widetilde{M}^e$ derived with respect to the crystal axis (indicated by the subscript 0) of the monoclinic lattice are:

$$[\mathbb{C}^e_d]_0 = \begin{bmatrix}
C^\star_{11} & C^\star_{12} & 0 & C^\star_{14} & 0 \\
C^\star_{12} & C^\star_{22} & 0 & C^\star_{24} & 0 \\
0 & 0 & C^\star_{33} & 0 & C^\star_{35} \\
C^\star_{14} & C^\star_{24} & 0 & C^\star_{44} & 0 \\
0 & 0 & C^\star_{35} & 0 & C^\star_{55}
\end{bmatrix} \tag{3.18}$$

where

$$
\begin{aligned}
C^{\star}_{11} &= \frac{C_{11}}{2} - C_{12} + \frac{C_{22}}{2} \\
C^{\star}_{12} &= -\frac{\sqrt{3}}{6}(C_{11} - 2C_{13} - C_{22} + 2C_{23}) \\
C^{\star}_{14} &= C_{15} - C_{25} \\
C^{\star}_{22} &= \frac{1}{6}(C_{11} + 2C_{12} - 4C_{13} + C_{22} - 4C_{23} + 4C_{33}) \\
C^{\star}_{24} &= -\frac{\sqrt{3}}{3}(C_{15} + C_{25} - 2C_{35}) \\
C^{\star}_{33} &= 2C_{44}, \quad C^{\star}_{35} = 2C_{46}, \quad C^{\star}_{44} = 2C_{55}, \quad C^{\star}_{55} = 2C_{66}
\end{aligned}
\tag{3.19}
$$

$$
\{H^e\}_0 = [H^{\star}_1 \quad H^{\star}_2 \quad 0 \quad H^{\star}_4 \quad 0] \tag{3.20}
$$

where

$$
\begin{aligned}
H^{\star}_1 &= \frac{\sqrt{2}}{6}(C_{11} + C_{13} - C_{22} - C_{23}) \\
H^{\star}_2 &= -\frac{\sqrt{6}}{18}(C_{11} - 3C_{23} - 3C_{33} - 3C_{13} + 2C_{12} + C_{22} + \frac{2|C_{13}|^2}{C_{13}} + \frac{2|C_{23}|^2}{C_{23}} + \frac{|C_{33}|^2}{C_{33}} \\
H^{\star}_4 &= \frac{\sqrt{2}}{3}(C_{15} + C_{25} + C_{35})
\end{aligned}
\tag{3.21}
$$

$$
M^e_0 = \frac{1}{9}(C_{11} + 2C_{12} + 2C_{13} + C_{22} + 2C_{23} + C_{33}) \tag{3.22}
$$

The tensor of elastic moduli in the intermediate configuration is obtained as:

$$
\widetilde{\mathbb{C}}^e_d = (\boldsymbol{C} \underline{\otimes} \boldsymbol{C}) : \mathbb{C}^e_{d0} : (\boldsymbol{C} \underline{\otimes} \boldsymbol{C})^T \tag{3.23}
$$

where $\boldsymbol{C} = \boldsymbol{R}^e \boldsymbol{C}_0$ represents the rotation from crystal coordinates to the global coordinates, and $(\boldsymbol{C} \underline{\otimes} \boldsymbol{C})_{ijAB} = C_{iA} C_{jB}$. The initial orientation $\boldsymbol{C}_0$ is prescribed as part of the crystal initial state in terms of the Euler angles in Kocks convention.

Chapter 4

MODELING AND NUMERICAL INVESTIGATION OF MECHANICAL TWINNING IN β-HMX CRYSTALS SUBJECTED TO SHOCK LOADING

4.1 Introduction

In this chapter, mechanical twinning in β-HMX subjected to shock loading is modeled in the microcale through the CPFE formulation with the capability of modeling large volume deformation at shock regime. Mechanical twinning has been identified as the dominant mechanism in quasi-static experiments, however, numerical modeling of twinning in β-HMX is still an undeveloped region. Zamiri and De [193] incorporated the twinning system into the formulation by taking it as a slip system using the same flow and hardening evolution law as for slip, which does not distinguish the fundamental difference between dislocation and twinning. Hence, the twinning model of β-HMX is developed based on a CPFE formulation which is capable of incorporating multiple deformation mechanisms (anisotropic elasticity, dislocation slip, twinning and large volumetric change) and predict the dynamic behaviors of β-HMX in shock regime.

In this chapter, we model and simulate the dynamic behavior of β-HMX crystals with emphasis on twinning phenomenon under different loading rates. Twin model of the monoclinic crystal is developed in a large deformation CPFE framework proposed by Becker [14] to capture dynamic responses up to shock loading regime. In this large deformation formulation, the third order Birch Murnaghan (BM) Equation-Of-State (EOS) [18] is employed to describe the pressure-volume relationship, and the Gruneisen tensor is incorporated to characterize the coupling between pressure and distortion for this monoclinic crystal. To capture the orientation dependent deformation ([37, 112, 192]) in β-HMX under dynamic loads, the elastic model of HMX not only incorporates the EOS, but also integrates the pressure dependency in the thirteen elasticity coefficients of the monoclinic crystal. Dis-

location slip within β-HMX twinned/untwinned crystals subjected to dynamic loads are depicted by the evolution law proposed by Zhang and Oskay [199] in which both thermal activation and phonon drag mechanisms are considered such that both slow dislocation motion (1e-6 m/s - 1 m/s) and faster dislocation motion ($>$1 m/s) can be captured. The proposed CPFE model is employed to investigate twin accumulation in single and polycrystal HMX configurations. The study of twin concentration within HMX polycrystalline specimens is focused on the effect of particle geometry and crystal misorientation. The key novel contribution of this chapter is the incorporation of mechanical twinning in HMX crystal as an independent physical phenomenon, and analysis of twinning evolution under a given dynamic loading regime for both single crystal and polycrystalline configurations.

The remainder of this chapter is structured as follows: Section 2 provides the crystal plasticity constitutive relations employed in the simulation of the dynamic response of β-HMX at the microscale, as well as the detailed twinning evolution equations. Section 3 describes the parameter calibration, including the parameters of thermo elastic deformation, dislocation slip and mechanical twinning. Numerical investigations that utilize the aforementioned CPFE framework and embedded twinning model to predict twin concentrations in both single crystal and polycrystalline configurations are discussed in Section 4. Section 5 provides the summary and conclusions.

4.2 Constitutive Model of β-HMX

The anisotropic deformation behavior of HMX at the crystal scale is modeled using the Crystal Plasticity Finite Element (CPFE) model accounting for the large volume change under shock loading, dislocation slip and mechanical twinning. The model formulation is based on multiplicative decomposition of the deformation gradient and the assumption that deviatoric thermo-elastic stretch remains small relative to volumetric deformation. The

deformation gradient $\boldsymbol{F}$ is decomposed as

$$\boldsymbol{F} = \boldsymbol{V}^e \cdot \boldsymbol{R}^e \cdot \boldsymbol{F}^p \tag{4.1}$$

where $\boldsymbol{V}^e$ is the left stretch tensor representing the elastic stretch of the lattice, $\boldsymbol{R}^e$ is the orthogonal tensor defining the rotation and reorientation of the material point in a grain, and $\boldsymbol{F}^p$ represents the plastic deformation induced by dislocation slip and twinning evolution in the crystallographic slip/twin systems. While we introduce two intermediate configurations, deformed but unrotated configuration, and the configuration obtained by unloading the elastic stretch from the current configuration, plasticity update is performed in the former configuration. All quantities with overbar in this formulation indicate representation in the plastically deformed but unrotated intermediate configuration. To characterize the elastic deformation, a logarithmic form is used for the lattice strain measure expressed in the intermediate configuration defined by $\boldsymbol{R}^e$.

$$\overline{\boldsymbol{E}} = \ln(\overline{\boldsymbol{V}}^e) \quad \text{where} \quad \overline{\boldsymbol{V}}^e = \boldsymbol{R}^{eT} \cdot \boldsymbol{V}^e \cdot \boldsymbol{R}^e \tag{4.2}$$

It is important to note that the hydrostatic elastic strain induced by shock compression remains large despite the small deviatoric elastic strain assumption. Let $a = (\det(\boldsymbol{V}^e))^{\frac{1}{3}}$ such that $\boldsymbol{V}^e = a\boldsymbol{V}^{e\star}$ and $\det(\boldsymbol{V}^{e\star}) = 1$. Then we assume $\boldsymbol{V}^{e\star} = \boldsymbol{I} + \boldsymbol{\epsilon}^\star$, which results in

$$\boldsymbol{V}^e = a(\boldsymbol{I} + \boldsymbol{\epsilon}^\star) \tag{4.3}$$

where, $\boldsymbol{I}$ is the second order unit tensor, $\boldsymbol{\epsilon}^\star$ denotes the small elastic deviatoric strain tensor ($\boldsymbol{\epsilon}^\star << \boldsymbol{I}$) and $\boldsymbol{\epsilon}^\star = \boldsymbol{\epsilon}^{\star\prime} = \frac{1}{a}\boldsymbol{V}^{e\prime}$. The volumetric and deviatoric parts of $\overline{\boldsymbol{E}}$ are expressed respectively as:

$$\overline{E}_V = \overline{\boldsymbol{E}} : \boldsymbol{I} = \ln(a^3) \quad \text{and} \quad \overline{\boldsymbol{E}}' \approx \frac{1}{a}\overline{\boldsymbol{V}}^{e\prime} \tag{4.4}$$

After some algebra detailed in [9], the following simplified kinematics equations for

small deviatoric elastic strain are obtained. The deformation rate $\boldsymbol{D}$ is described in terms of its deviatoric and volumetric components.

$$\boldsymbol{R}^{eT}\cdot\boldsymbol{D}'\cdot\boldsymbol{R}^{e}=\frac{1}{a}\dot{\overline{\boldsymbol{V}}}^{e\prime}+\overline{\boldsymbol{D}}' \tag{4.5a}$$

$$\frac{d}{dt}\big(\det(\boldsymbol{V}^{e})\big)=\det(\boldsymbol{V}^{e})\mathrm{tr}(\boldsymbol{D}-\overline{\boldsymbol{D}}) \tag{4.5b}$$

The spin tensor $\boldsymbol{W}$ is expressed as:

$$\boldsymbol{R}^{eT}\cdot\boldsymbol{W}\cdot\boldsymbol{R}^{e}=\boldsymbol{R}^{e}\cdot\boldsymbol{W}^{R}\cdot\boldsymbol{R}^{eT}+\overline{\boldsymbol{W}}+\frac{1}{a}[\overline{\boldsymbol{V}}^{e\prime}\cdot(\overline{\boldsymbol{D}}'+\frac{1}{2a}\dot{\overline{\boldsymbol{V}}}^{e\prime})-(\overline{\boldsymbol{D}}'+\frac{1}{2a}\dot{\overline{\boldsymbol{V}}}^{e\prime})\cdot\overline{\boldsymbol{V}}^{e\prime}] \tag{4.6}$$

where $\boldsymbol{W}^{R}=\dot{\boldsymbol{R}}^{e}\cdot\boldsymbol{R}^{eT}$, $\overline{\boldsymbol{W}}$ is the spin tensor in the intermediate configuration, $\boldsymbol{D}'$ is the deviatoric component of deformation rate, and $\overline{\boldsymbol{D}}'$ is the deviatoric component of $\overline{\boldsymbol{D}}$, which is the deformation rate in the intermediate configuration.

4.2.1 Anisotropic elasticity

At large pressures encountered in high rate conditions, the crystals undergo large volumetric deformations, and the elastic moduli are pressure dependent. The pressure-volume relationship is described by the equation of state, and the coupling of pressure and distortion is captured through the Gruneisen parameter.

For simplicity, we employ the Kirchhoff stress $\overline{\boldsymbol{\tau}}=J\overline{\boldsymbol{\sigma}}$ as the approximation of the conjugate stress to the logarithmic strain $\overline{\boldsymbol{E}}$ [56, 63], where $J=a^{3}$ is the Jacobian of the deformation gradient, and $\overline{\boldsymbol{\sigma}}=\boldsymbol{R}^{eT}\cdot\boldsymbol{\sigma}\cdot\boldsymbol{R}^{e}$. The elastic model [14] is expressed as $\overline{\boldsymbol{\tau}}=J\overline{\boldsymbol{\sigma}}=J\big[\overline{\mathbb{C}}^{e}:\overline{\boldsymbol{E}}+\frac{1}{2}(\overline{\boldsymbol{E}}:\frac{d\overline{\mathbb{C}}^{e}}{dp_{\overline{\tau}}}:\overline{\boldsymbol{E}})\frac{dp_{\overline{\tau}}}{d\overline{E}_{V}}\boldsymbol{I}\big]$, where $\overline{\mathbb{C}}^{e}$ is the pressure dependent elastic moduli tensor in the intermediate frame, and $p_{\overline{\tau}}$ is pressure. The Kirchhoff stress is decomposed to the deviatoric and volumetric parts with the introduction of the Gruneisen tensor and the EOS [14]:

$$\overline{\boldsymbol{\tau}}'=J\overline{\boldsymbol{\sigma}}'=J\Big[\mathbb{P}_{d}:\overline{\mathbb{C}}^{e}:\overline{\boldsymbol{E}}'+\frac{1}{3}(\mathbb{P}_{d}:\overline{\mathbb{C}}^{e}:\boldsymbol{I})\overline{E}_{V}+\boldsymbol{\Gamma}'e\Big] \tag{4.7}$$

$$
\begin{aligned}
p_{\overline{\tau}} &= -J\overline{\sigma}_h \\
&= -J\Big\{\sigma_h|_{\text{EOS}} + \frac{1}{3}(\overline{\boldsymbol{E}}' : \overline{\mathbb{C}}^e : \boldsymbol{I}) + \Big[\frac{1}{2}(\overline{\boldsymbol{E}}' : \frac{d\overline{\mathbb{C}}^e}{dp_{\overline{\tau}}} : \overline{\boldsymbol{E}}') + \frac{1}{3}(\overline{\boldsymbol{E}}' : \frac{d\overline{\mathbb{C}}^e}{dp_{\overline{\tau}}} : \boldsymbol{I})\overline{E}_V\Big]\frac{dp_{\overline{\tau}}}{d\overline{E}_V} - \Gamma e\Big\}
\end{aligned}
\tag{4.8}
$$

where $\mathbb{P}_d$ represents a fourth order operator that extracts the deviatoric part of a second order tensor, i.e., $\mathbb{P}_d = \mathbb{I} - \frac{1}{3}\boldsymbol{I}\otimes\boldsymbol{I}$ with fourth order identity tensor, $\mathbb{I}$. e is the volumetric part of the internal energy density. $\boldsymbol{\Gamma}'$ is the deviatoric part of the Gruneisen tensor expressed as a function of the thermal expansion tensor for the anisotropic material [81]. Γ is the volumetric component of the Gruneisen tensor. The matrix form of the Gruneisen tensor [81] is given as:

$$
\begin{bmatrix} \Gamma_{11} \\ \Gamma_{22} \\ \Gamma_{33} \\ \Gamma_{23} \\ \Gamma_{13} \\ \Gamma_{12} \end{bmatrix} = \frac{1}{\rho C_V} \begin{bmatrix} C_{11} & C_{12} & C_{13} & 0 & C_{15} & 0 \\ C_{12} & C_{22} & C_{23} & 0 & C_{25} & 0 \\ C_{13} & C_{23} & C_{33} & 0 & C_{35} & 0 \\ 0 & 0 & 0 & C_{44} & 0 & C_{46} \\ C_{15} & C_{25} & C_{35} & 0 & C_{55} & 0 \\ 0 & 0 & 0 & C_{46} & 0 & C_{66} \end{bmatrix} \begin{bmatrix} \alpha_{11} \\ \alpha_{22} \\ \alpha_{33} \\ \alpha_{23} \\ \alpha_{13} \\ \alpha_{12} \end{bmatrix}
\tag{4.9}
$$

where ρ is the mass density, C_V the specific heat, and α_{ij} is a component of thermal expansion tensor, $\boldsymbol{\alpha}$. Values of the thermal expansion tensor components for monoclinic β-HMX crystal were measured and provided in [36].

The part of Eq. 4.8 that deals with the pressure-volume relationship is replaced by an equation of state, $\sigma_h|_{\text{EOSs}}$. Various EOS have been proposed in modeling the hydrodynamic behavior of β-HMX subjected to levels of pressure induced by explosion or impact. Olinger et al. [121] measured room temperature isotherm for β-HMX and fit the isotherm to an EOS with two fitting parameters. Yoo and Cynn [189] obtained the pressure-volume relationship of β-HMX by fitting the isotherms of unreacted HMX (with pressure up to 27 GPa and 12 GPa, respectively) to the third-order Birch Murnaghan (BM) EOS for both hydrostatic and non-hydrostatic conditions. Menikoff and Sewell [111] re-analyzed the experiments from Olinger et al. [121] and Yoo and Cynn [189] to determine which fitting

form is most consistent with other data for HMX and HMX-based plastic-bonded explosives. In order to investigate the sensitivity of bulk modulus of β-HMX to the choice of EOS and weight scheme, Sewell et al. [153] applied three forms of EOS [111, 121, 189] to isotherms for β-HMX obtained from their simulations and two additional simulations from [161], and they concluded that the third-order BM EOS, fit with a weighting scheme that emphasizes low-pressure data, and consistently yields initial moduli in closest agreement with values obtained from theoretical predictions. Gump and Peiris [55] obtained the pressure-volume third-order BM EOS of β-HMX at temperatures of 30 °C, 100 °C, and 140 °C under both hydrostatic and non-hydrostatic compressions up to 5.8 GPa and 4 GPa, and observed phase transition from β to δ beyond these pressures. In contrast, Hooks et al. [65] did not observe phase transition in the isentropic compression reverberation experiments performed on (010) and (011) oriented HMX crystals up to a peak stress of about 54 GPa.

Despite the controversy on the pressures to phase transition, References [28, 88, 127] employed data from both [189] and [55] to fit third-order BM EOS for β-HMX with pressure up to 12 GPa.

Under larger pressure, additional physico-chemical mechanisms such as chemical reactions and crystal melting are involved in the deformation process. Austin et al. [7] described the thermo-elasto-viscoplastic behavior of the β phase HMX by incorporating a Murnaghan EOS into the crystal plasticity model, in which decomposition reaction and crystal melting are considered to reproduce Hugoniot data [102] with pressure larger than 40 GPa. Recently, White and Tarver [183] developed the parameters of Jones-Wilkins-Lee (JWL) EOS for HMX single crystal with mass density 1.905 g/cm^3 and of JWL EOS for reaction products.

Following Refs [28, 88, 127], third order BM EOS is employed in this study:

$$\sigma_h|_{\text{EOS}} = -\frac{3B_0}{2}\left(J^{-\frac{7}{3}} - J^{-\frac{5}{3}}\right)\left[1 + \frac{3}{4}(B_0' - 4)\left(J^{-\frac{2}{3}} - 1\right)\right] \tag{4.10}$$

where B_0 is the bulk modulus at zero pressure, and B_0' is the derivative of the bulk modulus with respect to pressure at zero pressure. The volumetric part of the internal energy density e is then expressed as

$$e = \frac{9B_0}{16}J^{-1}\left[\left(J^{-\frac{2}{3}}-1\right)^3 B_0' + \left(J^{-\frac{2}{3}}-1\right)^2\left(6-4J^{-\frac{2}{3}}\right)\right] \tag{4.11}$$

4.2.2 Mechanical twinning model

The velocity gradient in the plastically deformed but unrotated intermediate configuration, $\overline{\boldsymbol{L}}$, is decomposed into three components [77]:

$$\overline{\boldsymbol{L}} = \dot{\boldsymbol{F}}^p \cdot (\boldsymbol{F}^p)^{-1} = (1-\sum_{\beta=1}^{N^{\text{tw}}} f^\beta)\sum_{\alpha=1}^{N^{\text{sl}}} \dot{\gamma}^\alpha \overline{\boldsymbol{Z}}^\alpha_{\text{sl}} + \sum_{\beta=1}^{N^{\text{tw}}} \dot{f}^\beta \gamma^\beta_{\text{tw}} \overline{\boldsymbol{Z}}^\beta_{\text{tw}} + \sum_{\beta=1}^{N^{\text{tw}}} f^\beta (\sum_{\alpha=1}^{N^{\text{sl-tw}}} \dot{\gamma}^\alpha \overline{\boldsymbol{Z}}^\alpha_{\text{sl-tw}}) \tag{4.12}$$

where $\dot{\gamma}^\alpha$ denotes the resolved shear strain rate on a slip system α, f^β the volume fraction of the twinned region on the twinning system β, γ^β_{tw} the (constant) twinning shear strain, and $\overline{\boldsymbol{Z}}^\beta$ is the corresponding Schmid tensor that project the strain rate contribution from the corresponding slip or twin system. The first term is the contributions of dislocation slip along N^{sl} slip systems in the untwinned region. The second term models the contribution of twinning on N^{tw} twin systems. The last term reflects the contribution from slip in the twinned regions, and $\overline{\boldsymbol{Z}}^\alpha_{\text{sl-tw}}$ is obtained through rotation of the corresponding slip system:

$$\overline{\boldsymbol{Z}}^\alpha_{\text{sl-tw}} = Q^\beta \overline{\boldsymbol{Z}}^\alpha_{\text{sl}} {Q^\beta}^T \tag{4.13}$$

where Q^β is the rotation matrix between twinned and non-twinned lattices. Considering the fact that the deformation twins are thin structures, slip in the twinned regions are expected to be restricted to the co-planar slip systems with respect to the twin plane ($N_{\text{tw}} < N_{\text{sl-tw}}$).

Various models have been developed to describe twinning in crystals [141]. Kalidindi [77] implemented a CPFE framework, where the crystal orientation in a relaxed config-

uration for both the twinned and untwinned regions are pre-defined based on the initial lattice orientation. Wang et al. [179] proposed a physics-based crystal plasticity model to deal with both twinning and de-twinning mechanisms by incorporating twin nucleation, growth, shrinkage and re-twinning during the deformation process. However, many of the governing physical mechanisms for strain-induced twinning still remain unresolved [141]. Information on the evolution of the twinned volume fraction in β-HMX, especially under high rate loading is scarce. Hence, a phenomenological approach is employed in this study to describe the evolution of twin volume fraction in β-HMX [78, 179].

The evolution of twin volume fraction is taken to be affected by the resolved shear stress on the twinning systems, and the twinning resistance idealizes the resistance from neighbor molecules as well as the potential interaction between twinning and dislocation slip. Mechanical twinning is taken to occur only in the positive twinning direction and no recovery of twinning (i.e., detwinning [133]) is considered. Hence, the evolution of the volume fraction of twinning depends only on the resolved shear stress and twinning resistance through a power law function [78, 179]:

$$\dot{f}^{\beta} = \frac{\dot{\gamma}_{\mathrm{tw}}^{\mathrm{ref}}}{\gamma_{\mathrm{tw}}^{\beta}} \left(\frac{\tau^{\beta}}{g_{\mathrm{tw}}^{\beta}} \right)^{1/m_{\mathrm{tw}}^{\beta}} \quad \text{for} \quad \tau^{\beta} > 0 \tag{4.14}$$

where $\dot{\gamma}_{\mathrm{tw}}^{\mathrm{ref}}$ is the reference twin rate, $\gamma_{\mathrm{tw}}^{\beta}$ is the (constant) twinning shear strain, g_{tw}^{β} is the twin resistance and m_{tw}^{β} is a rate-sensitivity parameter. The twin volume fraction induced by the permanent twin cannot be negative, and the twinned regions are not allowed to untwin, i.e., $\dot{f}^{\beta} = 0$ for $\tau^{\beta} \leq 0$. Naturally, f^{β} is always non-negative, and an upper bound in the crystals exist: $f^{\beta} \geq 0$ and $\sum_{\beta}^{N^{\mathrm{tw}}} f^{\beta} \leq 1.0$. This phenomenological evolution law does not separate nucleation and growth of twinning, but rather tracks the volume fraction change of twinning in an average sense. The power-law parameter m_{tw}^{β} represents the strain rate sensitivity of twin growth.

4.2.3 Dislocation slip evolution

The first and third terms in Eq. 4.12 respectively define the contributions of the active slip systems and slip systems in the twinned region on the shear deformation in the crystal. A number of slip evolution models have been previously proposed for HMX [7, 10, 53, 60, 182]. At low shear stress magnitudes, the driving force on the dislocation is low and the dislocations move in a thermally activated manner. At high shear stress magnitudes, the movement of dislocations are limited by phonon drag.

In the current chapter, dislocation slip at slow (1e-6 m/s - 1 m/s) and faster speeds (> 1 m/s) are considered and modeled with both thermal activation and phonon drag mechanisms [199]. The thermally activated slip is expressed as:

$$\dot{\gamma}^{\alpha}_{w} = \begin{cases} \frac{\dot{\gamma}^{\alpha}_{wo}}{\sqrt{\rho_{\text{norm}}}}\Big[\exp\big(-\frac{\Delta G^{\alpha}(\tau^{\alpha})}{\kappa\theta}\big) - \exp\big(-\frac{\Delta G^{\alpha}(-\tau^{\alpha})}{\kappa\theta}\big)\Big] + h(\tau^{\alpha}), & \text{if} \quad |\tau^{\alpha}| \leq g^{\alpha} \\ \frac{\dot{\gamma}^{\alpha}_{wo}}{\sqrt{\rho_{\text{norm}}}}\text{sign}(\tau^{\alpha})\Big[1 - \exp\big(-\frac{2c_G\mu^{\alpha}}{\kappa\theta}\big)\Big] + h(\tau^{\alpha}), & \text{if} \quad |\tau^{\alpha}| > g^{\alpha} \end{cases} \tag{4.15}$$

where $\dot{\gamma}^{\alpha}_{wo}$ is the reference shear strain rate, κ is the Boltzmann constant and θ the temperature. The transition from thermal activation to phonon drag is controlled by the penalty function: $h(\tau^{\alpha}) = \text{sign}(\tau^{\alpha})(\frac{\tau^{\alpha}}{g^{\alpha}})^{\zeta}$ where ζ is a parameter. ρ_{norm} is a dimensionless dislocation density measure normalized by the reference dislocation density ρ_{ref} ($\rho_{\text{norm}} = \rho/\rho_{\text{ref}}$). $\Delta G^{\alpha}(\tau^{\alpha})$ is given by:

$$\Delta G^{\alpha}(\tau^{\alpha}) = c_G\mu^{\alpha}\Big[1 - \Big(\frac{\tau^{\alpha}}{g^{\alpha}}\Big)^{p}\Big]^{q} \tag{4.16}$$

where c_G, p, q are constants, and μ^{α} is the shear modulus resolved in the α^{th} slip system [46]. g^{α} is the slip strength of the slip system α, and takes the form:

$$g^{\alpha} = r^{\alpha}(g_o + s\sqrt{\rho}) \tag{4.17}$$

where, s and g_o are model parameters, and r^{α} is the ratio of the slip system strength g^{α} and

the reference slip system strength, $g^{(010)[100]}$ ($r^{(010)[100]} = 1$).

The drag term operates as the dislocation bows between obstacles before it cuts or bypasses them. For the glide of dislocations between sets of obstacles, the slip rate is:

$$\dot{\gamma}_r^{\alpha} = \text{sign}(\tau^{\alpha})\dot{\gamma}_{ro}\rho_{\text{norm}}\Big[1 - \exp(-\frac{|\tau^{\alpha}|}{D_r})\Big]; \quad D_r = D_{ro}\frac{\theta}{\theta_0} \tag{4.18}$$

where $\dot{\gamma}_{ro}$ is the reference shear strain rate, D_{ro} is the reference drag stress, and θ_0 is the reference temperature. The evolution of slip strength is controlled by the dislocation density which, under dynamic loading, evolves through generation and annihilation mechanisms:

$$\frac{d\rho}{d\gamma} = n_1\sqrt{\rho} - n_2\dot{\gamma}^{-\frac{1}{n_3}}\rho \tag{4.19}$$

n_1, n_2 and n_3 are constants.

Molecular packing of β-HMX [122] induces slip asymmetries in all slip planes. The slip asymmetry was also observed in other energetic molecular crystals, such as RDX [103]. While modeling of asymmetry is straightforward from the implementation viewpoint, values for asymmetric critical resolved shear stress (CRSS) and mobility are not currently available. Slip asymmetry effects are therefore not included in the present model.

4.3 Parameter Calibration

In this section, data from previous experimental studies, molecular dynamics (MD) and CPFE simulations are employed to calibrate the parameters of the proposed model for β-HMX. Calibration of the parameters for the anisotropic elasticity model and EOS, dislocation slip evolution, and twinning evolution are discussed separately.

4.3.1 Elasticity

The elastic model is fully described by the elasticity coefficients, mass density, specific heat, EOS parameters and the Gruneisen tensor. Thirteen coefficients of the anisotropic

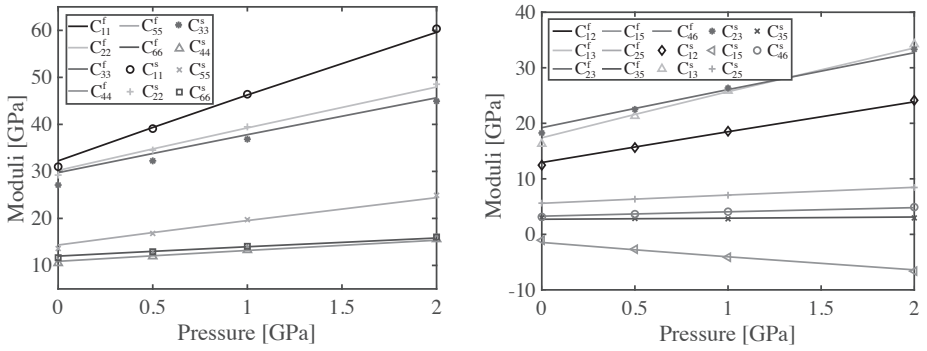

(a) (b)

Figure 4.1: Elasticity coefficients with pressure dependency for (a) the diagonal terms; and (b) the off-diagonal terms.

Table 4.1: Parameters of the elasticity model.

Parameter	B_0	B_0'	c_V	ρ_0^{mass}	α_{11}
Unit	GPa		kJ/(kg · K)	g/cm^3	10^{-6}/K
Value	16.71	7.79	1	1.9	-2.9
Parameter	α_{22}	α_{33}	α_{23}	α_{13}	α_{12}
Unit	10^{-6}/K	10^{-6}/K	10^{-6}/K	10^{-6}/K	10^{-6}/K
Value	116	17.9	0	-12.6	0

tensor of the monoclinic lattice are pressure dependent. Mathew and Sewell [104] computed the elasticity tensor components using MD simulations for pressures up to 2 GPa, as shown in Fig. 4.1. These values are used in the model calibration.

The EOS and the Gruneisen tensor account for the large volumetric deformation and potential distortion induced by thermal expansion. Bulk modulus, B_0, and the derivative of the bulk modulus with respect to pressure, B_0', are taken to be 16.71 GPa and 7.79 following [88]. The Gruneisen tensor for the anisotropic material is expressed as a function of mass density, specific heat and thermal expansion coefficients. Initial mass density of β-HMX, ρ_0^{mass}, is 1.9 g/cm^3, and the specific heat c_V is set to 1 kJ/(kg·K). Thermal expansion coefficients are obtained from the measurements of Ref. [61] and summarized in Table 4.1.

4.3.2 Dislocation slip parameters

Previous experiments and first principles calculations suggest that slip in HMX molecular crystal can occur along a large number of slip systems induced by the irregular molecular shape. Potential slip systems in β-HMX have been identified by Gallagher et al. [45] as $(001)[100]$, $(101)[10\bar{1}]$ and $(101)[010]$. Barton et al. [10] employed ten slip systems determined based on MD simulations. In that work, the corresponding slip strengths were selected according to an optimization algorithm to minimize the difference between simulation predictions and experimental observations. Recently, Pal and Picu [122] used MD simulations to identify slip systems which are potentially active in β-HMX, and ranked them in terms of their propensity for slip. Khan et al. [82] extended their study to finite temperatures, and evaluated critical thresholds for activating steady-state dislocation motion in the two most probable slip planes, (101) and (011). To model the nature of plasticity in HMX, full list of active slip systems and accurate description of slip behaviors within each slip system are needed from either smaller scale information or through parameter calibration at the continuum scale.

We initially attempted to calibrate parameters for all potential slip systems (27 systems) proposed in the literature [10, 82, 103, 122, 123]. However, incorporating more slip systems than those used in Barton's model complicates the calibration procedure, and no substantial improvement in matching particle velocity profiles is observed. Therefore, instead of modeling full list of potential slip systems, ten slip systems proposed by Barton et al. [10] are employed in the current chapter and summarized in Table 4.2 with calibrated parameters through particle velocity profiles. All slip systems are given in $P2_1/n$ notation. The lattice structure of β-HMX is described by four cell parameters: a, b, c and β (a=6.5374 Å, b=11.0296 Å, c=7.3549 Å, and β=102.69° [25]). Slip system strength ratios r^{α} and phonon drag parameter D_{ro} as well as the thermal activation and dislocation density evolution parameters are set to those provided in Ref. [199].

Table 4.2: Slip strength ratios.

Slip system	$(010)[100]$	$(011)[100]$	$(01\bar{1})[\bar{1}00]$	$(101)[0\bar{1}0]$	$(001)[100]$
Ratio r^{α}	1	0.963	0.963	0.933	1.68
Slip system	$(101)[10\bar{1}]$	$(011)[\bar{1}1\bar{1}]$	$(0\bar{1}1)[111]$	$(1\bar{1}0)[001]$	$(\bar{1}\bar{1}0)[00\bar{1}]$
Ratio r^{α}	0.376	0.931	0.931	0.701	0.701

4.3.3 Twinning parameters

The primary twinning system in HMX crystal has been identified as $(101)[10\bar{1}]$ in $P2_1/n$ space group [4, 21, 45, 124] ($N^{\text{tw}} = 1$). Within the twinning system $(101)[10\bar{1}]$, characteristic twinning shear strain γ_{tw}, reference twin rate $\dot{\gamma}_{\text{tw}}^{\text{ref}}$, twinning resistance g_{tw} and the power-law parameter m_{tw} fully define the twinning evolution law. The fact that deformation twins are thin structures constrains further slip and twinning in the twinned region.

Among those four parameters, γ_{tw} has been calculated by Gallagher et al. [45] as 0.353. While research has been done to quantify twinning resistance, g_{tw}, for other materials [113], there is no experimental measurement of this parameter for HMX. Zamiri and De [192] employed a slip-like twinning model with the initial value of twinning resistance 2.5 MPa at 24 °C and 2.2 MPa at 55 °C. and the saturation values of twin resistance are also reported as 2.55 MPa at 24 °C (297 K) and 3.1 MPa at 55 °C (328 K). The study by Zamiri and De [192] used identical values for twinning and slip resistance. A commonly used method to calibrate the critical stress is through fitting the macroscopic stress-strain curve [73, 74, 99, 113, 132, 169]. However, this approach is not applicable for β-HMX due to the lack of experimental stress-strain curve at the relevant strain rate. The rate-sensitivity parameter m_{tw} is set to a small number (0.05) to approach the rate-insensitivity for twinning [73, 77, 132].

Two of the twinning parameters (reference twin rate $\dot{\gamma}_{\text{tw}}^{\text{ref}}$ and twinning resistance g_{tw}) are calibrated using the plane shock experiments by Dick et al. [37]. In these experiments, an initial velocity is applied to an impactor. The shock wave generated by the impactor is

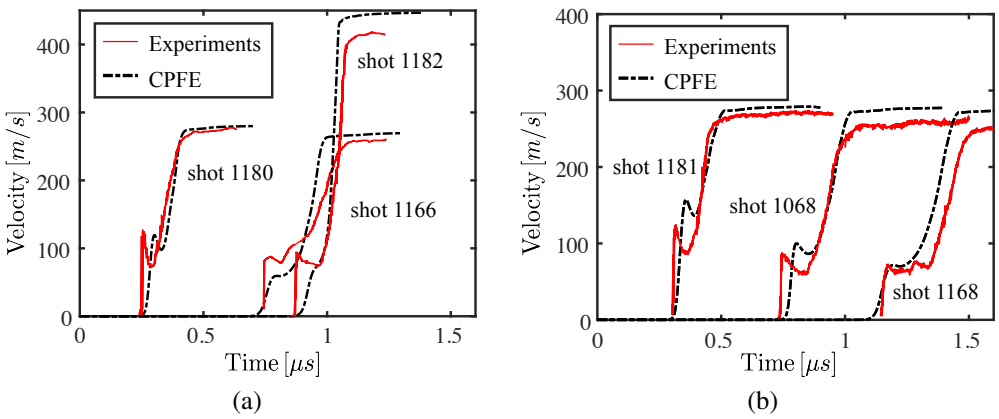

Figure 4.2: Model verification with respect to loading in (a) the $(110)_{P2_1/n}$ direction; and (b) the $(011)_{P2_1/n}$ direction.

transmitted through the specimen, which is a single HMX crystal. The calibration is performed by minimizing the discrepancy between experimentally observed and numerically simulated particle velocity profiles at the interface between the specimen and the PMMA window behind the specimen.

In the numerical simulations, the specimen is discretized using a quasi-one-dimensional mesh, and the loading is applied as prescribed constant velocity. The amplitude of the applied velocity is determined using the measured impactor velocity through the impedance matching technique, in which linear Hugoniot relationships are employed for the impactor, anvils and HMX [16, 112]. The PMMA window is bonded to the HMX specimen, and modeled using the nonlinear viscoelastic constitutive law developed by Schuler and Nunziato [150]. Periodic boundary conditions are applied at the top/bottom and front/back boundaries. Dislocation density field is taken to be uniform prior to the onset of the dynamic load. The particle velocity at HMX/PMMA interface is extracted for parameter calibration. In a similar study, Barton et al. [10] observed a discrepancy between the times of arrival in the predictions and experiments due to the dependence of elastic parameters to pressure and temperature and reported the prediction results with a time shift. In the current simulations, time shift is not used.

Calibration data are collected from three shots along $(110)_{P2_1/n}$ direction and three

Table 4.3: Twinning parameters.

Variable	$\dot{\gamma}_{tw0}$	γ_{tw}	m_{tw}	g_{tw}
Unit	μs^{-1}			MPa
Number	1	0.353	0.05	120

shots with single crystals along $(011)_{P2_1/n}$ direction as shown in Table 3.3. In the calibration process, strong crystal orientation dependency of the twin model is observed. Prevalent twin accumulation occurs at shots under loading in (011) direction, while only a small amount of twin is observed in (110) direction. The predictions of the calibrated model and experimental measurements are compared in Fig. 4.2. Overall, a reasonable agreement between the predictions and experimental data is observed. Calibrated twinning parameters are summarized in Table 4.3. Although the prediction of overall wave propagation is qualitatively similar to the prediction with a previous model that considered only slip evolution on the twin plane [199], the presence of twins does contribute to the plastic response, which is explained in Fig. 4.3. The particle velocity profile of shot 1168 is simulated with two models, and the fittings are shown in Fig. 4.3. In the first model, only dislocation slip is incorporated in the current large deformation CPFE model, while in the second model, both dislocation slip and twins are considered. All slip parameters are identical in the two models. The presence of twins significantly reduces the elastic peak at t=0.15 μs, and increases the following stress decay. The plastic peaks in both models are the same. Furthermore, velocity of the plastic wave is slower in the model with twinning than the prediction without twins, which results in a better fitting between the numerical simulation and the experiment. The presence of twins introduces more plastic deformation into the system, which increases the accuracy of model prediction in terms of both elastic peak and plastic wave propagation.

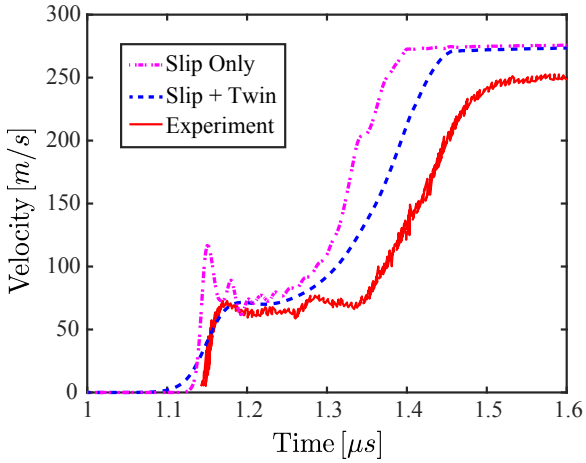

Figure 4.3: Effect of twinning on model prediction. Particle velocity of shot 1168 is predicted using current model with twinning (dislocation slip and twin) and without twinning behavior (dislocation slip only).

4.4 Analysis of twin evolution

4.4.1 Single crystal configuration

In what follows a deeper investigation on the evolution of twinning in single crystal configuration is performed. The numerical investigation uses the setup employed in model calibration described above.

4.4.1.1 Effect of crystal orientation

Mechanical twinning is prevalent when the resolved shear stress (RSS) in $(101)[10\bar{1}]$ direction exceeds the twinning resistance. This implies that twinning is not sensitive to deformation in certain directions (where RSS is low or negative) and sensitive to deformation in others (where RSS is positive and high). In the current study, the mechanical twinning is investigated when the compression wave aligns with two crystal orientations: (110) and (011), one of which promotes higher level of twinning.

Employing the setup of the calibration experiments, a 4.66 mm long single crystal HMX specimen is subjected to prescribed boundary velocity of 200 m/s. The spatial distributions of the resolved shear stress and twin volume fraction on twin system are recorded at seven

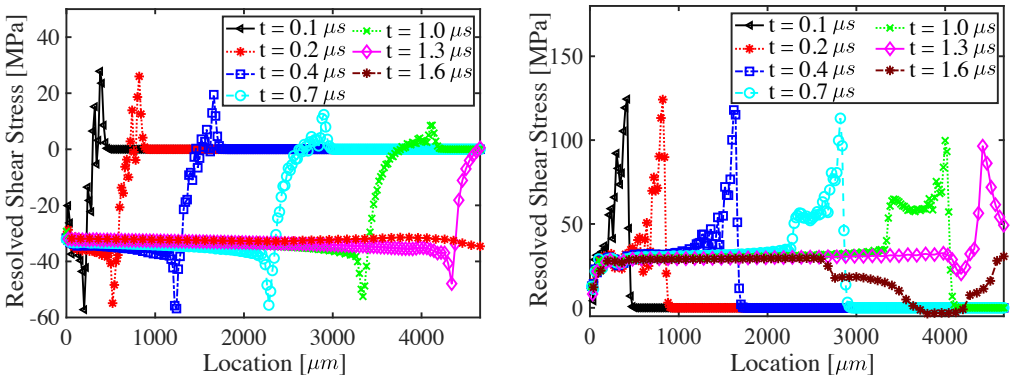

Figure 4.4: Orientation dependency of resolved shear stress in (a) the $(110)_{P2_1/n}$ direction; and (b) the $(011)_{P2_1/n}$ direction. Temporal evolution of RSS is plotted at t=0.1 μs, 0.2 μs, 0.4 μs, 0.7 μs, 1.0 μs, 1.3 μs and 1.6 μs. Location x=0 mm represents the left hand side of the specimen, and x=4.66 mm represents the HMX/PMMA interface.

time instances (i.e., t=0.1 μs, 0.2 μs, 0.4 μs, 0.7 μs, 1.0 μs, 1.3 μs and 1.6 μs) and plotted in Figs. 4.4 and 4.5. The effect of loading orientation on the stress evolution on the twin system is evident from the differences in the (011) direction (Fig. 4.4b) and the (110) direction (Fig. 4.4a). In Fig. 4.4a, specimen deformation in $(101)[10\bar{1}]$ follows the stress wave which passes through the specimen without significantly changing shape, and reaching a stable state (RSS $\approx$ -33 MPa) on the wake of the wave. In contrast, a more complex stress evolution is observed in Fig. 4.4b. Between 0 μm and 1000 μm, RSS exhibits a double peak structure once the dynamic wave has already passed. Constant stress state is reached between $\sim$500 μm and the wave front. Resolved shear stress in (110) case does not exceed 120 MPa during the entire dynamic deformation process, which leads to no twin formation. However, RSS in (011) exhibits a large peak ($>$ 120 MPa) which directly induce twin accumulation until the RSS drops below the twinning resistance (120 MPa). RSS behind the shock front is positive but lower than the resistance. At t=1.3 μs, the wave has already reflected at the HMX/PMMA interface thus the double peak structure disappears.

Figure 4.5 shows the twin volume fraction profile at a number of time instances for the (011) specimen loaded at 200 m/s velocity (Fig. 4.5a) and 500 m/s velocity (Fig 4.5b).

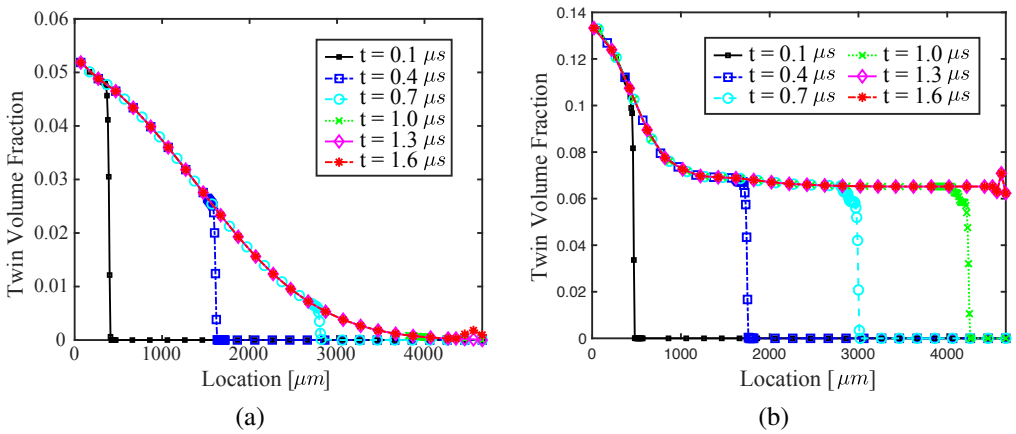

Figure 4.5: Temporal evolution of twin volume fraction at loading (1) 200 m/s, and (2) 500 m/s. Loading is along (011) direction.

The shock front is marked by the sudden increase in twinning activated by the high RSS observed at the shock front. Twinning rapidly accumulates when the resolved shear stress approaches or exceeds twinning resistance. The twin volume fraction increases from zero to a decreasing peak as the shock front propagates through the specimen. As shown in Fig. 4.5a, at t=0.1 μs, the wave arrives at approximately 400 μm (Fig. 4.5a) and the induced twin volume fraction is approximately 4.8%. At 0.4 μs, 0.7 μs and 1 μs, the induced twin volume fraction reduces to 2.6%, 0.4% and 0.1%, respectively. After the shock is reflected back at the HMX/PMMA interface, due to the relatively small impedance contrast, a slight increase in the twin concentration is observed. A similar phenomenon is observed in Fig. 4.5b.

We also observe the propagation of transition region after shock front. The twinning transition region is defined as the distance it takes for the twin to fully form at the shock front. Under 200 m/s loading at t=0.1 μs, the twinning transition region starts at x=355 μm and ends at x=411 μm. At t=0.4 μs, the transition region remains as 56 μm. The size increases to 57 μm at t=0.7 μs. The propagation of the transition region without significant size change indicates stable energy dissipation process at the wave front.

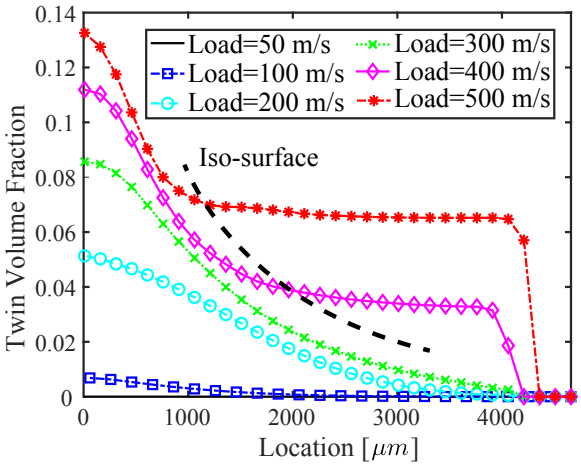

Figure 4.6: Twin volume fraction in single crystal at t=1.6 μs with loading velocity 50 m/s, 100 m/s, 200 m/s, 300 m/s, 400 m/s and 500 m/s.

4.4.1.2 Effect of impact velocity

The same specimen configuration (shot 1168) and boundary conditions as above are employed to study the response when subjected to different loading velocities in the (110) direction. At high impact velocity (500 m/s), compared with twinning at lower loading velocity (200 m/s, as shown in Fig. 4.5a), more twins are observed, and twinning accumulation reaches a steady state. The twinning transition regions at t=0.1 μs, t=0.4 μs, t=0.7 μs and t=1.0 μs increase to 60 μm, 150 μm, 210 μm and 220 μm at 500 m/s load velocity. The expansion of transition region at the higher impact velocity and more accumulated twins clearly indicate increased energy dissipation at the wave front and more plastic deformation when the impact velocity increases.

Figure 4.6 shows the spatial distribution of twin volume fraction when the dynamic wave arrives at the HMX/PMMA interface (1.050 μs, 1.046 μs, 1.034 μs, 1.022 μs, 1.014 μs and 1.000 μs under impact velocities of 50 m/s, 100 m/s, 200 m/s, 300 m/s, 400 m/s and 500 m/s). It is clear that twin volume fraction increases with the loading rate, and the maximum amount of twinning occurs at the loading boundary (x=0 μm). Maximum twin volume fraction $f_{\max}$ in 50 m/s case is less than 0.01%, while $f_{\max}$ in 500 m/s case reaches 13.26%. Other cases (400 m/s, 300 m/s, 200 m/s, 100 m/s and 50 m/s) have

maximum twin fractions 11.19%, 8.57%, 5.13% and 0.68%, respectively. Especially at higher impact velocities, a boundary region develops with high twin fraction that attenuates to a steady value in the sample interior. The attenuation is slower at lower load rates. The iso-surface plotted in Fig. 4.6 demonstrates the nonlinear relationship between the "run-to-steady-state" and the load rate. The steady state for 500 m/s case starts at approximately x=1 mm with $f \approx 6.5\%$, while in 400 m/s case, the steady region ($f \approx 3.5\%$) starts at 2 mm. Steady state region is not observed in the cases with lower applied velocities. Slight impedance mismatch at the sample-PMMA interface (x=4.66 mm) results in a perturbation of the twin volume fraction as the impact wave is reflected at the material boundary.

4.4.2 Polycrystal configurations

Particle-particle interactions could lead to stress and strain concentrations in an energetic material microstructure, and have potential links to hot-spot formation [40]. In this section, we investigate twinning in polycrystalline HMX configurations under impact loading. Polycrystalline HMX is typically synthesized to a compressed granular form or bound by a polymeric binder with small binder concentration. In the former, the microstructure includes interparticle voids, whereas in the latter, the void spaces are completely or partially filled with the binder. The current study does not include the presence of voids or binder, and focuses on the twin formation in idealized microstructures with particles fully bonded with each other. Similar assumptions have been previously employed to investigate polycrystalline energetic particles, see e.g. [60].

4.4.2.1 Microscale structures

The microscale morphologies, the boundary and loading conditions considered in the microscale simulations are shown in Fig. 4.7. Five microscale specimens subjected to high rate compression loading are investigated in this study. Each particle that comprise the microscale morphologies is idealized as a single crystal. The size of the numerical specimens is 400 $\mu m \times 400\ \mu m \times 800\ \mu m$. The orientation of each particle is sampled from a

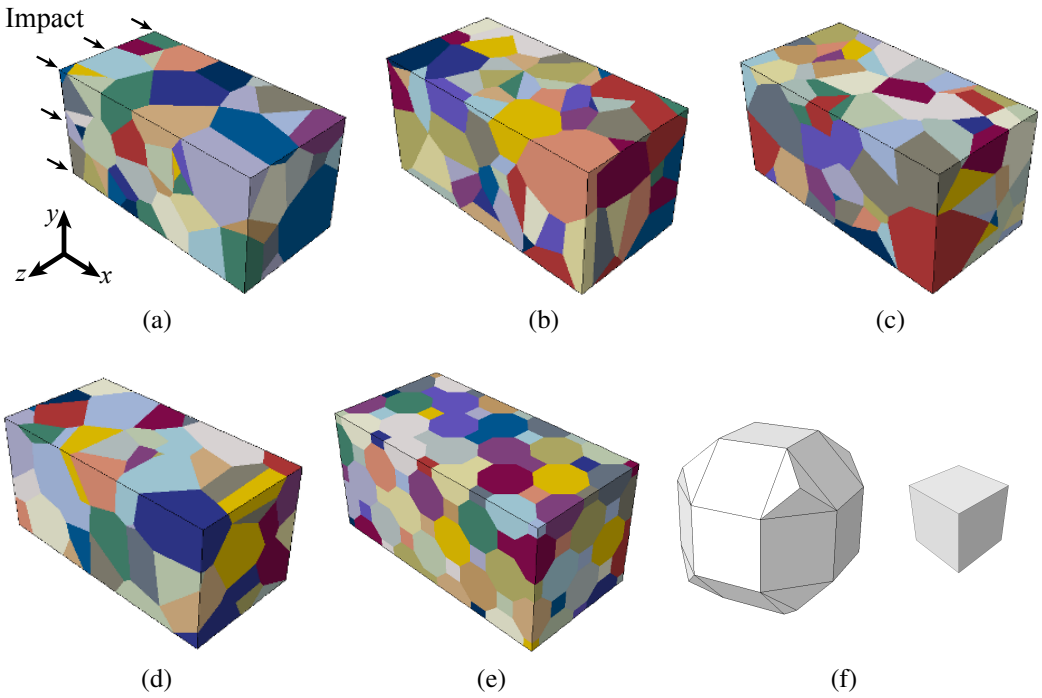

Figure 4.7: Microstructures of polycrystal configuration. Each colored region represents a single crystal particle. Impact velocity is applied on the left hand side, and the movements of top, bottom, front and back faces are constraint in their normal directions.

uniform random distribution. The three Euler angles (Kocks convention) defining the orientation of a crystal is assumed to be independent of each other, and sampled from the range of $0 < \Phi_1 < 2\pi$, $0 < \phi < \pi$ and $0 < \Phi_2 < 2\pi$. The loading is imparted on the specimens as prescribed velocity as shown in Fig. 4.7a. The displacements on the front/back/top/bottom faces are constrained in the normal directions, and free in other directions.

Four of the five microstructures (Figures 4.7a to 4.7e) include randomized polygonal particle geometries. The microstructures are generated using the Neper software [136]. A bimodal particle size distribution (see Ref. [199]) is used to create these four microstructures, each of which consists of 120 grains. The geometries are therefore four realizations with identical morphological statistics. Note that variation in the dynamic response is expected as the microstructures are not large enough to be statistically representative. Alternatively, we aggregate the responses leveraging the statistical volume concept in the analyses. The fifth microstructure, shown in Fig. 4.7e, is constructed by tiling two polyhedral particle

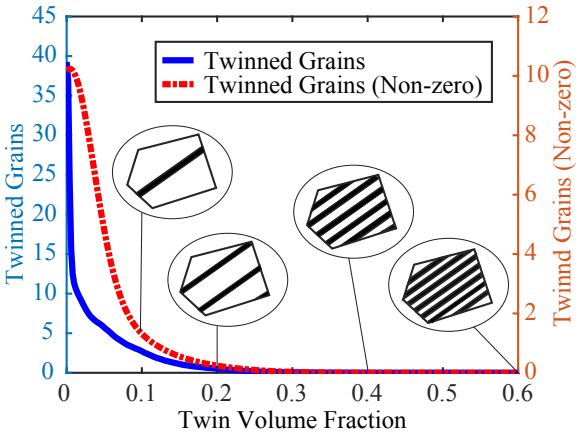

Figure 4.8: Probabilistic distribution of twin volume fraction and non-zero twin volume fraction. The twinning accumulations are schematically presented at $f = 0.1$, $f = 0.2$, $f = 0.4$ and $f = 0.6$.

shapes (Fig. 4.7f) in a regular pattern. Similar, geometrically regularized microstructures, have been employed in previous studies to investigate the dynamic response of energetic materials (e.g. Ref. [60]). The microstructures are discretized with approximately 500,000 - 1 million trilinear tetrahedral elements. Simulations are conducted using dynamic explicit finite element method. Time step sizes are chosen to ensure stability (3×10^{-6} - 1×10^{-5} μs).

To understand the overall twinning evolution, the collective distributions for twin volume fractions from the first four cases (Figures 4.7a to 4.7d) are plotted in Fig. 4.8 under the excitation amplitude of 250 m/s. A large portion of the specimens (38% volume or 182 grains), do not exhibit or exhibit a very small amount of twinning. Critical regions of high twin concentration that only exist in a limited number of locations in the microstructure.

Figure 4.9 illustrates the twin volume fraction and maximum principal strain contours as predicted using the microstructures with random (Fig. 4.7b) and regular (Fig. 4.7e) particle geometries when the shock wave front is near the end of the specimens. In both types of microstructures, high twin concentrations are observed at or near particle boundaries, which indicates the roles of interparticle misorientation and particle geometry on twin formation. Although the twin accumulation regions are likely to have relatively high strain

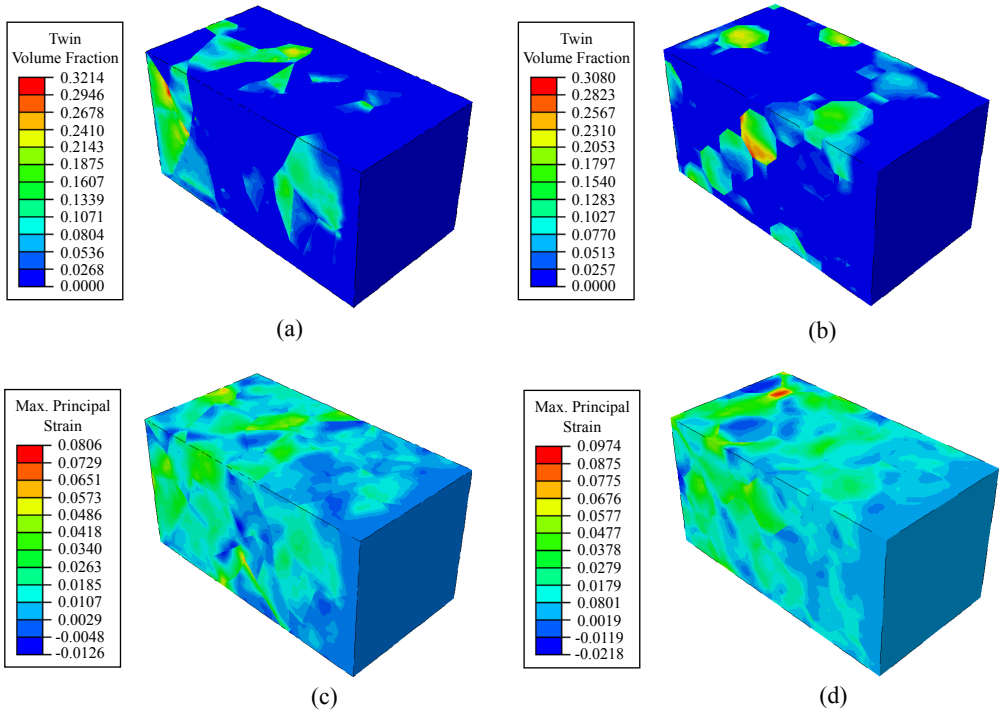

Figure 4.9: Twin volume fraction distribution of the microstructures with (a) randomized polygonal particle geometries and (b) regularized particle geometries, and maximum principal strain with (c) andomized polygonal particle geometries and (d) regularized particle geometries at t=1.6 μs.

concentration, a high strain region does not imply high twin volume fraction. The local regions with peak twin concentration in both microstructures as well as the grain orientations are shown in Fig. 4.10. In the microstructure with polygonal particles, $f_{\max} = 0.3214$ occurs at a triple junction on the boundary as plotted in Fig. 4.10a. In the microstructure with regularized particles, a column of particles aligning on the front face show high twin volume fraction, with $f_{\max} = 0.308$ observed again at a triple junction (Fig. 4.10b).

Although grain misorientations appear to characterize the local twinning initiation and accumulation behavior, the peak twin volume fraction does not show a clear connection to the grain misorientation angles. In both Fig. 4.10a and Fig. 4.10b, the highly twinned grain is next to a grain that has only a small amount of twinning, which seems to suggest an effect of crystal misorientation and grain boundary. To investigate the possible effect of grain misorientation between neighboring particles, maximum twin volume fraction dis-

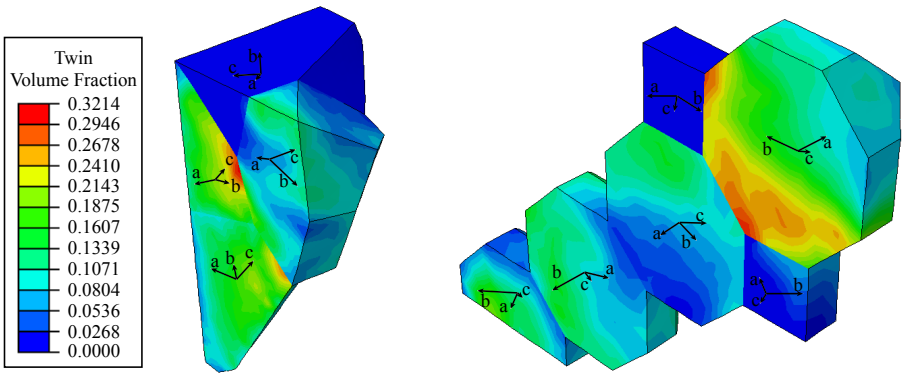

(a) (b)

Figure 4.10: Local region of twin concentration for microstructures with (1) randomized polygonal particle geometries and (2) regularized particle geometries at t=1.6 μs. Lattice axes $\boldsymbol{a}$, $\boldsymbol{b}$ and $\boldsymbol{c}$ for each grain are plotted as well. The lattice axes are not orthogonal due to the monoclinic lattice structure.

crepancy (TVFD) between each neighbor grain pair is plotted in Fig. 4.11 where mean and standard deviation are computed in five intervals for microstructures with randomized polygonal particle geometries and regularized polygonal particle geometries. The means of twin volume fraction discrepancy exhibit small values ($< \%5$) for all grain pairs in two microstructures, while the standard deviation are larger than the means, which indicates that misorientation is not clearly connected to twin concentration. In the both microstructures, mean and standard deviation of the twin volume fraction discrepancy do not show a strong dependence on the misorientation angle.

4.4.2.2 Loading velocity

The microstructure shown in Fig. 4.7b is subjected to four different impact velocities (100 m/s, 200 m/s, 300 m/s and 400 m/s) to investigate twinning evolution at different deformation rates. The simulations are performed until the shock front reaches the face of the microstructure opposing the impacted face. Total time of the simulations are 0.5 μs, 0.25 μs, 0.17 μs and 0.15 μs for impact velocities of 100 m/s, 200 m/s. 300 m/s and 400 m/s, respectively. The corresponding time step size are 2.5e-5 μs, 1.25e-5 μs, 5e-6 μs and 1e-6 μs.

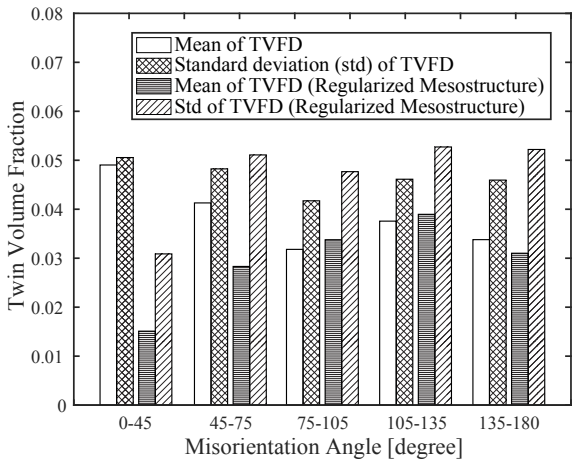

Figure 4.11: Maximum twin concentration discrepancy and misorientation in microstructures with (a) randomized polygonal particle geometries and (b) regularized particle geometries. Mean and standard deviation are computed in five intervals ((0°,45°), (45°,75°), (75°,105°), (105°,135°) and (135°,180°)).

Stress distributions of these four cases are plotted in Fig. 4.12. The stress contours are at time instances, where the wave front is approximately in the middle of the microstructure. With increasing impact velocity, the response transitions from elastoplastic wave propagation (Fig. 4.12a) to near hydrodynamic shock propagation (Fig. 4.12d). A clear separation of the shock wave is observed in the latter three simulations, while the 100 m/s case shows continuous compression trailing the wave front. Even at the highest impact velocity, stress distribution at the shock front is highly heterogeneous indicating the role of morphology on the dynamic response.

The corresponding twin volume fraction contours are shown in Fig. 4.13. The regions of the microstructure with elevated twin concentration are not significantly affected by the impact loading amplitude. Naturally, those grains, where the twin system is favorably aligned with the orientation of shock propagation exhibit significant twin volume fractions. For low to moderate impact velocities (i.e., 100-300 m/s), the sites of localized peak volume concentration occur at the triple junctions near the surface of the volume. Under the high impact velocity condition, the location of the peak volume fraction occurs at the interior of the grain near the impact surface in microstructure as shown in Fig. 4.13d. Figure 4.14

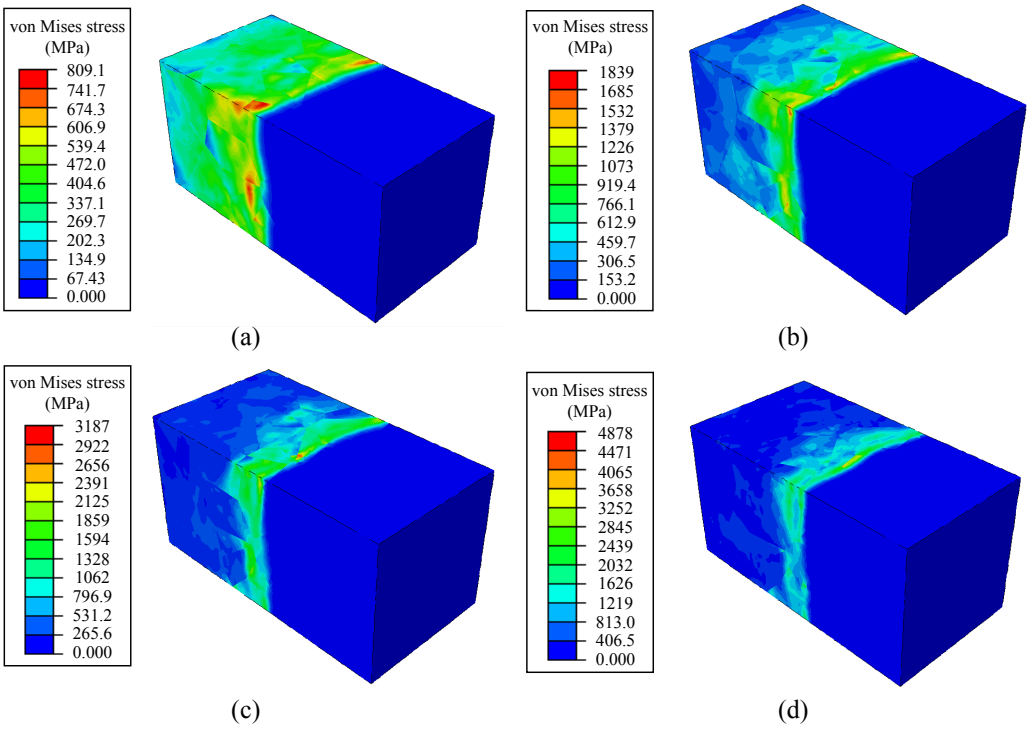

Figure 4.12: Stress contour of microscale structure subjected to impact loading (a) 100 m/s at t=0.25 μs, (b) 200 m/s at t=0.125 μs, (c) 300 m/s at t=0.098 μs and (d) 400 m/s at t=0.095 μs.

shows the relationship between the peak twin volume fraction and the applied impact velocity. At the range of loading tested in this study, a clear linear trend exists with very substantial twin concentrations (60%) at high impact velocity. Considering localized twinning concentrations as potential hot-spots in the microstructure, the simulations indicate that triple junctions could be of significance in detonation initiation.

4.5 Conclusion

This chapter presented the investigations of mechanical twinning behavior of crystalline β-HMX with respect to crystal orientation, microscale structure and loading amplitude under given shock/sub-shock impact through a large deformation CPFE framework. This chapter serves as a starting point of modeling mechanical twinning from a physics-based perspective, and it can be further improved with additional experimental data about twin-

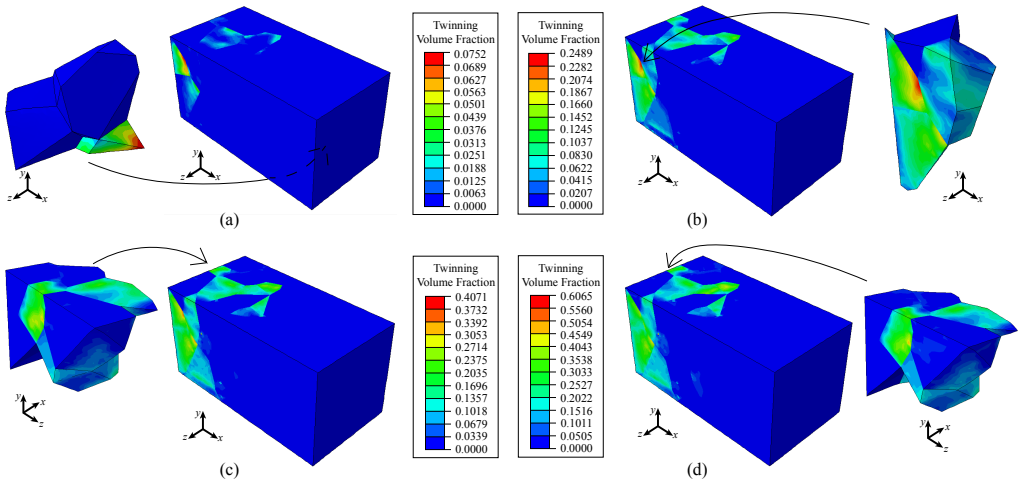

Figure 4.13: Twin volume fraction contour of microscale structure subjected to impact loading (a) 100 m/s at t=0.25 μs, (b) 200 m/s at t=0.125 μs, (c) 300 m/s at t=0.098 μs and (d) 400 m/s at t=0.095 μs.

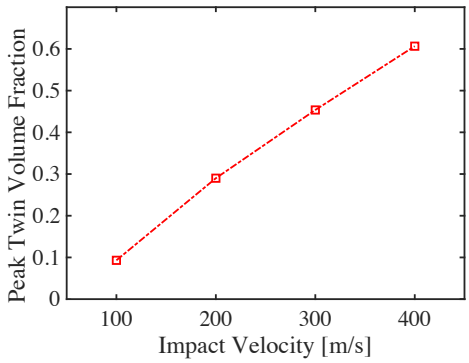

Figure 4.14: Rate-dependent twin formation in the HMX polycrystal.

ning and detwinning. The results show that the deformation twinning has strong orientation dependency in single crystal and in polycrystal configurations. Compared with the more realistic microstructure, the regularized structure generates lower peak twin volume fraction due to the reduction of sharp corners of particles. Twinning phenomenon becomes more evident at higher strain rate which further highlights the importance of modeling twinning through a physically meaningful fashion. Once more information, particularly information from lower scales, become available through experimental observation or first principle calculations, the proposed model can be improved with more accurate calibration and additional physics can be incorporated to capture material behavior at microscale.

Appendix A: Formulation Discretization

4.5.1 General Remarks

Similar to [100], the rotation matrix between crystal basis and sample basis, i.e., $\boldsymbol{e}_i = \boldsymbol{C} \cdot \boldsymbol{e}_A^c$ in Euler angles $\varphi_1, \phi, \varphi_2$ (Kocks convention) is described below:

$$[\boldsymbol{C}] = \begin{bmatrix} \cos\varphi_1\cos\varphi_2 - \sin\varphi_1\cos\phi\sin\varphi_2 & -\cos\varphi_1\sin\varphi_2 - \sin\varphi_1\cos\phi\cos\varphi_2 & \sin\varphi_1\sin\phi \\ \sin\varphi_1\cos\varphi_2 + \cos\varphi_1\cos\phi\sin\varphi_2 & -\sin\varphi_1\sin\varphi_2 + \cos\varphi_1\cos\phi\cos\varphi_2 & -\cos\varphi_1\sin\phi \\ \sin\varphi_2\sin\phi & \cos\varphi_2\sin\phi & \cos\phi \end{bmatrix} \tag{4.20}$$

with $0 < \varphi_1 < 2\pi$, $0 < \phi < 2\pi$, $0 < \varphi_2 < 2\pi$. In a numerical setting, this rotation matrix is used to transform to the sample coordinate system in configuration $\overline{\mathbb{B}}$, the time-independent orthonormal slip system vectors $(\overline{\boldsymbol{s}}_0^\alpha, \overline{\boldsymbol{m}}_0^\alpha)$ and the fourth order tensor of elastic moduli $\overline{\mathbb{C}}^e$ both of which referred to the lattice axis,

$$\overline{\boldsymbol{s}}^\alpha = \boldsymbol{C}\boldsymbol{s}_0^\alpha, \quad \overline{\boldsymbol{m}}^\alpha = \boldsymbol{C}\boldsymbol{m}_0^\alpha \tag{4.21}$$

$$\overline{\mathbb{C}}^e = (\boldsymbol{C}\underline{\otimes}\boldsymbol{C}) : \mathbb{C}^e : (\boldsymbol{C}\underline{\otimes}\boldsymbol{C})^T \tag{4.22}$$

where $(\boldsymbol{C}\underline{\otimes}\boldsymbol{C})_{ijAB} = C_{iA}C_{jB}$. In contrast with Marin [100], the current formulation use $\boldsymbol{C}$ to represent the crystal orientation at initial status. The following crystal rotation will be described through roration tensor $\boldsymbol{R}^e$. Note that the Schmid tensor $\overline{\boldsymbol{Z}}^\alpha$ in $\overline{\mathbb{B}}$ is related to the one in $\mathbb{B}$ by $\overline{\boldsymbol{Z}}^\alpha = \boldsymbol{C} \cdot \boldsymbol{Z}_0^\alpha \cdot \boldsymbol{C}^T$, where $\boldsymbol{Z}_0^\alpha = \boldsymbol{s}_0^\alpha \otimes \boldsymbol{m}_0^\alpha$.

Consider Voight (vector) notation for the stress and strain, i.e.,

$$\{\boldsymbol{\sigma}\} = \{\sigma_{11} \quad \sigma_{22} \quad \sigma_{33} \quad \sigma_{23} \quad \sigma_{13} \quad \sigma_{12}\}^T \tag{4.23}$$

$$\{\boldsymbol{E}\} = \{E_{11} \quad E_{22} \quad E_{33} \quad 2E_{23} \quad 2E_{13} \quad 2E_{12}\}^T \tag{4.24}$$

4.5.2 Pressure Dependence of Elastic Moduli

The section has not been finished. However, detailed description can be referred to Wu and Huang [185]. The pressure dependence of $\mathbb{C}^e$, or $\frac{d\mathbb{C}^e}{dp}$ is given in the crystal configuration, and transformation can be achieved by the rotation $\boldsymbol{C}$. The matrix form of $\mathbb{C}^e$ is given by

$$[\mathbb{C}^e]_0 = \begin{bmatrix} C_{11} & C_{12} & C_{13} & 0 & C_{15} & 0 \\ C_{12} & C_{22} & C_{23} & 0 & C_{25} & 0 \\ C_{13} & C_{23} & C_{33} & 0 & C_{35} & 0 \\ 0 & 0 & 0 & C_{44} & 0 & C_{46} \\ C_{15} & C_{25} & C_{35} & 0 & C_{55} & 0 \\ 0 & 0 & 0 & C_{46} & 0 & C_{66} \end{bmatrix} \tag{4.25}$$

where all coefficients are pressure dependent [1]

Matrix form of Gruneisen tensor [81] is given below:

$$\begin{bmatrix} \Gamma_{11} \\ \Gamma_{22} \\ \Gamma_{33} \\ \Gamma_{23} \\ \Gamma_{13} \\ \Gamma_{12} \end{bmatrix} = \frac{1}{\rho C_V} \begin{bmatrix} C_{11} & C_{12} & C_{13} & 0 & C_{15} & 0 \\ C_{12} & C_{22} & C_{23} & 0 & C_{25} & 0 \\ C_{13} & C_{23} & C_{33} & 0 & C_{35} & 0 \\ 0 & 0 & 0 & C_{44} & 0 & C_{46} \\ C_{15} & C_{25} & C_{35} & 0 & C_{55} & 0 \\ 0 & 0 & 0 & C_{46} & 0 & C_{66} \end{bmatrix} \begin{bmatrix} \alpha_{11} \\ \alpha_{22} \\ \alpha_{33} \\ \alpha_{23} \\ \alpha_{13} \\ \alpha_{12} \end{bmatrix} \tag{4.26}$$

[1] Thermal expansion tensor α for monoclinic β-HMX crystal has been investigated [36].

C_{11} =9.02397 + 11.0554p − 0.12183p^2,C_{12} = −1.32088 + 6.52789p − 0.10792p^2,C_{13} = −1.3792 + 7.77819p − 0.1551p^2,C_{15} = −0.2347 + 1.53836p − 0.02168p^2
C_{22} =15.56815 + 7.59921p − 0.10686p^2,C_{23} = 0.22377 + 5.7947p − 0.10229p^2,C_{25} = −3.09946 − .53953p + 5.02487$e^{-4}p^2$,C_{33} = 18.39271 + 5.90386p − 0.06176p^2
C_{35} = − 0.7547,C_{44} = 1.13088 + 3.78434p − 0.09663p^2,C_{46} = −2.41649 − 0.21976p + 5.72921$e^{-4}p^2$,C_{55} = −1.59267 + 5.16237p − 0.10296p^2
C_{66} =6.24105 + 1.352751p − 0.01491p^2, all coefficients are in the unit of GPa.

4.5.3 Constitutive Integration Scheme

The crystal constitutive model can be considered as a set of coupled first order ordinary differential equations for the variables ($\boldsymbol{\tau}$, $\boldsymbol{R}^e$, ρ). The time integration of these evolutionary equations is carried out in the sample axis and proceeds by discretizing the history in time and numerically integrating the equations over each time step. For this purpose, we consider the configurations of the body at time t_n and t_{n+1} with $t_{n+1} = t_n + \Delta t$.

This integration scheme is developed assuming (i) that the crystal deformation represented by $\boldsymbol{L}_{n+1}$ (or $\boldsymbol{D}_{n+1}$ and $\boldsymbol{W}_{n+1}$) is given [2], (ii) that the variables (p_{n+1}, $\overline{\boldsymbol{\tau}}'_n$, $\boldsymbol{R}^e_n$, ρ_n) are known, and (iii) that the time-independent slip system vectors ($\boldsymbol{s}^\alpha_0, \boldsymbol{m}^\alpha_0$), the elasticity tensor $\mathbb{C}^e$, the crystal orientation $\boldsymbol{C}$ (texture), and the plasticity material parameters (flow rule and hardening law) are input. The integration of the model will then give the updated values (p_{n+1}, $\overline{\boldsymbol{\tau}}'_{n+1}$, $\boldsymbol{R}^e_{n+1}$, ρ_{n+1}).

This numerical integration proceeds as follows. After performing some pre-processing steps, three target functions are rewritten as residual form. Numerical process of solving the target functions is established and expressed as matrix form as well. The overall integration procedure for the current CPFE model is summarized in a box for comparison with [100].

4.5.3.1 Evolution of target variables

In order to solve the unknown variables (p_{n+1}, $\overline{\boldsymbol{\tau}}'_{n+1}$, $\boldsymbol{R}^e_{n+1}$, ρ_{n+1}), four equations are required, in which the volumetric stress and deviatoric stress are described separately. A fully explicit scheme has been used for all the updates.

The first two kinematic equations (Eq. 4.5a and Eq. 4.5b) are written as

$$\overline{\dot{\boldsymbol{V}}}^{e\prime} = a(\boldsymbol{R}^{eT} \cdot \boldsymbol{D}' \cdot \boldsymbol{R}^e - \overline{\boldsymbol{D}}') \tag{4.27}$$

[2] In ABAQUS VUMAT subroutine, deformation gradients at the beginning and end of each step are given to compute the velocity gradient.

$$\dot{J} = \det(\boldsymbol{V}^e)\mathrm{tr}(\boldsymbol{D} - \overline{\boldsymbol{D}}) \tag{4.28}$$

and are integrated using a backward Euler scheme, resulting in

$$\overline{\boldsymbol{V}}^{e\prime}_{n+1} = \overline{\boldsymbol{V}}^{e\prime}_{n} + a_{n+1}(\boldsymbol{R}^{eT}_{n+1} \cdot \boldsymbol{D}'_{n+1} \cdot \boldsymbol{R}^{e}_{n+1} - \overline{\boldsymbol{D}}'_{n+1})\Delta t \tag{4.29}$$

$$J_{n+1} = J_n + \det(\boldsymbol{V}^e_{n+1})\mathrm{tr}(\boldsymbol{D}_{n+1} - \overline{\boldsymbol{D}}_{n+1})\Delta t \tag{4.30}$$

Reorganize the volumetric kinematic equation

$$J_{n+1} = J_n[1 - \mathrm{tr}(\boldsymbol{D}_{n+1} - \overline{\boldsymbol{D}}_{n+1})\Delta t]^{-1} \tag{4.31}$$

From Eq. 4.12, the plastic deformation rate $\overline{\boldsymbol{D}}_{n+1}$ can be expressed as

$$\overline{\boldsymbol{D}}_{n+1} = (1 - \sum_{\beta}^{N^{\mathrm{tw}}} f^{\beta}_{n+1}) \sum_{\alpha}^{N^{\mathrm{sl}}} \dot{\gamma}^{\alpha}_{n+1} \overline{\boldsymbol{P}}^{\alpha}_{\mathrm{sl}} + \sum_{\beta}^{N^{\mathrm{tw}}} \dot{f}^{\beta}_{n+1} \gamma^{\beta}_{\mathrm{tw}} \overline{\boldsymbol{P}}^{\beta}_{\mathrm{tw}} + \sum_{\beta}^{N^{\mathrm{tw}}} f^{\beta}_{n+1} \big(\sum_{\alpha}^{N^{\text{sl-tw}}} \dot{\gamma}^{\alpha}_{n+1} \overline{\boldsymbol{P}}^{\alpha}_{\text{sl-tw}} \big) \tag{4.32}$$

Then we can write the elastic strains at t_{n+1} as

$$\overline{E}_{V,n+1} = \ln(J_{n+1}) \quad \text{and} \quad \overline{\boldsymbol{E}}'_{n+1} = \frac{1}{a_{n+1}} \overline{\boldsymbol{V}}^{e\prime}_{n+1} \tag{4.33}$$

According to the above equations, the elasticity relationships are written at t_{n+1} as

$$\begin{aligned} p_{n+1} = -J_{n+1}\overline{\sigma}_{h,n+1} = -J_{n+1}\Big\{ & \sigma_h|_{\mathrm{EOS},n+1} + \frac{1}{3}(\overline{\boldsymbol{E}}'_{n+1} : \overline{\mathbb{C}}^{e}_{n+1} : \boldsymbol{I}) \\ & + \Big[\frac{1}{2}(\overline{\boldsymbol{E}}'_{n+1} : \frac{d\overline{\mathbb{C}}^{e}}{dp}\Big|_{n+1} : \overline{\boldsymbol{E}}'_{n+1}) + \frac{1}{3}(\overline{\boldsymbol{E}}'_{n+1} : \frac{d\overline{\mathbb{C}}^{e}}{dp}\Big|_{n+1} : \boldsymbol{I})\overline{E}_{V,n+1}\Big] \frac{dp}{d\overline{E}_V}\Big|_{n+1} - \Gamma e_{n+1} \Big\} \end{aligned} \tag{4.34}$$

$$\overline{\boldsymbol{\tau}}'_{n+1} = J_{n+1}\overline{\boldsymbol{\sigma}}'_{n+1} = J_{n+1}\Big[\mathbb{P}_d : \overline{\mathbb{C}}^{e}_{n+1} : \overline{\boldsymbol{E}}'_{n+1} + \frac{1}{3}(\mathbb{P}_d : \overline{\mathbb{C}}^{e}_{n+1} : \boldsymbol{I})\overline{E}_{V,n+1} + \boldsymbol{\Gamma}' e_{n+1}\Big] \tag{4.35}$$

On the other hand, the evolution equations for the rotation tensor $\boldsymbol{R}^e$ and the dislocation density ρ are integrated using the exponential map and a backward Euler scheme, respec-

tively,

$$\boldsymbol{R}^e_{n+1} = \exp(\Delta t \boldsymbol{W}^R_n)\boldsymbol{R}^e_n \tag{4.36}$$

where $\boldsymbol{W}^R_n$ is computed from Eq. 4.6:

$$\boldsymbol{W}^R_n = \boldsymbol{W}_n - \boldsymbol{R}^{eT}_n \cdot \overline{\boldsymbol{W}}_n \cdot \boldsymbol{R}^e_n - \frac{1}{a_n}\boldsymbol{R}^{eT}_n \cdot [\overline{\boldsymbol{V}}^{e\prime}_n \cdot (\overline{\boldsymbol{D}}'_n + \frac{1}{2a_n}\dot{\overline{\boldsymbol{V}}}^{e\prime}_n) - (\overline{\boldsymbol{D}}'_n + \frac{1}{2a_n}\dot{\overline{\boldsymbol{V}}}^{e\prime}_n) \cdot \overline{\boldsymbol{V}}^{e\prime}_n] \cdot \boldsymbol{R}^e_n \tag{4.37}$$

and

$$\dot{\rho}_{n+1} = n_1\sqrt{\rho_{n+1}}\dot{\gamma}_{n+1} - n_2\dot{\gamma}^{-1/n_3}_{n+1}\rho_{n+1}\dot{\gamma}_{n+1} \tag{4.38}$$

$$\rho_{n+1} = \left[\frac{\Delta t n_1\dot{\gamma}_{n+1} + \sqrt{(\Delta t n_1\dot{\gamma}_{n+1})^2 + 4(1+\Delta t n_2\dot{\gamma}^{1-1/n_3}_{n+1})\rho_n}}{2(1+\Delta t n_2\dot{\gamma}^{1-1/n_3}_{n+1})}\right]^2 \tag{4.39}$$

The temperature θ_{n+1} is updated using a backward Euler scheme:

$$\theta_{n+1} = \theta_n + \Delta t\dot{\theta_{n+1}}, \text{ where } c\dot{\theta_{n+1}} = \eta\sum_{\alpha=1}^{N}\tau^\alpha_{n+1}\dot{\gamma}^\alpha_{n+1} - p_{n+1}\frac{\overline{E}_{V,n+1} - \overline{E}_{V,n}}{\Delta t} \tag{4.40}$$

Equation 4.34, 4.35, 4.36, 4.38 represent a set of coupe nonlinear algebraic equations for the unknowns (p_{n+1}, $\overline{\boldsymbol{\tau}}'_{n+1}$, $\boldsymbol{R}^e_{n+1}$, ρ_{n+1}), with Eq. 4.34 giving the volumetric response, Eq. 4.36 giving the rotation, and the other two equations representing the deviatoric behavior.

4.5.4 Discretization

The above large elastic volumetric deformation CPFE formulation is discretized for computation, and will be implemented in ABAQUS VUMAT. Once the user-defined subroutine is finished, the formulation will be tested and compared at different impact velocity to simulate and demonstrate the constitutive behaviors (dislocation slip, twinning and EOS) at a large strain rate regime. Herein, the discretization of CPFE formulation is first introduced, as well as the numerical integration scheme for the proposed constitutive model. A benchmark for model behavior test is then provided for the examination of constitutive

model.

The crystal constitutive model can be considered as a set of coupled first order ordinary differential equations for the variables ($\boldsymbol{\tau}$, $\boldsymbol{R}^e$, ρ) or (p, $\boldsymbol{\tau}'$, $\boldsymbol{R}^e$, ρ), where ρ is the dislocation density. The time integration of these evolutionary equations is carried out in the sample axis and proceeds by discretizing the history in time and numerically integrating the equations over each time step. For this purpose, we consider the configurations of the body at time t_n and t_{n+1} with $t_{n+1} = t_n + \Delta t$.

This integration scheme is developed assuming (i) that the crystal deformation represented by $\boldsymbol{L}_{n+1}$ (or $\boldsymbol{D}_{n+1}$ and $\boldsymbol{W}_{n+1}$) is given, (ii) that the variables (p_{n+1}, $\overline{\boldsymbol{\tau}}'_n$, $\boldsymbol{R}^e_n$, ρ_n) are known, and (iii) that the time-independent slip system vectors ($\boldsymbol{s}^\alpha_0, \boldsymbol{m}^\alpha_0$), the crystal orientation $\boldsymbol{C}$ (texture), and the plasticity material parameters are input. The integration of the model will then give the updated values (p_{n+1}, $\overline{\boldsymbol{\tau}}'_{n+1}$, $\boldsymbol{R}^e_{n+1}$, ρ_{n+1}). In order to solve the unknown variables (p_{n+1}, $\overline{\boldsymbol{\tau}}'_{n+1}$, $\boldsymbol{R}^e_{n+1}$, ρ_{n+1}), four equations are required. The residuals are written as

$$\mathscr{R}_1 = p_{n+1} + J_{n+1}\Big\{\sigma_h|_{\mathrm{EOS},n+1} + \frac{1}{3}(\overline{\boldsymbol{E}}'_{n+1} : \overline{\mathbb{C}}^e_{n+1} : \boldsymbol{I}) + \Big[\frac{1}{2}(\overline{\boldsymbol{E}}'_{n+1} : \frac{d\overline{\mathbb{C}}^e_{n+1}}{dp_{n+1}} : \overline{\boldsymbol{E}}'_{n+1}) + \frac{1}{3}(\overline{\boldsymbol{E}}'_{n+1} : \frac{d\overline{\mathbb{C}}^e_{n+1}}{dp_{n+1}} : \boldsymbol{I})\overline{E}_{V,n+1}\Big]\frac{dp_{n+1}}{d\overline{E}_{V,n+1}} - \Gamma e_{n+1}\Big\} = 0 \tag{4.41}$$

$$\mathscr{R}_2 = \overline{\boldsymbol{\tau}}'_{n+1} - J_{n+1}\Big[\mathbb{P}_d : \overline{\mathbb{C}}^e_{n+1} : \overline{\boldsymbol{E}}'_{n+1} + \frac{1}{3}(\mathbb{P}_d : \overline{\mathbb{C}}^e_{n+1} : \boldsymbol{I})\overline{E}_{V,n+1} + \boldsymbol{\Gamma}' e_{n+1}\Big] = \boldsymbol{0} \tag{4.42}$$

$$\mathscr{R}_3 = \boldsymbol{R}^e_{n+1} - \exp(\Delta t \boldsymbol{W}^R_n)\boldsymbol{R}^e_n = \boldsymbol{0} \tag{4.43}$$

$$\mathscr{R}_4 = \rho_{n+1} - \rho_n - \Delta t(n_1\sqrt{\rho_{n+1}}\dot{\gamma}_{n+1} - n_2\dot{\gamma}^{-1/n_3}_{n+1}\rho_{n+1}\dot{\gamma}_{n+1}) = 0 \tag{4.44}$$

In this work we use a two-level iterative scheme (staggering scheme). In the first level, the residual Eq. 4.41 is solved for p_{n+1} using a N-R method by keeping ($\overline{\boldsymbol{\tau}}'_{n+1}$, $\boldsymbol{R}^e_{n+1}$, ρ_{n+1}) at their best available estimate. The linearization of the residual $\mathscr{R}_1$ with respect to p_{n+1}

leads to the following equation to be solved iteratively at each time step for the $\Delta(p_{n+1})$

$$\Big(1+J_{n+1}\frac{\partial\overline{\sigma}_{h,n+1}}{\partial p_{n+1}}\Big)\Delta(p_{n+1}) = -p_{n+1} - J_{n+1}\overline{\sigma}_{h,n+1} \tag{4.45}$$

Once a N-R solution for the pressure p_{n+1} has been obtained, the second level of the iterative procedure involves (i) a N-R solution for the deviatoric stresses $\overline{\boldsymbol{\tau}}'$ from Eq. 4.42 keeping (p_{n+1}, $\boldsymbol{R}^e_{n+1}$ and ρ_{n+1}) fixed, and (ii) simple updates for the lattice rotation $\boldsymbol{R}^e_{n+1}$ using Eq. 4.43 and dislocation density ρ_{n+1}. The linearization of the residual $\mathscr{R}_2$ with respect to $\overline{\boldsymbol{\tau}}'$ leads to the following system of five equations to be solved iteratively at each time step for the components of $\Delta(\overline{\boldsymbol{\tau}}'_{n+1})$.

$$\Big[\boldsymbol{I} - \frac{\partial}{\partial\overline{\boldsymbol{\tau}}'_{n+1}}\big(J_{n+1}\overline{\boldsymbol{\sigma}}'_{n+1}\big)\Big]\Delta(\overline{\boldsymbol{\tau}}'_{n+1}) = -\overline{\boldsymbol{\tau}}'_{n+1} + J_{n+1}\overline{\boldsymbol{\sigma}}'_{n+1} \tag{4.46}$$

With the crystal variables (p_{n+1}, $\overline{\boldsymbol{\tau}}'_{n+1}$, $\boldsymbol{R}^e_{n+1}$, ρ_{n+1}) known, the crystal Cauchy stress is computed:

$$\boldsymbol{\sigma}_{n+1} = \boldsymbol{R}^e_{n+1}\cdot\frac{1}{J_{n+1}}\overline{\boldsymbol{\tau}}_{n+1}\cdot\boldsymbol{R}^{eT}_{n+1} \tag{4.47}$$

where $\overline{\boldsymbol{\tau}}_{n+1} = \overline{\boldsymbol{\tau}}'_{n+1} - p_{n+1}\boldsymbol{I}$. The summary of the integration scheme to update the stress and state variables is given in the Appendix B.

Appendix B: Summary of Solution Scheme

1. Given quantities:

   Kinematic terms: $\boldsymbol{L}_{n+1}$, J_n or a_n, $\overline{\dot{\boldsymbol{V}}}^{e\prime}_n$, $\overline{\boldsymbol{V}}^{e\prime}_n$, $\boldsymbol{W}_n$, $\overline{\boldsymbol{W}}_n$, $\overline{\boldsymbol{D}}_n$, Δt

   Unknowns: p_n, $\overline{\boldsymbol{\tau}}'_n$, $\boldsymbol{R}^e_n$, ρ_n

   Lattice properties: $\overline{\boldsymbol{P}}^{\alpha}_{\text{sl}}$, $\overline{\boldsymbol{P}}^{\beta}_{\text{tw}}$, $\overline{\boldsymbol{P}}^{\alpha}_{\text{sl-tw}}$, Γ, Γ', $\gamma^{\beta}_{\text{tw}}$, $\overline{\mathbb{C}}^e_n$

2. Initial estimate for (p_{n+1}, $\overline{\boldsymbol{\tau}}'_{n+1}$, $\boldsymbol{R}^e_{n+1}$, $\kappa^{\alpha}_{s,n+1}$):

   thermo-elastic solution $\rightarrow p_{n+1}$, visco-plastic solution $\rightarrow \overline{\boldsymbol{\tau}}'_{n+1}$

   exponential map $\rightarrow \boldsymbol{R}^e_{n+1}$, backward Euler approx $\rightarrow \rho_n$

3. Start two-level iterative scheme to compute (p_{n+1}, $\overline{\boldsymbol{\tau}}'_{n+1}$, $\boldsymbol{R}^e_{n+1}$, $\kappa^{\alpha}_{s,n+1}$):

   (a) 1st level - Compute new estimate for p_{n+1} by solving Eq. 4.45:

   - Estimate $\dot{\gamma}^{\alpha}_{n+1}$, twin volume fraction f^{β}_{n+1} and $\dot{f}^{\beta}_{n+1}$
   - Compute the volumetric and deviatoric elastic strain (Eq. 4.33)

     $\overline{\boldsymbol{D}}_{n+1}$ (Eq. 4.12) $\rightarrow J_{n+1}$ and a_{n+1} (Eq. 4.5b) $\rightarrow \overline{\boldsymbol{V}}^{e\prime}_{n+1}$ (Eq. 4.5a) $\rightarrow \overline{\boldsymbol{E}}'_{n+1}$ and $\overline{E}_{V,n+1}$ (Eq. 4.33)
   - Compute the pure volume-pressure term $\boldsymbol{\sigma}_h|_{\text{EOS},n+1}$ using Eq. 4.10
   - Compute the bulk modulus $\frac{\partial p_{n+1}}{\partial \overline{E}_{V,n+1}}$
   - Update elastic moduli $\overline{\mathbb{C}}^e_{n+1}$ and the derivatives ($\frac{\partial \overline{\mathbb{C}}^e_{n+1}}{\partial p_{n+1}}$, $\frac{\partial^2 \overline{\mathbb{C}}^e_{n+1}}{\partial p^2_{n+1}}$)
   - Evaluate the residual $\mathscr{R}_1$ (Eq. 4.41) and $\frac{\partial \mathscr{R}_1}{\partial p_{n+1}}$ to update p_{n+1} (Eq. 4.45)

   (b) 2nd level - Compute new estimates for $\overline{\boldsymbol{\tau}}'_{n+1}$ by solving Eq. 4.46:

   - Update $\overline{\mathbb{C}}^e_{n+1}$ with the new estimated p_{n+1} from the 1st level
   - Update the crystallography terms based on the new $\overline{\boldsymbol{\tau}}'_{n+1}$

     $\dot{\gamma}^{\alpha}_{n+1}$, f^{β}_{n+1}, $\dot{f}^{\beta}_{n+1}$, $\frac{\partial \dot{\gamma}^{\alpha}_{n+1}}{\partial \overline{\tau}^{\alpha}_{n+1}}$, $\frac{\partial \dot{\gamma}^{\alpha}_{n+1}}{\partial \overline{\tau}^{\beta}_{n+1}}$, $\frac{\partial f^{\beta}_{n+1}}{\partial \overline{\tau}^{\alpha}_{n+1}}$, $\frac{\partial f^{\beta}_{n+1}}{\partial \overline{\tau}^{\beta}_{n+1}}$, $\frac{\partial (\dot{f}^{\beta}_{n+1}\gamma^{\beta}_{\text{tw}})}{\overline{\tau}^{\alpha}_{n+1}}$, $\frac{\partial (\dot{f}^{\beta}_{n+1}\gamma^{\beta}_{\text{tw}})}{\overline{\tau}^{\beta}_{n+1}}$

- Update $\overline{\boldsymbol{D}}_{n+1}$, J_{n+1}, $\overline{\boldsymbol{V}}^{e\prime}_{n+1}$, and eventually $\overline{E}_{V,n+1}$ and $\overline{\boldsymbol{E}}'_{n+1}$ (Eq. 4.12, Eq. 4.5b, Eq. 4.5a, Eq. 4.33)
- Update energy terms e_{n+1} and $\frac{\partial e_{n+1}}{\partial J_{n+1}}$ using Eq. 4.11
- Compute $\mathscr{R}_2$ (Eq. 4.42) and $\frac{\partial \mathscr{R}_2}{\partial \overline{\boldsymbol{\tau}}'_{n+1}}$ (equations in appendix)
- Exponential map, Eq. 4.43 4.6 $\rightarrow \boldsymbol{R}^e_{n+1}$
- Backward Euler approx, Eq. 4.44 $\rightarrow \rho_{n+1}$

(c) Check convergence of two-level iterative scheme:

Are the changes in p_{n+1} and $\overline{\boldsymbol{\tau}}'_{n+1}$ less than TOL?

NO, return to step (a).

YES, continue to step (4).

4. Update and save quantities for next step:

J_{n+1} or a_{n+1}, $\dot{\overline{\boldsymbol{V}}}^{e\prime}_{n+1}$, $\overline{\boldsymbol{V}}^{e\prime}_{n+1}$, $\boldsymbol{W}_{n+1}$, $\overline{\boldsymbol{W}}_{n+1}$, $\overline{\boldsymbol{D}}_{n+1}$

5. Update Cauchy stress $\boldsymbol{\sigma}_{n+1}$ using Eq. 4.47.

EXIT

Chapter 5

UNCERTAINTY QUANTIFICATION FOR FATIGUE NUCLEATION OF TITANIUM ALLOY MICROSTRUCTURE

5.1 Introduction

In this chapter, we investigate the uncertainty in fatigue nucleation of polycrystalline metallic alloy microstructures as a function of microstructural morphological uncertainties. A key contribution of the current study is that we explicitly incorporate the lamellar microstructure in Statistical Volume Element (SVE) simulations which are employed to establish the link between microstructure attribute distributions and extreme value distribution of the Fatigue Nucleation Parameter (FNP). We demonstrate the capabilities of the proposed framework on the titanium alloy Ti-6242. Key morphological features are selected based on the microstructure characteristics of Ti-6242, and available experimental measurements. The Dislocation Density informed Eigenstrain based reduced order Homogenization Model (DD-EHM) [94] is combined with the Sparse EHM and employed within the proposed framework to perform microstructure simulations defined over statistical volume elements (SVE). The probabilistic distribution of the critical FNP is taken as a mechanical property, and employed to predict the probability of failure for Ti-6242 subjected to fatigue loads.

5.2 Uncertainty Quantification Framework

The microstructure and mechanical properties of (α/β) titanium alloy are influenced by settings of processing steps, for example, cooling rate and deformation [51, 97]. To fully understand the uncertainty of mechanical properties of titanium alloy, for example, fatigue nucleation, it is necessary to establish the connection between manufacturing process and resulting material microstructures, and then investigate the material behaviors by taking the

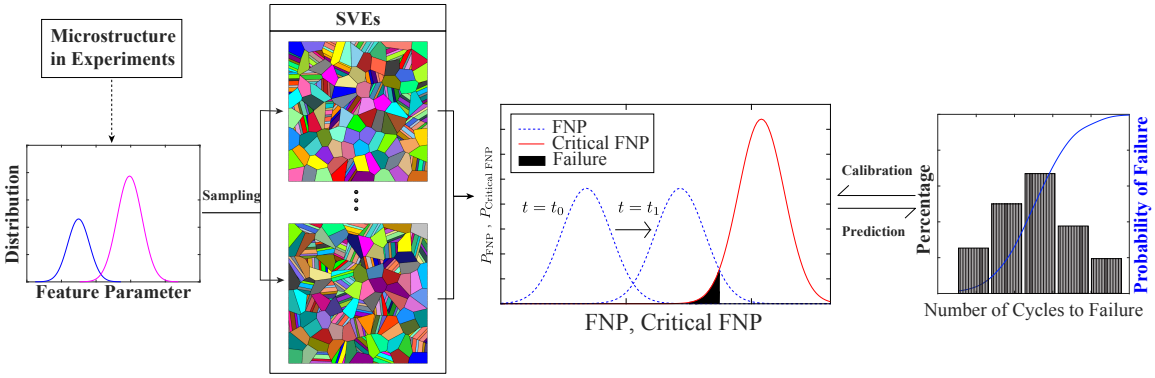

Figure 5.1: Overview of the proposed uncertainty quantification framework.

variance of microstructure into account. In the current chapter, our research focuses on the second part, which is the effect of microstructure features on fatigue nucleation, and the variance of microstructure features induced by processing settings are described by probability distributions. An uncertainty quantification framework is proposed to establish the relationship between the variability in the features that define the material microstructure and the resulting fatigue nucleation behavior, as schematically illustrated in Fig. 5.1.

While predicting fatigue nucleation, it is important to take the uncertainty in load and resistance into account. In the traditional Safety Factor method, the safety factor is simply a ratio between the maximal load not leading to failure and the maximal desired load, which does not depict the effect of uncertainty in load and resistance. In the last few decades, attempts have been made to use probabilistic calculations instead of safety factor [79, 89, 207]. In reliability engineering, both load and resistance are considered as variables, and the probability of failure is defined as the probability for exceeding a limit state within a defined reference time period. In the proposed framework, both load and resistance are obtained through the material SVEs which are constructed on material microstructure features.

Among all possible microstructures for titanium alloy, one main type of the microstructure is lamellar which consists of α-phase lamellae within large β-phase grains of several hundred microns in diameter. Increase in cooling rate leads to the reduction of colony

size, α lamellae thickness, and the nucleation of new colonies, which produces the formation of characteristic microstructure called "basket weave" or Widmanstatten microstructure [155]. To focus the investigations, we construct the probabilistic framework in the context of lamellar microstructures of Ti-6242. In the current chapter, the variability of microstructure feature is described from probabilistic point of view. The features within each microstructure, for instance volume fraction of colony grain, can be quantified and parameterized, and the variability of microstructures introduces variability of the parametric description of features. Therefore, the features are assumed to be subjected to prescribed probabilistic distribution functions which are constructed from experimental data. More details about microstructure features are provided in Section 5.4.

Statistical volume element is employed in current study to capture the variability of microstructure features as well as the uncertainty for fatigue nucleation. With the probabilistic distributions of microstructure features captured with experimental data, Monte Carlo sampling technique is utilized for the generation of microstructure realizations with different morphologoes, i.e., SVEs. The material responses of these SVEs are ensembled to approximate the distribution of FNP. A critical step is to determine the ensemble size of SVEs which is limited by the computational expense of microscale model (for example, CPFE model). Gu et al. [54] employed only 100 SVE simulations with 264 grains per SVE to prediction the statistics of the maximum FIPs in Ti-64 through the proposed statistical approach. However, the α/β colony grain was modeled as a single, homogenized microscale unit which did not explicitly take the β lath into consideration. Lucarini and Segurado [95] also employed 100 SVEs for the prediction of fatigue life for Ni-base superalloy IN718, but the number of grains within each SVE is in the order of 700. In the current study, the ensemble size of SVEs is determined by limiting the difference between the FNP distribution of arbitrary two sets of SVEs.

SVEs, and SVE simulations with calibrated Sparse DD-EHM for Ti-6242 serve as the bridge between microstructure and fatigue nucleation prediction. For a given SVE mi-

crostructure, the response under cyclic loading is computed using the Sparse DD-EHM approach for the prediction of material behavior at thousands of load cycles. In order to accelerate the expensive SVE simulations, we employed the Eigenstrain based reduced order homogenization method (EHM)[200, 201] which is a multiscale modeling approach that is endowed with a reduced order representation of the microstructure response concurrently coupled with a structural analysis capability, and it has been proposed to alleviate the computational cost of microstructure simulations. The scale bridging relations are based on the computational homogenization approach. In the current chapter, the grain scale constitutive behavior is computed using a dislocation density based crystal plasticity formulation, which is the DD-EHM. Besides, the sparse and scalable EHM model is also combined with DD-EHM to further increase computational efficiency.

In this study, fatigue nucleation is defined as a locally dissipative process that results in a microstructurally small crack formation. In the context of titanium alloys, the nucleation process is concluded by facet formation in a hard grain generally oriented along a direction near the basal plane. Therefore, we consider that the fatigue nucleation process can be captured using the concept of a fatigue nucleation parameter [50]. The Maximum relative Dislocation Density Discrepancy (MD^3) proposed by Liu et al. [94] has been used as the FNP in this study. A simulation performed over the SVE results in a distribution of Dislocation Density Discrepancy (D^3) that can be represented in the form of a probability distribution, and the MD^3 is the maximum value of D^3 over entire microstructure and history. Instead of focusing on a single extreme value MD^3, the distribution of D^3 provides a more reliable description of locally dissipative process over the entire microstructure, and this distribution could be obtained by the simulation of a large ensemble of SVEs.

An important fact is that the local dissipation process represented by the distribution of D^3 is time dependent. Therefore, it is needed to develop the ability of predicting D^3 distribution at any given time instance. However, even with the acceleration of Sparse DD-EHM, it is computationally prohibitive to execute every SVE simulation to the point where

fatigue nucleates which is in the order of several tens of thousands of cycles. Therefore, the temporal evolution of the D^3 distribution is captured at the beginning of the fatigue test through the probability distribution function, and extrapolation technique helps the estimation of D^3 distribution at thousands of cycles. As schematically demonstrated in Fig. 5.1, uncertainties in both D^3 and resistance (critical D^3) are expressed as probability density functions. The PDF of load changes as a function of time and morphology, while the PDF of resistance is assumed to be a material mechanical property and does not change with respect to time and loads. At an arbitrary time instance, there is an overlapping area (dark region in Fig. 5.1) between the probabilistic description curves of load and strength, which indicates that the load has exceed the material strength and therefore provides a qualitative measure of the probability of failure.

It is important to note that D^3 spatially varies over the material microstructure, and material is considered to be failed once the local D^3 exceeds the local critical value. Considering both the D^3 and critical D^3 as random variables, where the uncertainties are expressed as probability density functions, we can express the measure of risk in terms of the Probability Of Failure (P_f). The mathematical expression of P_f is given by:

$$P_f = \int_0^\infty F_R(\xi) f_S(\xi) d\xi \tag{5.1}$$

where $F_R(\xi)$ is the CDF of resistance at $D^3 = \xi$. $f_S(\xi)$ is the PDF of the load at $D^3 = \xi$. Distribution of P_f is shown in Fig 5.1

In our study, the probabilistic distribution of D^3 constructed by collecting D^3 between any two neighbor grains over the entire SVE ensemble. However, the critical D^3 distribution is unknown for the prediction of P_f. In the current chapter, the distribution of critical D^3 is calibrated at 95% yield stress level by fitting the probability of failure curve from experiments, and the calibrated critical D^3 PDF is employed to predict the probability of failure at 90% yield stress for validation.

Steps for the implementation and analysis are summarized as follows:

1. Establish parametric descriptions of key microstructure features, and characterize these parametric descriptions via probability distributions.

2. Employ the Monte Carlo sampling technique to create realizations (SVEs) of microstructures.

3. Perform forward simulations with Sparse DD-EHM to measure the uncertainty of fatigue nucleation prediction, and predict the temporal evolution of FNP.

4. Calibrate the probabilistic distribution of the critical FNP from experiments, and predict the probability of failure at various stress levels.

    - Construct CDF of life or number of cycle to failure from experiments
    - Compute $P_{\text{f,exp}}$ at selected cycle numbers
    - Predict the PDF of D^3 at selected cycle numbers
    - Estimate the PDF of the critical D^3
    - Compute the probability of failure ($P_{\text{f,cal}}$) based on the predicted D^3 distribution and estimated critical D^3 distribution
    - Compute residual ($P_{\text{f,exp}} - P_{\text{f,cal}}$) and go back to step 3 for optimization if not converged

5.3 Sparse DD-EHM Model

The forward simulation of the behavior of microstructure under cyclic loading is performed using the DD-EHM model. The DD-EHM model has the capability to incorporate HCP, BCC and multi-phase microstructures subjected to monotonic and cyclic loading conditions. The details of the DD-EHM model are provided in [94] and skipped here for brevity. The sparse and scalable formulation is also briefly introduced. A brief description of the key features of the Sparse DD-EHM is presented below.

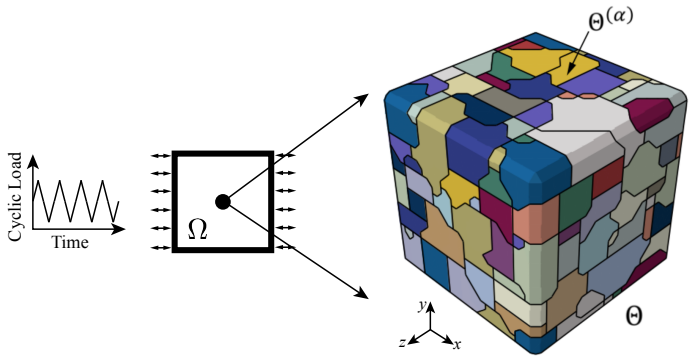

Figure 5.2: The two-scale problem: macro- and microscales.

5.3.1 Reduced Order Model

The basic idea of EHM is to pre-compute a small set of "constitutive tensors" that retain the microstructure morphological information, and employ these tensors to approximate the microstructure scale response fields using a much smaller basis obtained through constrained kinematics.

In Fig. 5.2, the macroscopic structure, denoted as Ω, is subjected to a cyclic loading, and the constitutive behavior is obtained at microscale. The macroscopic structure consists of a periodic construction of a polycrystalline microstructure, denoted as Θ. This polycrystalline microstructure is decomposed into n sub-domains (or reduced order "parts") such that $\Theta^{(\alpha)} \cap \Theta^{(\beta)} = \emptyset$ when $\alpha \neq \beta$; $\alpha, \beta = 1, 2, ..., n$, and $\cup_{\alpha=1}^{n} \Theta^{(\alpha)} = \Theta$, where $\Theta^{(\alpha)}$ denotes the domain of part α. The stress and the visco-plastic strain fields spatially vary within the microstructure in a piece-wise constant fashion, based on the reduced order partitioning of the domain.

The governing equation of the macroscale boundary value problem associated with the heterogeneous body is obtained as:

$$\nabla \overline{\boldsymbol{\sigma}}(\boldsymbol{x},t) + \overline{\boldsymbol{b}}(\boldsymbol{x},t) = \boldsymbol{0} \quad \text{for} \quad \boldsymbol{x} \in \Omega \tag{5.2}$$

in which $\overline{\boldsymbol{\sigma}}$ is the Cauchy stress at macroscale, $\overline{\boldsymbol{b}}$ the body force, and ∇ denotes the gradient

operator. The boundary conditions are given below:

$$\overline{\boldsymbol{u}}(\boldsymbol{x},t) = \overline{\boldsymbol{u}}_0 \quad \text{for} \quad \boldsymbol{x} \in \Gamma^u \tag{5.3}$$

$$\boldsymbol{n} \cdot \overline{\boldsymbol{\sigma}}(\boldsymbol{x},t) = \overline{\boldsymbol{t}}_0 \quad \text{for} \quad \boldsymbol{x} \in \Gamma^t \tag{5.4}$$

where $\overline{\boldsymbol{u}}$ is the displacement at macroscale, $\overline{\boldsymbol{u}}_0$ and $\overline{\boldsymbol{t}}_0$ are the prescribed displacement and traction on the boundaries Γ^u and Γ^t. Macroscopic strain, $\overline{\boldsymbol{\epsilon}}(\boldsymbol{x},t)$, is expressed in terms of macroscale displacement based on small deformation assumption:

$$\overline{\boldsymbol{\epsilon}} = \nabla^S \overline{\boldsymbol{u}}(\boldsymbol{x},t) \tag{5.5}$$

where ∇^S is the symmetric gradient operator.

The microscale component of the displacement field is expressed in terms of the influence function (i.e. discrete Green's functions), then the microscale constitutive equation is expressed in indicial notation:

$$M_{ijkl}^{(\beta)} \dot{\boldsymbol{\sigma}}_{kl}^{(\beta)}(\boldsymbol{x},t) - \sum_{\alpha=1}^{n} [P_{ijkl}^{(\beta\alpha)} - \delta^{(\beta\alpha)} I_{ijkl}] \dot{\boldsymbol{\mu}}_{kl}^{(\alpha)}(\boldsymbol{x},t) = A_{ijkl}^{(\beta)} \dot{\overline{\boldsymbol{\varepsilon}}}_{kl}(\boldsymbol{x},t) \tag{5.6}$$

where $\boldsymbol{\sigma}^{(\beta)}$ is the Cauchy stress of part β at microscale, $\boldsymbol{\mu}^{(\alpha)}$ the inelastic strain in part α, $\boldsymbol{\delta}$ is the Kronecker delta function, $\boldsymbol{I}$ the fourth order identity tensor. $\boldsymbol{M}^{(\beta)}$ is the compliance tensor. $\boldsymbol{P}^{(\beta\alpha)}$ and $\boldsymbol{A}^{(\beta)}$ are the interaction and concentration tensors. Macroscale stress is then computed as the volume average of the part-average stress coefficients:

$$\overline{\boldsymbol{\sigma}}_{ij} = \sum_{\beta=1}^{n} \frac{|\Theta^{(\beta)}|}{|\Theta|} \boldsymbol{\sigma}_{ij}^{(\beta)} \tag{5.7}$$

Consider the texture and dislocation slip as the source of plastic deformation, the inelastic

strain in part α is described by the dislocation slip over slip systems:

$$\dot{\mu}_{ij}^{(\alpha)}(\boldsymbol{x},t) = \sum_{s=1}^{N} \dot{\gamma}^{s(\alpha)}(\boldsymbol{x},t) Z_{ij}^{s(\alpha)} \tag{5.8}$$

where $\boldsymbol{Z}^{s(\alpha)}$ is the Schmid tensor of slip system s in part α, and $\boldsymbol{Z}^{s(\alpha)} = \boldsymbol{n}^{s(\alpha)} \otimes \boldsymbol{m}^{s(\alpha)}$ where $\boldsymbol{n}^{s(\alpha)}$ and $\boldsymbol{m}^{s(\alpha)}$ are the slip direction and normal of the slip plane.

The primary obstacle of computational efficiency for the above EHM model with increasing number of grains is the dense and unsymmetric linear system with a dimension of $6n$. In the sparse and scalable EHM formulation, computational efficiency is increased by introducing sparsity into the Jacobian matrix of the linearized EHM system. The interaction between two adjacent grains $\overline{\alpha}$ and $\overline{\beta}$ can be neglected to enforce off-diagonal components in the system Jacobian matrix two 6×6 zero blocks, then a structurally symmetric sparse linear system is obtained. The sparsity of the resulting system is naturally determined by the extent of neglected interactions. The consequences of partial consideration of grain-to-grain interactions are provided in Zhang and Oskay [201].

Strain compatibility constrained sparse EHM (ε-EHM) has been used to meet the requirement that the average of strains in each part is equal to the maroscale strain. For arbitrary pair of grains, the interaction is to be neglected. The new sparse set of interactions tensors are set to zero. The compliance tensors remain the same. To enforce the strain compatibility, the effect of the neglected transmitted interaction tensors are lumped to the self-induced ones Zhang and Oskay [201].

5.3.2 Dislocation Density Based Crystal Plasticity

A dislocation-mediated plasticity model has been adopted [93]. The slip rate at the s^{th} system is derived from the Orowan's equation:

$$\dot{\gamma}^{s} = \frac{\rho_{\text{m}}^{s} v_{\text{id}}^{s} (b^{s})^{2}}{2} \text{sign}(\tau^{s}) \exp\left(\frac{-\Delta F^{s}}{k\theta}\right) \exp\left(\frac{(\tau^{s} - s^{s})\Delta V^{s}}{k\theta}\right) \tag{5.9}$$

where ρ_{m}^{s} is the average mobile dislocation density, v_{id}^{s} the vibration frequency of the dislocation segment, b^{s} the magnitude of the Burgers vector, k the Boltzmann constant and θ the temperature in Kelvin, ΔV^{s} the thermal activation volume, and ΔF the activation energy. s^{s} is the critical resolved shear strength, and the strength hardening is expressed as

$$s^{s}(\dot{\gamma}^{s}) = s_{0}^{s} + s_{\mathrm{for}}^{s}(\dot{\gamma}^{s}) + s_{\mathrm{deb}}^{s}(\dot{\gamma}^{s}) \tag{5.10}$$

where s_{0}^{s} is the initial slip resistance, $\dot{\gamma}^{s}$ is the slip rate at s^{th} slip system, s_{deb}^{s} and s_{for}^{s} denote the contributions to strength evolution by dislocation debris and forest dislocations, respectively.

$$s_{\mathrm{for}}^{s}(\dot{\gamma}^{s}) = \mu \chi b^{s} \sqrt{\rho_{\mathrm{for}}^{s}} \tag{5.11}$$

$$s_{\mathrm{deb}}^{s}(\dot{\gamma}^{s}) = \mu b^{s} k_{\mathrm{deb}} \sqrt{\rho_{\mathrm{for}}} \ln\left(\frac{1}{b^{s}\sqrt{\rho_{\mathrm{deb}}}}\right) \tag{5.12}$$

where μ is the shear modulus, χ is the dislocation interaction parameter, b^{s} is the Burgers vector. ρ_{for}^{s} and ρ_{deb}^{s} represent the forest and debris dislocation density, respectively. k_{deb} is the material independent factor associated with low substructure dislocation density.

The total forest dislocation density is expressed as:

$$\rho_{\mathrm{for}}^{s} = \rho_{\mathrm{fwd}}^{s} + \rho_{\mathrm{rev}}^{s+} + \rho_{\mathrm{rev}}^{s-} \tag{5.13}$$

where ρ_{fwd}^{s} is the forward dislocation density and $\rho_{\mathrm{rev}}^{s\pm}$ denote the reversible terms corresponding to loading and unloading paths along the s^{th} slip system. The evolution of the forward dislocation density includes both athermal storage and temperature dependent recovery of classical Kock-Mecking law, as given below:

$$\frac{\partial \rho_{\mathrm{fwd}}^{s}}{\partial \gamma^{s}} = (1-p) k_{1}^{s} \sqrt{\rho_{\mathrm{for}}^{s}} - k_{2}^{s}(\dot{\gamma}, \theta) \rho_{\mathrm{for}}^{s} \tag{5.14}$$

where p is a reversibility parameter. k_{1}^{s} controls the generation of forest dislocations, and

the recovery coefficient k_2^s is taken to be:

$$k_2^s(\dot{\gamma},\theta) = k_1^s \frac{b^s \chi}{g^s}[1 - \frac{k\theta}{\hat{D}^s b^{s^3}} \ln \frac{\dot{\gamma}^s}{\dot{\gamma}_0}] \tag{5.15}$$

where $\dot{\gamma}_0$, g^s and $\hat{D}^s$ are the reference shearing rate, effective activation enthalpy and drag stress, respectively. The evolution of the remaining two components, ρ_{rev}^{s+} and ρ_{rev}^{s-} are expressed as functions of loading direction in the slip system:

$$\frac{\partial \rho_{\text{rev}}^{s+}}{\partial \gamma^s} = \mathbb{H}\big(\text{sign}(\tau^s)\big)\Big(pk_1^s\sqrt{\rho_{\text{for}}^s} - k_2^s(\dot{\gamma}^s,\theta)\rho_{\text{rev}}^{s+}\Big) + \mathbb{H}\big(\text{sign}(-\tau^s)\big)\Big[-k_1^s\sqrt{\rho_{\text{for}}^s}(\frac{\rho_{\text{rev}}^{s+}}{\rho_0^s})^{\hat{m}}\Big] \tag{5.16}$$

$$\frac{\partial \rho_{\text{rev}}^{s-}}{\partial \gamma^s} = \mathbb{H}\big(\text{sign}(\tau^s)\big)\Big(-k_1^s\sqrt{\rho_{\text{for}}^s}(\frac{\rho_{\text{rev}}^{s-}}{\rho_0^s})^{\hat{m}}\Big) + \mathbb{H}\big(\text{sign}(-\tau^s)\big)\Big[pk_1^s\sqrt{\rho_{\text{for}}^s} - k_2^s(\dot{\gamma}^s,\theta)\rho_{\text{rev}}^{s-}\Big] \tag{5.17}$$

where $\mathbb{H}$ is the heaviside function, ρ_0^s the total dislocation density at the point of load reversal, $\hat{m}$ the dislocation density recombination coefficient.

The evolution of the debris dislocation density is expressed as:

$$d\rho_{\text{deb}} = \sum_s \frac{\partial \rho_{\text{deb}}^s}{\partial \gamma^s} d\gamma^s, \quad \text{and} \quad \frac{\partial \rho_{\text{deb}}^s}{\partial \gamma^s} = qb^s\sqrt{\rho_{\text{deb}}}k_2^s(\dot{\gamma}^s,\theta)\rho_{\text{for}}^s \tag{5.18}$$

where q is the recovery rate coefficient.

5.4 Microscale Structure

5.4.1 SVE Morphology

In current study, three important features of the microstructure of Ti-6242, crystal orientation, the presence of colony grain and the lamella structure with both α lath and β lath, are considered and analyzed through the proposed framework. Particularly, three feature parameters of Ti-6242 are taken into account: crystal orientation of prior β grain, colony grain volume fraction and α/β lath thickness.

It is known that the orientation of α phase depends on the metallurgical high tempera-

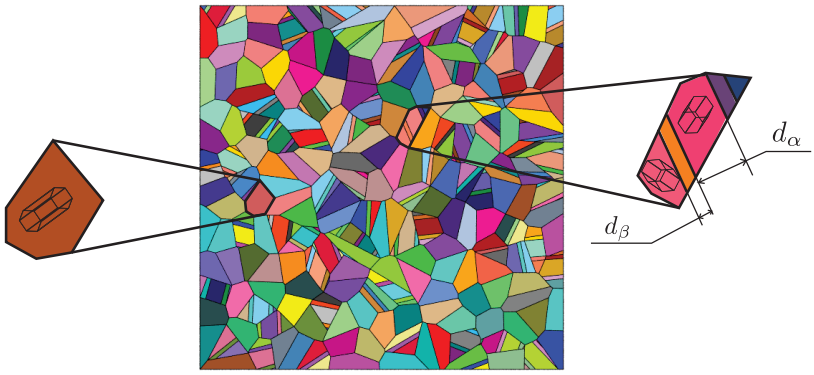

Figure 5.3: Microstructures features.

ture state. After a heat treatment in the β-field alone, the inherited α texture was obtained from the texture of the parent β grain without variant selection. With a mechanical deformation in the β field, the resulting α texture at room temperature is inherited with variant selection. Therefore, for arbitrary Ti-6242 SVE, both the mechanical deformation and orientation of the prior β grain should be provided to obtain the crystal orientations of α phases in the microstructure. In the current chapter, the mechanical deformation is considered as rolling and the rolling direction is assumed to be in loading direction. The Euler angles of prior β grain are randomly selected in the range of $[0^\circ, 90^\circ]$.

Orientation relationship between the room temperature α phase and high temperature β phase is subjected to Burgers Orientation Relationship (BOR):

- $(110)_\beta /\!/ (0001)_\alpha$
- $[\bar{1}1\bar{1}]_\beta /\!/ [2\bar{1}\bar{1}0]_\alpha$

Therefore, there are only 12 possible variants in titanium alloy Ti-6242. In fact, only a small subset of variants is formed. In the current chapter, variant selection is performed with the variant selection function proposed by Gey et al. [48]. Let's denote the orientation of i^{th} α variant as $g_i^\alpha$and the orientation of the prior β grain as g^β, then

$$g_i^\alpha = \{b_i g^\beta\}_{i=1,2,\ldots,12} \tag{5.19}$$

where b_i is the BOR for the i^{th} variant. The crystalline volume of the i^{th} α variantis related to the parent volume $f^{\beta}(g^{\beta})$ by

$$f_i^{\beta} = v_i \cdot f^{\beta}(g^{\beta}) \tag{5.20}$$

where v_i is the variant selection function defined by

$$v_i = \frac{|\gamma_i|}{\sum_{\gamma_0}^{|\gamma|_{\max}} |\gamma|} \tag{5.21}$$

where $\gamma_0 = X\%|\gamma|_{\max}$ is the minimum resolved shear strain that corresponding α variant is possible to form, and $|\gamma|_{\max}$ is the maximum amplitude of resolved shear strain among all slip systems under given thermo-mechanical loading. Following [48], X is selected as 50 in the current study.

Experimental efforts are put on the measurement of Ti-6242 microstructure features and the effect of microstructure on the material behaviors. Deka et al. [33] measured the volume fraction of the transformed β phase and primary α grain in the overall Ti-6242 microstructure to be 30 percent and 70 percent. Within the colony grain, α and β lamellae were experimentally observed to have volume fractions of approximately 88 percent and 12 percent, respectively. Gigliotti et al. [51] investigated four microstructures of Ti-6242 produced by different processing conditions, and measured the size of pure α grain and colony through light microscopy. Jun et al. [75] determined the volume fraction of α and β phase of Ti-6242 and Ti-6246 through the secondary election micrographs. In Ti-6242, measured values are 90 percent and 10 percent for α and β phase. Qiu et al. [135] conducted dwell fatigue tests for T924x (x=2,3,4,5,6) alloys to demonstrate that alloy composition, microstructure, and microtexture all influence the dwell effect. In the Ti-6242 specimen, the nearly equiaxed microstructures consists of α grains and transformed β phase, and the grain size and volume fraction of α grains are approximately $13.6\mu m$ and 90 percent. Sansoz and Ghonem [147] performed scanning electron microscope examinations on the fracture surface of three microstructures in order to identify the relevant crack

growth mechanisms with respect to the loading frequency and the microstructure details. In these three microstructures, the average thicknesses of α lath are quite different (0.7, 2.0 and 5.9 mm), while the average thickness of the β lath is found to be similar in all produced microstructures (0.2 mm). Jun et al. [76] studied local deformation mechanisms in Ti-6242 by performing in-situ micropillar compression tests on nine different pillars, and they concluded that, for these colony structures, the presence and morphology of the β phase can significantly alter the apparent yielding point and work hardening response. The widths of α and β lath in the as-received specimen are approximately 2 mm and 0.5 mm, while the averaged thicknesses in the nine processed specimens are around 3.7 mm and 0.8 mm for α and β lath, respectively.

In microscale modeling of Ti-6242, these attributes are selected to approximate the desired microstructures. Ashton et al. [5] investigated the role of α phase ligament width on the micro-mechanical behavior of dual-phase titanium alloys through a CPFE model, and the width are 1.0 μm, 2.0 μm and 5.0 μm. The β lath thickness is fixed at 0.5 μm for all numerical tests. Zhang and Dunne [204] employed a crystal plasticity model to investigate the response of the differing microstructure-level morphological units (colony to basketweave) and their role in determining strain rate sensitivity. For the unit cell structure in Ti-6242, the β lath morphological orientations are selected at 0, 20, 45 and 90 degree, and the thickness of β lath varies from 0.6 μm, 1.5 μm to 2.5 μm to achieve the volume fraction at 6 percent, 12 percent and 20 percent. Zhang and Dunne [205] investigated slip transfer and load shedding across the differing phases in both α/β colony structure and four variant α/β basketweave structure. While changing the α variant, the thickness of β lath changes from 1.6 μm to 3.2 μm Waheed et al. [175] performed stress relaxation test simulations for equiaxed pure α, colony, Widmanstatten and basketweave microstructures to investigate the effect of α grain size and dislocation penetration on rate sensitivity. In their study, the width of the α lath is fixed at 2.5 mm and the b volume fraction is fixed at 20 percent. According to the experimental observations and numerical settings of the Ti-6242

Variable	Lower Bound	Upper Bound
V_α	0.65	0.95
d_α	$2.0\mu m$	$5.0\mu m$
d_β	$0.5\mu m$	$1.0\mu m$
$\theta_1^\beta, \theta_2^\beta, \theta_3^\beta$	0°	90°

Table 5.1: Morphology parameters.

microstructure, the upper and lower bound of microstructure parameters are selected and summarized in Table. 5.1.

5.4.2 Numerical Settings

To ensure that the constitutive formulation captures the response of the near-α titanium alloy Ti-6242, model parameters calibrated by [94] are employed and summarized below. Idealized microstructure based on the variability of features is also presented. The FNP employed in the current study is presented as well as its temporal evolution a SVE forward simulation.

5.4.2.1 Model Parameters

There are two phase existing in the α/β titanium alloy Ti-6242. The constitutive parameters of both phases in the Sparse DD-EHM approach are presented as well as the morphology of bi-model microstructure for Ti-6242. Flow rule parameters and hardening rule parameters are provided.

Table 5.3 summarizes the parameters of flow rule for both the HCP and BCC grains used in the uncertainty quantification studies. The HCP model includes 30 slip systems including the basal, pyramidal and prismatic systems. The BCC model includes 48 slip systems. All slips systems are summarized in Table. 5.2. The model parameters are calibrated by [94].

The strength hardening evolution in HCP dominated crystals is controlled by initial slip resistance, forest dislocation and debris dislocation, and corresponding parameters are

Lattice	Type	Slip system	Number
HCP	Basal $\langle$a$\rangle$	$\{0001\}\langle 11\bar{2}0\rangle$	3
	Prismatic $\langle$a$\rangle$	$\{10\bar{1}0\}\langle 11\bar{2}0\rangle$	3
	Pyramidal $\langle$a$\rangle$	$\{10\bar{1}1\}\langle 11\bar{2}0\rangle$	6
	1st Order Pyramidal $\langle$c+a$\rangle$	$\{10\bar{1}1\}\langle 11\bar{2}3\rangle$	12
	2nd Order Pyramidal $\langle$c+a$\rangle$	$\{11\bar{2}2\}\langle 11\bar{2}3\rangle$	6
BCC		$\{110\}\langle 1\bar{1}1\rangle$	12
		$\{112\}\langle 12\bar{1}\rangle$	12
		$\{123\}\langle 11\bar{1}\rangle$	24

Table 5.2: Slip system of HCP and BCC.

Parameter	Unit	Basal $\langle$a$\rangle$	Prismatic $\langle$a$\rangle$	Pyramidal $\langle$a$\rangle$	Pyramidal $\langle$c+a$\rangle$	$\{110\}(\bar{1}11)$
ΔF^s	$\times 10^{-19}$J	2.58	2.93	3.21	3.44	2.27
ΔV^s	$\times 10^{-29} m^3$	1.94	2.84	2.96	3.17	479
ρ_m^s	$\times 10^{12} m^{-2}$	5	5	5	5	5
v_{id}^s	$\times 10^{12} Hz$	1	1	1	1	1
b^s	$\times 10^{-4} \mu m$	3.54	3.58	3.59	6.83	2.86
s_0^s	MPa	11.6	47.2	143.69	158.87	94
k_1^s	$\times 10^{6} m^{-1}$	6.32	107	103	174	52
D^s	MPa	100	150	185	225	230

Table 5.3: Flow rule parameters for HCP and BCC crystals.

summarized in Table 5.4. The dislocation interaction parameter χ is set as 0.9 to satisfy the Taylor relationship [17]. The material independent factor k_{deb} is set as 0.086 [98]. A small value of initial forest dislocation density is adopted, $\rho_{\text{for},0} = 1 \times 10^{12} m^{-2}$, according to experimental observations [172, 118, 108]. The reversibility parameter p is chosen as 0.8 [83]. The reference shear strain rate $\dot{\gamma}_0$ is defined as $10^7 s^{-1}$. The dislocation density recombination coefficient $\hat{m}$ is taken to be 0.4 for HCP and BCC [197]. The initial debris dislocation density in all slip systems are defined as $1 \times 10^{10} m^{-2}$ [1].

5.4.2.2 Load and Boundary Conditions

Figure 5.4 shows the morphology, loading and boundary conditions for one of the SVE microstructure considered in this study. The microstructures are generated using the Neper software [136]. The mesh of the microstructures consist of around 60,000 wedge elements

Parameter	χ	k_{deb}	$\rho_{\text{for},0}$	p	$\dot{\gamma}_0$	$\hat{m}$	$\rho^s_{\text{deb},0}$
Unit			m^{-2}		s^{-1}		m^{-2}
Value	0.9	0.086	1×10^{12}	0.8	10^7	0.4	1×10^{10}

Table 5.4: Hardening rule parameters.

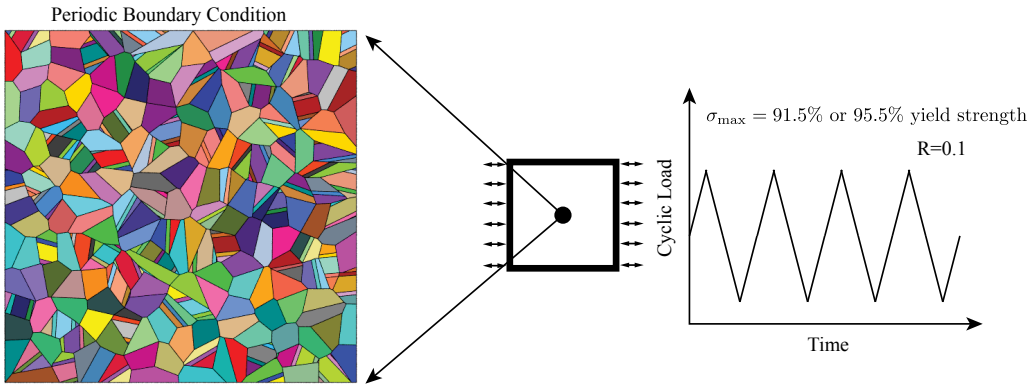

Figure 5.4: Cyclic loading.

to capture the localized stress and dislocation density evolution. The size of the numerical specimen is 39.135 mm × 39.135 mm that is made of 150 grains (primary α or colony grain) with random orientations generated from variant selection. The cyclic loading is applied from the left and right edge of the specimen, where the maximum stress is 91.5% or 95.5% yield strength, R ratio is 0.1, and load frequency is 10 Hz. The total duration of the SVE simulation is 1 second (10 cycles), with maximum time step size of 0.01 s. The geometry is modeled as a quasi 2D domain with three dimensional discretization, and periodic boundary condition is applied to all three direction. The out of plane direction (the thickness direction) only contains a single set of elements. The size of the grains are sampled from a bimodal distribution [94].

The yield strength of It-6242 is estimated through a tension test simulation. Strain-controlled load in x direction is applied on the Sparse DD-EHM model with 145 grains in the microstructure as shown in Fig. 5.2. The yield stress is estimated as 880 MPa from the tension test where load rate is $0.01/s$.

5.4.2.3 FNP and Motion Preditions

Fatigue behavior of Ti-6242 subjected to fatigue loading is predicted by the Sparse DD-EHM and idealized microstructure, while the onsite of fatigue is determined by FNP. There are numerous fatigue parameters that has been used with microscale constitutive model for the prediction of fatigue life. Fatemi and Socie [39] proposed the Fatemi–Socie (FS) damage parameter to predict multiaxial fatigue life under both in-phase and out-of-phase loading conditions. Przybyla and McDowell [134] employed the maximum plastic shear strain range (MPSS) and FS damage parameter to investigate driving forces for fatigue crack formation at the scale of microstructure. Liu et al. [94] proposed the MD^3 considering that dislocation pile-ups at the grain boundary has main effect on crack nucleation, and the amount of pile-ups is quantified by the D^3.

The relative Dislocation Density Discrepancy (D^3) for grain i, $(\Delta\rho_{\text{tot}})^i$,is defined as the maximum dislocation density discrepancy between grain i and its neighbors. The maximum value of D^3 over the entire SVE, i.e., the Maximum Relative Dislocation Density Discrepancy (MD^3), $\Delta\rho_{\text{tot}}$, has been used as the FNP.

$$\Delta\rho_{\text{tot}} = \max_{i\in\{1,\dots,n\}} \left\{ (\Delta\rho_{\text{tot}})^i \right\} \tag{5.22}$$

$$(\Delta\rho_{\text{tot}})^i = \max_{j\in\{1,\dots,m_i\}} \left\{ \left| (\rho_{\text{tot}})^i - (\rho_{\text{tot}})^{k(j)} \right| \right\} \tag{5.23}$$

where $(\rho_{\text{tot}})^i$ is the maximum dislocation density for grain i over all slip systems, ρ_{tot} is the total dislocation density defined as $\rho_{\text{tot}} = \rho_{\text{for}} + \rho_{\text{deb}}$.

5.5 Fatigue Nucleation Prediction With Uncertainty

5.5.1 SVE ensemble size

In the UQ analysis with SVEs, the ensemble size is determined by comparing the aggregated D^3 distributions with different ensemble sizes. The variation of material response

under fatigue loading condition is investigated by performing 10,258 SVE simulations and analyzing their aggregated response. Within each SVE, morphology parameters are randomly sampled from their probability distribution.

For any given ensemble size, arbitrary two sets of SVEs will generate different aggregated D^3 distributions, and the difference can be reduced by increasing the ensemble size. In general, larger ensemble size produces smaller variation of the aggregated material response, which indicates that the difference of aggregated responses between any two sets of SVEs with the same ensemble size should be within given tolerance if the ensemble size is considered to be sufficient. To find appropriate ensemble size, six different ensemble sizes (100, 250, 500, 750, 1000, 2000) have been investigated in this section. For any ensemble size z, fifty sets of SVEs are randomly selected from the 10,258 simulation pool, and each set contains z number of SVEs. The aggregated D^3 distribution of each set is constructed by gathering all D^3 in all SVE simulations within given set.

As presented in Section 5.4.1, morphology parameters of Ti-6242 fall in the ranges listed in Table 5.1. In the current chapter, all features are assumed to be subjected to uniform distributions with boundaries defined in Table 5.1. Each pure α grain that comprise the microscale morphologies is idealized as a single crystal, while each colony grain contains multiple α variants with prescribed thickness (d_α) as well as β lath. Five SVE microstructures generated from the given probabilistic distributions are provided as examples in Fig. 5.5. The the number of grains in the numerical specimens shown in Fig. 5.5 are 25, 50, 100, 150, and 200. The orientation of each grain and α/β lath is sampled based on the variant selection function. The three Euler angles (xxx convention) defining the orientation of a crystal is assumed to be independent of each other, and sampled from the range of $0 < \Phi_1 < \pi/2, 0 < \Phi < \pi/2$ and $0 < \Phi_2 < \pi/2$. These microstructures are generated using the Neper software [136]. Grain size distribution proposed by [94] has been employed. In the current chapter, the SVE size with 150 grains is applied for each microstructure, and we aggregate the responses in the analyses.

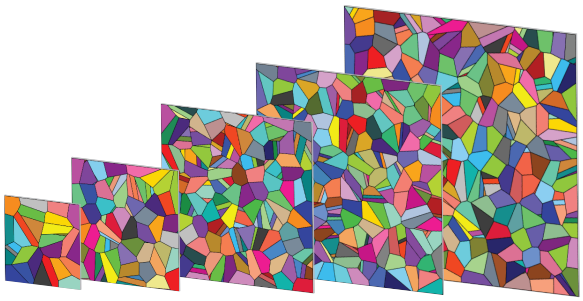

Figure 5.5: SVE sizes.

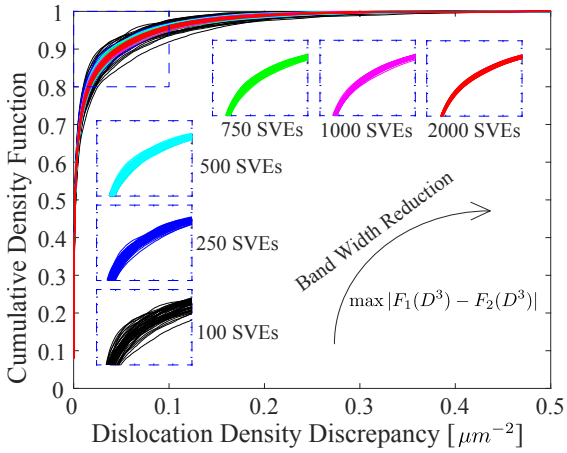

Figure 5.6: Variability of D^3 CDF.

Convergence of the aggregated D^3 distribution, particularly, cumulative distribution function (CDF), with increasing ensemble size is shown in Fig. 5.6. The band width for each ensemble size represents the variation of the aggregated D^3 distribution, and a clearly narrowing trend is observed while the ensemble size increases.

To quantify the variation of the aggregated D^3 distribution, the Kolmogorov–Smirnov test (K–S test or KS test) is used to compare two aggregated D^3 distributions with the same ensemble size. The Kolmogorov–Smirnov statistic $D^\star$ for arbitrary two sample cumulative distribution functions, $F_1(x)$ and $F_2(x)$ is defined as

$$D^\star = \max_x(|F_1(x) - F_2(x)|) \tag{5.24}$$

The variation of the aggregated response is quantified by computing the KS statistics be-

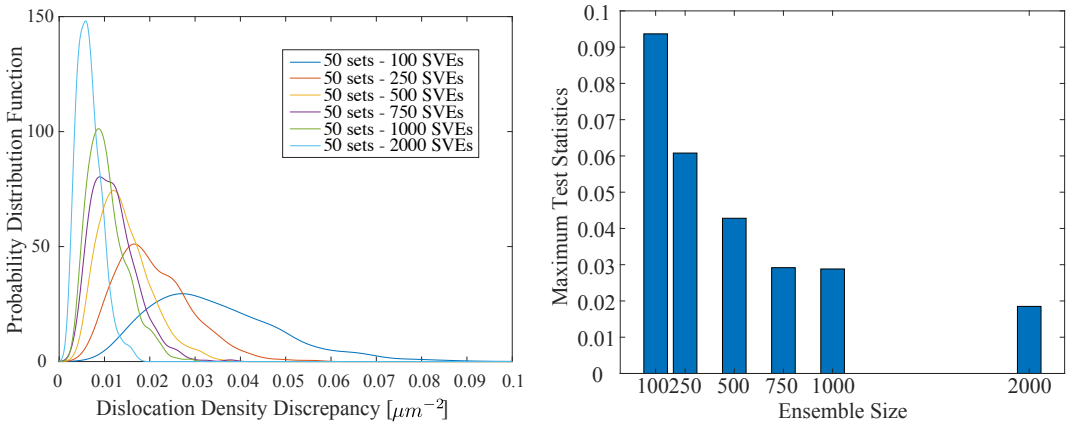

(a) (b)

Figure 5.7: (a) Distributions of D* with increasing number of SVEs, and (b) convergence of max D* with increasing number of SVEs.

tween any two sets of SVEs among the fifty sets. For any ensemble size, 1225 $D^\star$ are obtained through Eq. 5.24.

Applying the same loading and boundary conditions described in Section 5.4.2.2 to each SVE in the simulation pool, we obtained the D^3 for each SVE at load cycle ten. Construct the CDF of D^3 from simulation results, and the probability distribution of $D^\star$ between any two sets is plotted in Fig. 5.7a. It is clear that the increase of ensemble size reduces the variance of $D^\star$, which indicates the reduction of material aggregated behavior. The maximum $D^\star$ is extracted and plotted as a function of ensemble size, as shown in Fig. 5.7b. Increasing the ensemble size form 100 to 2000 significantly reduces the discrepancy between the aggregated D^3 distribution ($\sim 2\%$ error for 2000 SVEs). Note that as the ensemble size increases to 500, the range of $D^\star$ distribution has reduced to less than 5%.

5.5.2 Evolution of Dislocation Density Discrepancy

The evolution of local behavior, for example, D^3, is effected by the applied load amplitude and frequency due to load re-distributions induced by visco-plasticity. Ideally, the prediction of D^3 requires the execution of microscale forward model up to the number of

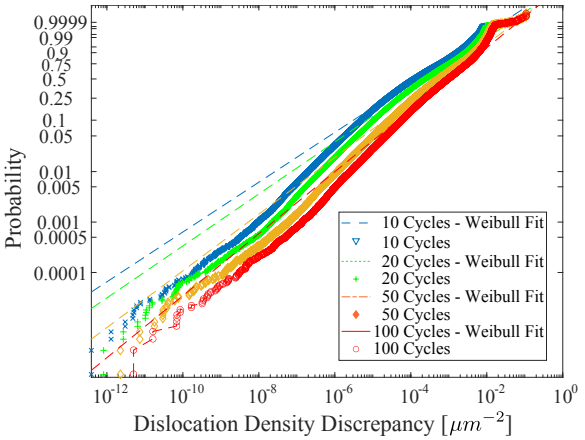

Figure 5.8: Motion of D^3 distribution.

cycle to failure. Even though the Sparse DD-EHM approach improved the computational efficiency and allowed us to simulate the material fatigue behavior to hundreds of cycles, it is still computational prohibitive to execute all 10,258 SVE simulations to the number of cycle to failure which is typically in the order of 10,000 cycles.

In the current chapter, five hundred SVEs selected to represent the 10,258 SVE pool based on the selection criterion that the the maximum $D^\star$ of the 500 SVEs is similar (the discrepancy is 0.3%). Cyclic loading, as shown in Section 5.4.2.2, is applied to these 500 SVEs up to 100 cycles. D^3 is assumed to be subject to a Weibull distribution at any given time instance, and the probability distribution for a Weibull random variable is expressed as:

$$f(x;\lambda,k) = \begin{cases} \frac{k}{\lambda}(\frac{x}{\lambda})^{k-1}\exp[-(\frac{x}{\lambda})^k] & x \geq 0 \\ 0 & x < 0 \end{cases} \tag{5.25}$$

where $k > 0$ is the shape parameter, and $\lambda > 0$ is the scale parameter. The distributions at 10 cycles, 20 cycles, 50 cycles and 100 cycles are shown in the probability plot (Figure 5.8). It is clearly seen that the Weibull distribution captures the tail of D^3 distribution for $D^3 > 10^{-5}$ at all time instances. The D^3 distributions are shifting to higher D^3 region with higher loading cycles.

To extend the prediction capability of D^3 distribution from 100 cycles to 10,000 cycles

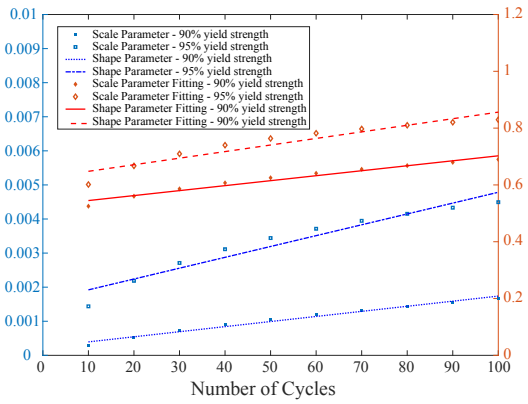

Figure 5.9: Temporal evolution of the shape and scale parameter.

or higher, an extrapolation technique is employed. The movement of D^3 distribution can be captured by simply varying the parameters of Weibull distribution, and the temporal evolution of shape parameter and scale parameter within the first 100 cycles is fitted to a linear curve, as shown in Fig. 5.9. The changing rates of shape and scale parameters are assumed to be constant, and therefore the evolution of D^3 distribution is predicted.

5.5.3 Critical Strength Distribution

Predicted D^3 distribution and P_f curve from experiments are employed to calibrate the probability distribution function of the critical D^3. The D^3 distribution at any time instance can be predicted by the extrapolated shape and scale parameter, and the P_f curve is constructed from available experimental data.

Researchers have measured the number of cycle to failure N_f for Ti-6242 at 95% yield stress. Fujishiro and Eylon [44] investigated the effect of Pt ion plating on the high cycle axial fatigue life of Ti-6242 specimens at room temperature and 455C. Measured number of cycle to failure at room temperature with and without Pt coat are employed in our study. Yuan et al. [191] studied the effects of surface roughness and residual stress induced by the mechanical polishing treatments (cold rolling polishing (CRP), sandpaper polishing (SP) andnylon cloth polishing (NCP)) on fatigue life. Sinha et al. [156] presented the results of

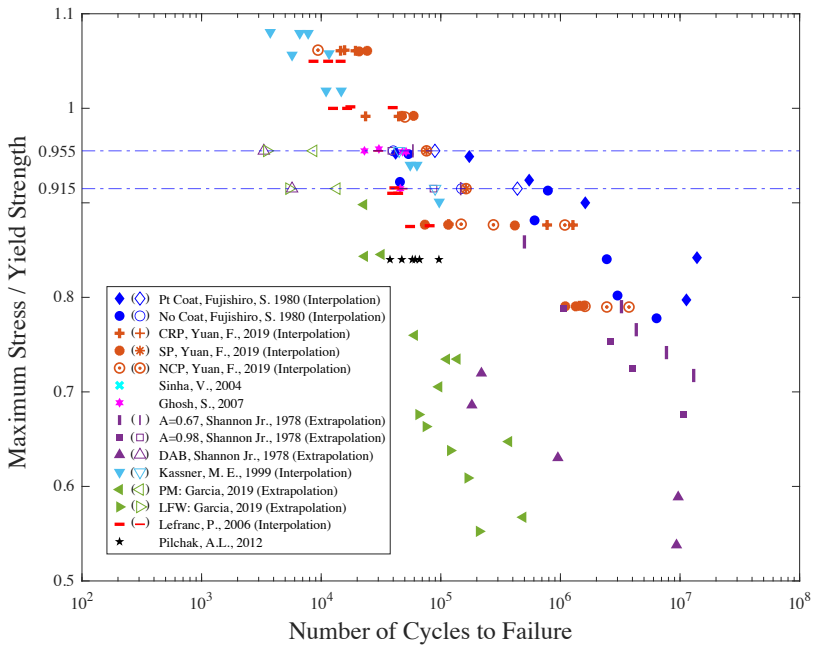

Figure 5.10: Experimental S-N data.

a study of the response of an β-forged Ti-6242y during static, normal-fatigue, and dwell-fatigue loading. Results under pure fatigue loading is employed in current study. Ghosh et al. [49] conducted pure fatigue and dwell fatigue tests with different test conditions (load ratio, dwell time and peak stress to yield strength ratio) for the three α/β-forged and one β-forged Ti-6242. Mich. [114] provided the fatigue properties of duplex annealed sheet at 70F and smooth rotating beam made of Ti-6242. However, available data points are limited to relative low stress level ($< 90\%yieldstress$). Pilchak et al. [128] performed fatigue test on both as-received samples and exposed samples at 80% yield strength. Kassner et al. [80] determined the low cycle fatigue properties and dwell low cycle fatigue properties for Ti-6242. Garcia and Morgeneyer [47] measured the fatigue life for the parent material (PM) and linear friction welds (LFW) of Ti-6242, and number of cycle to failure is observed mainly with stress less than 800 MPa. Lefranc et al. [91] focused the dwell effect on β-forged Ti-6242, but they also measured fatigue life for comparison. Above experimental data points, and number of cycle to failure estimated at 91.5% yield strength and 95.5% yield strength are plotted in stress-life plot in Fig. 5.10.

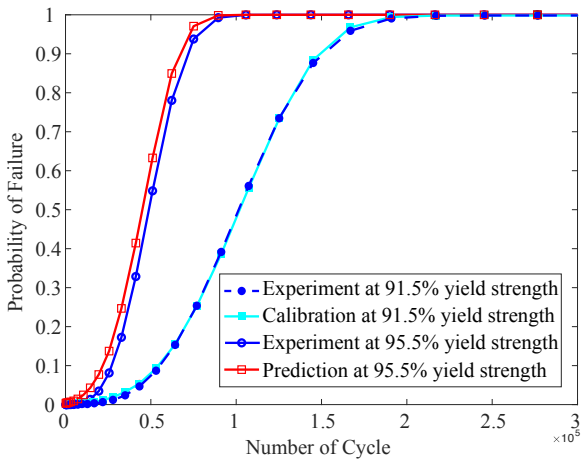

Figure 5.11: P_f calibration and prediction.

Employing the number of cycle to failure at 91.5% yield strength, the P_f curve can be constructed as shown in Fig. 5.11. To focus on the region where the P_f is small, bias calibration points are selected on the P_f curve to calibrate the strength distribution by comparing the predicted P_f and P_f from experiments. For any of the calibration point $(N_{f,i}, P_{f,i})$, the distribution of D^3 at $N_{f,i}$ is estimated through the evolving scale and shape parameters as shown in Fig. 5.9. The strength distribution is obtained through optimization algorithm. For each iteration, the residual is calculated by

$$R_{P_f} = \sqrt{R_1^2 + R_2^2 + ... + R_{n_{cp}}^2} \tag{5.26}$$

where R_i is the different between predicted P_f and experimental PDF at i^{th} calibration point. n_{cp} is the number of calibration points. The calibrated strength distribution and predicted D^3 distributions are plotted in Fig. 5.12. The motion of D^3 is represented every 10,000 cycles and up to 50,000 cycles.

The probabilistic distribution of the critical strength is taken as a material property and does not change at different loading amplitude. The calibrated critical strength distribution is employed to predict the probability of failure of Ti-6242 at 95.5% yield stress.

In Fig. 5.11, the predicted probability of failure at 95.5% yield strength is compared

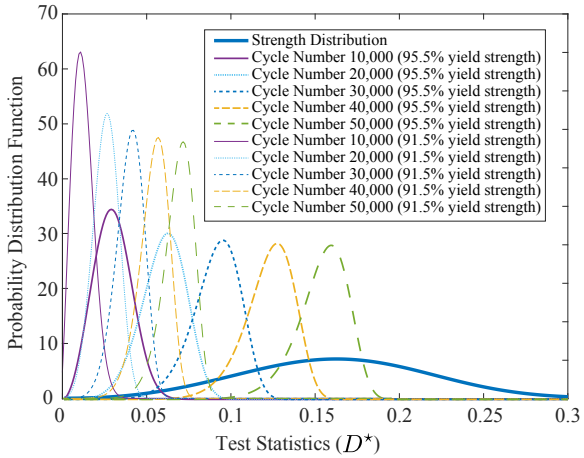

Figure 5.12: Distribution of D^3 and critical D^3.

with the experimental curve. At both stress levels, the probability of failure rise from 0 to 1 with the increasing loading cycles. The experimental curve is plotted based on the available data and interpolations. The predicted P_f curve is obtained by computing the intersection area between the D^3 prediction and calibrated critical D^3 distribution where the D^3 is higher than the critical value. The discrepancy between these two curves are also observed. For any given probability of failure, the discrepancy of cycle numbers is around 5,000 cycles. The critical D^3 distribution and the PDF of D^3 at 10,000, 20,000, 30,000, 40,000 and 50,000 cycles are presented in Fig. 5.11b. The PDF of D^3 at both stress levels move from near zero to large D^3 with the increasing of cycle number. Higher stress level leads to faster propagation of D^3 distribution and larger D^3 variation within the microstructure.

5.6 Conclusion

A uncertainty quantification framework has been proposed to predict the fatigue nucleation life for Ti-6242. The constitutive behavior of Ti-6242 is captured by a verified Sparse DD-EHM formulation [94]. The capability of microstructure generation and fatigue nucleation prediction has been developed. The critical FNP distribution is calibrated at 91.5% yield strength, and then employed to predict the probability of failure at 95.5%

yield strength. This framework provides the ability to quantify the effect of crystal orientation distribution, colony grain volume fraction and thickness of α/β lath within the Ti-6242 microstructure on the fatigue nucleation life.

Chapter 6

Conclusion

This dissertation has focused on the uncertainty quantification and sensitivity analysis of heterogeneous materials. The studies are devoted to understand and characterize the roles of different deformation and failure mechanisms at the microstructure scale. Particularly, energetic materials and a titanium alloy are investigated through the proposed analysis frameworks for the effect of material morphology and property parameters on material behavior under dynamic / fatigue loads. The key contributions of this dissertation are follows:

- *Investigation of the dynamic response of energetic materials through sensitivity analyses to quantify the contribution of material morphologies and properties in the microscale structure to material response under dynamic loading.*

    1. A parameter sensitivity analysis framework has been developed in the context of PBX microstructures subjected to transient loading. This framework is exercised to investigate: (1) the sensitivity of interfacial separation observed under impact loading to the parameters that describe the constitutive behavior of the binder and the interface, and (2) the sensitivity of temperature rise observed under the cyclic loading to the parameters that describe the particle size, shape and volume fraction. A piece-wise continuous GP model with SVM classier is proposed and employed to characterize sensitivities in the presence of response function discontinuities.

    2. Sensitivity analysis is performed to investigate the sensitivity of temperature rise under sub-shock loading to the monoclinic elasticity and crystal plasticities of β-HMX crystalline which is described by a CPFE model. The anisotropic

elasticity coefficients in the monoclinic crystalline have a modest effect on the energy dissipation and temperature rise dominated by sensitivities of a few coefficients. Among the two primary slip mechanisms, phonon drag appears dominant within the load rate amplitude regimes considered in this study.

3. Mechanical twinning behavior of crystalline β-HMX is investigated with respect to crystal orientation, microscale structure and loading amplitude under given shock/sub-shock impact through a large deformation CPFE framework. A strong crystal orientation dependency is observed in single crystal and polycrystal orientations. Compared with the more eralistic microstructure, the regularized structure generates lower peak twin volume fractiondue to the reduction of sharp corners of particles. Twinning phenomenon becomes more evident at higher strain rate which further highlights the importance of modeling twinning through a physically meaningful fashion.

- *Investigation of the effect of lamellar microstructure features on fatigue nucleation life of titanium alloy Ti-6242.*

  A uncertainty quantification framework is proposed to predict the fatigue nucleation life for Ti-6242. The lamellar microstructure of Ti-6242 is explicitly incorporated in the SVE simulations for the prediction of failure probability. The constitutive behavior of Ti-6242 is captured by a verified Sparse DD-EHM formulation. The critical FNP distribution is calibrated at 91.5% yield strength, and then employed to predict the probability of failure at 95.5% The effect of crystal orientation distribution, colony grain volume fraction and thickness of α/β lath within the Ti-6242 microstructure on the fatigue nucleation life is quantified at different stress levels through the probability of failure.

BIBLIOGRAPHY

[1] F. Appel, U. Lorenz, M. Oehring, U. Sparka, and R. J. M. S. Wagner. Thermally activated deformation mechanisms in micro-alloyed two-phase titanium amminide alloys. *Materials Science and Engineering: A*, 233(1-2):1–14, 1997.

[2] R. W. Armstrong. Dislocation-assisted initiation of energetic materials. *Central European Journal of Energetic Materials*, 2(3):21–37, 2005.

[3] R. W. Armstrong. Dislocation mechanics aspects of energetic material composites. *Rev. Adv. Mater. Sci*, 19:13–40, 2009.

[4] R. W. Armstrong, H. L. Ammon, Z. Y. Du, W. L. Elban, and X. J. Zhang. Energetic crystal-lattice-dependent responses. *MRS Online Proceedings Library Archive*, 296, 1992.

[5] P. J. Ashton, T.-S. Jun, Z. Zhang, T. B. Britton, A. M. Harte, S. B. Leen, and F. P. Dunne. The effect of the beta phase on the micromechanical response of dual-phase titanium alloys. *International Journal of Fatigue*, 100:377–387, 2017.

[6] R. A. Austin, N. R. Barton, W. M. Howard, and L. E. Fried. Modeling pore collapse and chemical reactions in shock-loaded hmx crystals. *Journal of Physics: Conference Series*, 500(5):052002, 2014.

[7] R. A. Austin, N. R. Barton, J. E. Reaugh, and L. E. Fried. Direct numerical simulation of shear localization and decomposition reactions in shock-loaded hmx crystal. *Journal of Applied Physics*, 117(18):185902, 2015.

[8] Ritwik Bandyopadhyay, Veerappan Prithivirajan, and Michael D Sangid. Uncertainty quantification in the mechanical response of crystal plasticity simulations. *JOM*, 71(8):2612–2624, 2019.

[9] N. R. Barton, J. Knap, A. Arsenlis, R. Becker, R. D. Hornung, and D. R. Jefferson. Embedded polycrystal plasticity and adaptive sampling. *International Journal of Plasticity*, 24(2):242–266, 2008.

[10] N. R. Barton, N. W. Winter, and J. E. Reaugh. Defect evolution and pore collapse in crystalline energetic materials. *Modelling and Simulation in Materials Science and Engineering*, 17(3):035003, 2009.

[11] A. Barua and M. Zhou. A lagrangian framework for analyzing microstructural level response of polymer-bonded explosives. *Modelling and Simulation in Materials Science and Engineering*, 19(5):055001, 2011.

[12] A. Barua, S. Kim, Y. Horie, and M. Zhou. Ignition criterion for heterogeneous energetic materials based on hotspot size-temperature threshold. *Journal of Applied Physics*, 113(6):064906, 2013.

[13] A. Barua, S. Kim, Y. Horie, and M. Zhou. Ignition criterion for heterogeneous energetic materials based on hotspot size-temperature threshold. *Journal of Applied Physics*, 113(6):064906, 2013.

[14] R. Becker. Effects of crystal plasticity on materials loaded at high pressures and strain rates. *International Journal of Plasticity*, 20(11):1983–2006, 2004.

[15] S. Beretta and Y. Murakami. Statistical analysis of defects for fatigue strength prediction and quality control of materials. *Fatigue & Fracture of Engineering Materials & Structures*, 21(9):1049–1065, 1998.

[16] R. R. Bernecker. Observations on the hugoniot for hmx. *In AIP Conference Proceedings*, 370(1):141–144, 1996.

[17] I. J. Beyerlein and C. N. Tomé. A dislocation-based constitutive law for pure zr

including temperature effects. *International Journal of Plasticity*, 24(5):867–895, 2008.

[18] F. Birch. Finite elastic strain of cubic crystals. *Physical review*, 71(11):809, 1947.

[19] F. P. Bowden and A. D. Yoffe. *Initiation and growth of explosion in liquids and solids*. CUP Archive, 1985.

[20] C. M. Cady, W. R. Blumenthal, G. T. Gray III, and D. J. Idar. Mechanical properties of plastic-bonded explosive binder materials as a function of strain-rate and temperature. *Polymer Engineering & Science*, 46(6):812–819, 2006.

[21] H. H. Cady. Growth and defects of explosives crystals. *MRS Online Proceedings Library Archive*, 296:243–254, 1992.

[22] G. M. Castelluccio and D. L. McDowell. Mesoscale modeling of microstructurally small fatigue cracks in metallic polycrystals. *Materials Science and Engineering: A*, 598:34–55, 2014.

[23] G. M. Castelluccio and D. L. McDowell. Microstructure and mesh sensitivities of mesoscale surrogate driving force measures for transgranular fatigue cracks in polycrystals. *Materials Science and Engineering: A*, 639:626–639, 2015.

[24] S. Chatterjee and A. S. Hadi. *Sensitivity analysis in linear regression*, volume 327. John Wiley & Sons, 2009.

[25] C. S. Choi and H. P. Boutin. A study of the crystal structure of β-cyclotetramethylene tetranitramine by neutron diffraction. *Acta Crystallographica Section B: Structural Crystallography and Crystal Chemistry*, 26(9):1235–1240, 1970.

[26] C. S. Coffey and J. Sharma. Lattice softening and failure in severely deformed molecular crystals. *Journal of Applied Physics*, 89(9):4797–4802, 2001.

[27] Peter C Collins, B Welk, T Searles, J Tiley, JC Russ, and HL Fraser. Development of methods for the quantification of microstructural features in α+ β-processed α/β titanium alloys. *Materials Science and Engineering: A*, 508(1-2):174–182, 2009.

[28] M. W. Conroy, I. I. Oleynik, S. V. Zybin, and C. T. White. First-principles anisotropic constitutive relationships in β-cyclotetramethylene tetranitramine (β-hmx). *Journal of Applied Physics*, 104(5):053506, 2008.

[29] N. Cristianini and J. Shawe-Taylor. *An introduction to support vector machines and other kernel-based learning methods*. Cambridge university press, 2000.

[30] H. Cui, G. Ji, X. Chen, Q. Zhang, D. Wei, and F. Zhao. Phase transitions and mechanical properties of octahydro-1, 3, 5, 7-tetranitro-1, 3, 5, 7-tetrazocine in different crystal phases by molecular dynamics simulation. *Journal of Chemical & Engineering Data*, 55(9):3121–3129, 2010.

[31] H. Czerski and W. G. Proud. Relationship between the morphology of granular cyclotrimethylene-trinitramine and its shock sensitivity. *Journal of Applied Physics*, 102(11):113515, 2007.

[32] H. Czerski and W. G. Proud. Relationship between the morphology of granular cyclotrimethylene-trinitramine and its shock sensitivity. *Journal of Applied Physics*, 102(11):113515, 2007.

[33] D. Deka, D. S. Joseph, S. Ghosh, and M. J. Mills. Crystal plasticity modeling of deformation and creep in polycrystalline ti-6242. *Metallurgical and materials transactions A*, 37(5):1371–1388, 2006.

[34] L. Delannay, P. J. Jacques, and S. R. Kalidindi. Finite element modeling of crystal plasticity with grains shaped as truncated octahedrons. *International Journal of Plasticity*, 22(10):1879–1898, 2006.

[35] C. Deng, X. Xue, Y. Chi, H. Li, X. Long, and C. Zhang. Nature of the enhanced self-heating ability of imperfect energetic crystals relative to perfect ones. *The Journal of Physical Chemistry C*, 121(22):12101–12109, 2017.

[36] J. R. Deschamps, M. Frisch, and D. Parrish. Thermal expansion of hmx. *Journal of Chemical Crystallography*, 41(7):966–970, 2011.

[37] J. J. Dick, D. E. Hooks, and R. Menikoff. Elastic–plastic wave profiles in cyclotetramethylene tetranitramine crystals. *Journal of Applied Physics*, 96(1):374–379, 2004.

[38] M. Elices, G. V. Guinea, J. Gomez, and J. Planas. The cohesive zone model: advantages, limitations and challenges. *Engineering Fracture Mechanics*, 69(2):137–163, 2002.

[39] A. Fatemi and D. F. Socie. A critical plane approach to multiaxial fatigue damage including out-of-phase loading. *Fatigue & Fracture of Engineering Materials & Structures*, 11(3):149–165, 1988.

[40] J. E. Field. Hot spot ignition mechanisms for explosives. *Accounts of chemical Research*, 25(11):489–496, 1992.

[41] H. Christopher Frey and S. R. Patil. Identification and review of sensitivity analysis methods. *Risk Analysis*, 22(3):553–578, 2002.

[42] H. Christopher Frey and S. R. Patil. Identification and review of sensitivity analysis methods. *Risk Analysis*, 22(3):553–578, 2002.

[43] H. J. Frost and M. F. Ashby. Motion of a dislocation acted on by a viscous drag through an array of discrete obstacles. *Journal of Applied Physics*, 42(13):5273–5279, 1971.

[44] S. Fujishiro and D. Eylon. Improvement of ti alloy fatigue properties by pt ion plating. *Metallurgical Transactions A*, 11(8):1259–1263, 1980.

[45] H. G. Gallagher, J. C. Miller, D. B. Sheen, J. N. Sherwood, and R. M. Vrcelj. Mechanical properties of β-hmx. *Chemistry Central Journal*, 9(1):22, 2015.

[46] Y. F. Gao and Z. Suo. The orientation of the self-assembled monolayer stripes on a crystalline substrate. *Journal of the Mechanics and Physics of Solids*, 51(1):147–167, 2003.

[47] J. M. Garcia and T. F. Morgeneyer. Strength and fatigue strength of a similar ti-6al-2sn-4zr-2mo-0.1 si linear friction welded joint. *Fatigue & Fracture of Engineering Materials & Structures*, 42(5):1100–1117, 2019.

[48] N. Gey, M. Humbert, M. J. Philippe, and Y. Combres. Modeling the transformation texture of ti-64 sheets after rolling in the β-field. *Materials Science and Engineering: A*, 230(1-2):68–74, 1997.

[49] S. Ghosh, M. Mills, S. Rokhlin, V. Sinha, W. Soboyejo, and J. Williams. The evaluation of cold dwell fatigue in ti-6242. *US Dept. of Transportation/Federal Aviation Authority report, DOT/FAA/AR-06/24*, 2007.

[50] Somnath Ghosh and Pritam Chakraborty. Microstructure and load sensitive fatigue crack nucleation in ti-6242 using accelerated crystal plasticity fem simulations. *International journal of fatigue*, 48:231–246, 2013.

[51] M. F. X. Gigliotti, B. P. Bewlay, J. B. Deaton, R. S. Gilmore, and G. A. Salishchev. Microstructure-ultrasonic inspectability relationships in ti6242: Signal-to-noise in fine-grain-processed ti6242. *Metallurgical and Materials Transactions A*, 31(9): 2119–2125, 2000.

[52] G. T. Gray, W. R. Blumenthal, D. J. Idar, and C. M. Cady. Influence of temperature on the high-strain-rate mechanical behavior of pbx 9501. *In Aip conference proceedings*, 429:583–586, 1998.

[53] N. Grilli and M. Koslowski. The effect of crystal orientation on shock loading of single crystal energetic materials. *Computational Materials Science*, 155:235–245, 2018.

[54] T. Gu, K. S. Stopka, C. Xu, and D. L. McDowell. Prediction of maximum fatigue indicator parameters for duplex ti–6al–4v using extreme value theory. *Acta Materialia*, 188:504–516, 2020.

[55] J. C. Gump and S. M. Peiris. Isothermal equations of state of beta octahydro-1, 3, 5, 7-tetranitro-1, 3, 5, 7-tetrazocine at high temperatures. *Journal of applied physics*, 97(5):053513, 2005.

[56] M. E. Gurtin and K. Spear. On the relationship between the logarithmic strain rate and the stretching tensor. *International Journal of Solids and Structures*, 19(5):437–444, 1983.

[57] G. Hackeling. *Mastering Machine Learning with scikit-learn*. Packt Publishing Ltd, 2017.

[58] B. Han, Y. Ju, and C. Zhou. Simulation of crack propagation in htpb propellant using cohesive zone model. *Engineering Failure Analysis*, 26:304–317, 2012.

[59] D. M. Hanson-Parr and T. P. Parr. Thermal properties measurements of solid rocket propellant oxidizers and binder materials as a function of temperature. *Journal of energetic materials*, 17(1):1–48, 1999.

[60] D. B. Hardin, J. J. Rimoli, and M. Zhou. Analysis of thermomechanical response

of polycrystalline hmx under impact loading through mesoscale simulations. *AIP Advances*, 4(9):097136, 2014.

[61] M. Herrmann, W. Engel, and N. Eisenreich. Thermal expansion, transitions, sensitivities and burning rates of hmx. *Propellants, Explosives, Pyrotechnics*, 17(4): 190–195, 1992.

[62] M. Hiratani and E. M. Nadgorny. Combined model of dislocation motion with thermally activated and drag-dependent stages. *Acta Materialia*, 49(20):4337–4346, 2001.

[63] A. Hoger. The stress conjugate to logarithmic strain. *International Journal of Solids and Structures*, 23(12):1645–1656, 1987.

[64] T. Homma and A. Saltelli. Importance measures in global sensitivity analysis of nonlinear models. *Reliability Engineering & System Safety*, 52(1):1–17, 1996.

[65] D. E. Hooks, D. B. Hayes, D. E. Hare, D. B. Reisman, K. S. Vandersall, J. W. Forbes, and C. A. Hall. Isentropic compression of cyclotetramethylene tetranitramine (hmx) single crystals to 50 gpa. *Journal of applied physics*, 99(12):124901, 2006.

[66] D. E. Hooks, K. J. Ramos, and A. R. Martinez. Elastic-plastic shock wave profiles in oriented single crystals of cyclotrimethylene trinitramine (rdx) at 2.25 gpa. *Journal of Applied Physics*, 100(2):024908, 2006.

[67] S.-W. Hsiao and N. Kikuchi. Numerical analysis and optimal design of composite thermoforming process. *Computer Methods in Applied Mechanics and Engineering*, 177(1-2):1–34, 1999.

[68] R. Hu, C. Prakash, V. Tomar, M. Harr, and I. E. Gunduzand C. Oskay. Experimentally-validated mesoscale modeling of the coupled mechanical–thermal

response of ap–htpb energetic material under dynamic loading. *International Journal of Fracture*, 203(1-2):277–298, 2017.

[69] R. J. Hudson, M. Moniruzzaman, and P. P. Gill. Investigation of crystal morphology and shock sensitivity of cyclotrimethylenetrinitramine suspension by rheology. *Propellants, Explosives, Pyrotechnics*, 40(2):233–237, 2015.

[70] R. L. Iman and J. C. Helton. An investigation of uncertainty and sensitivity analysis techniques for computer models. *Risk Analysis*, 8(1):71–90, 1988.

[71] M. Inoue and I. Hirasawa. The relationship between crystal morphology and XRD peak intensity on $CaSO_4 \cdot 2H_2O$. *Journal of Crystal Growth*, 380:169 – 175, 2013.

[72] T. L. Jackson, D. E. Hooks, and J. Buckmaster. Modeling the microstructure of energetic materials with realistic constituent morphology. *Propellants, Explosives, Pyrotechnics*, 36(3):252–258, 2011.

[73] A. Jain and S. R. Agnew. Modeling the temperature dependent effect of twinning on the behavior of magnesium alloy az31b sheet. *Materials Science and Engineering: A*, 462(1-2):29–36, 2007.

[74] N. Jia, F. Roters, P. Eisenlohr, C. Kords, and D. Raabe. Non-crystallographic shear banding in crystal plasticity fem simulations: Example of texture evolution in α-brass. *Acta Materialia*, 60(3):1099–1115, 2012.

[75] T. S. Jun, D. E. J. Armstrong, and T. B. Britton. A nanoindentation investigation of local strain rate sensitivity in dual-phase ti alloys. *Journal of Alloys and Compounds*, 672:282–291, 2016.

[76] T.-S. Jun, G. Sernicola, F. P. Dunne, and T. B. Britton. Local deformation mechanisms of two-phase ti alloy. *Materials Science and Engineering: A*, 649:39–47, 2016.

[77] S. R. Kalidindi. Incorporation of deformation twinning in crystal plasticity models. *Journal of the Mechanics and Physics of Solids*, 46(2):267–290, 1998.

[78] S. R. Kalidindi. Modeling anisotropic strain hardening and deformation textures in low stacking fault energy fcc metals. *International Journal of Plasticity*, 17(6): 837–860, 2001.

[79] M. Kamiński. On probabilistic fatigue models for composite materials. *International journal of fatigue*, 24(2-4):477–495, 2002.

[80] M. E. Kassner, Y. Kosaka, and J. S. Hall. Low-cycle dwell-time fatigue in ti-6242. *Metallurgical and Materials Transactions A*, 30(9):2383–2389, 1999.

[81] S. W. Key. Grüneisen tensor for anisotropic materials. *Journal of Applied Physics*, 38(7):2923–2928, 1967.

[82] M. Khan, A. Pal, and C. R. Picu. Dislocation mobility and critical stresses at finite temperatures in molecular crystal cyclotetramethylene tetranitramine (beta-hmx). *Modelling and Simulation in Materials Science and Engineering*, 26(8):085009, 2018.

[83] K. Kitayama, C. N. Tomé, E. F. Rauch, J. J. Gracio, and F. Barlat. A crystallographic dislocation model for describing hardening of polycrystals during strain path changes. application to low carbon steels. *International Journal of Plasticity*, 46:54–69, 2013.

[84] R. Kohavi. A study of cross-validation and bootstrap for accuracy estimation and model selection. In *Ijcai*, volume 14, pages 1137–1145. Stanford, CA, 1995.

[85] Shravan Kotha, Deniz Ozturk, and Somnath Ghosh. Uncertainty-quantified parametrically homogenized constitutive models (uq-phcms) for dual-phase α/β titanium alloys. *npj Computational Materials*, 6(1):1–20, 2020.

[86] S. B. Kotsiantis, I. Zaharakis, and P. Pintelas. Supervised machine learning: A review of classification techniques. *Emerging artificial intelligence applications in computer engineering*, 160(1):3–24, 2007.

[87] N. V. Kozyrev, B. V. Larionov, and G. V. Sakovich. Influence of HMX particle size on the synthesis of nanodiamonds in detonation waves. *Combustion, Explosion, and Shock Waves*, 44(2):193–197, 2008.

[88] A. C. Landerville, M. W. Conroy, M. M. Budzevich, Y. Lin, C. T. White, and I. I. Oleynik. Equations of state for energetic materials from density functional theory with van der waals, thermal, and zero-point energy corrections. *Applied Physics Letters*, 97(25):251908, 2010.

[89] J. Le and Z. P. Bažant. Unified nano-mechanics based probabilistic theory of quasibrittle and brittle structures: Ii. fatigue crack growth, lifetime and scaling. *Journal of the Mechanics and Physics of Solids*, 59(7):1322–1337, 2011.

[90] K. Y. Lee, R. Gilardi, K. H. Liebenberg, R. W. Armstrong, and J. J. Gilman. Structure and properties of energetic materials. *Research Society, Pittsburgh, PA*, 296:237, 1993.

[91] P. Lefranc, C. Sarrazin-Baudoux, and V. Doquet. Dwell-fatigue behaviour of a beta-forged ti 6242 alloy. In *Fracture of Nano and Engineering Materials and Structures*, pages 171–172. Springer, 2006.

[92] G. Li, H. Rabitz, P. E. Yelvington, O. O. Oluwole, F. Bacon, C. E. Kolb, and J. Schoendorf. Global sensitivity analysis for systems with independent and/or correlated inputs. *The journal of physical chemistry A*, 114(19):6022–6032, 2010.

[93] Yang Liu, Yiguo Zhu, Caglar Oskay, Ping Hu, Liang Ying, and Dantong Wang. Experimental and computational study of microstructural effect on ductile fracture

of hot-forming materials. *Materials Science and Engineering: A*, 724:298–323, 2018.

[94] Yang Liu, Xiang Zhang, Yiguo Zhu, Ping Hu, and Caglar Oskay. Dislocation density informed eigenstrain based reduced order homogenization modeling: Verification and application on a titanium alloy structure subjected to cyclic loading. *Modelling and Simulation in Materials Science and Engineering*, 28(2):025004, 2020.

[95] S. Lucarini and J. Segurado. An upscaling approach for micromechanics based fatigue: from rves to specimens and component life prediction. *International Journal of Fracture*, pages 1–16, 2019.

[96] D. A. Lucca, M. J. Klopfstein, O. R. Mejia, L. Rossettini, and L. T. DeLuca. Investigation of ammonium perchlorate by nanoindentation. *Materials science and technology*, 22(4):396–401, 2006.

[97] GERD Lütjering. Influence of processing on microstructure and mechanical properties of (α+ β) titanium alloys. *Materials Science and Engineering: A*, 243(1-2): 32–45, 1998.

[98] R. Madec, B. Devincre, and L. P. Kubin. From dislocation junctions to forest hardening. *Physical review letters*, 89(25):255508, 2002.

[99] S. Mahajan and G. Y. Chin. Formation of deformation twins in fcc crystals. *Acta metallurgica*, 21(10):1353–1363, 1973.

[100] E. B. Marin. On the formulation of a crystal plasticity model. Technical report, Sandia National Laboratories, 2006.

[101] E. B. Marin and P. R. Dawson. On modelling the elasto-viscoplastic response of metals using polycrystal plasticity. *Computer Methods in Applied Mechanics and Engineering*, 165(1-4):1–21, 1998.

[102] S. P. Marsh. *LASL shock Hugoniot data*, volume 5. Univ of California Press, 1980.

[103] N. Mathew and R. C. Picu. Slip asymmetry in the molecular crystal cyclotrimethylenetrinitramine. *Chemical Physics Letters*, 582:78–81, 2013.

[104] N. Mathew and T. Sewell. Pressure-dependent elastic coefficients of β-hmx from molecular simulations. *Propellants, Explosives, Pyrotechnics*, 43(3):223–227, 2018.

[105] S. Matthies and H. R. Wenk. Transformations for monoclinic crystal symmetry in texture analysis. *Journal of Applied Crystallography*, 42(4):564–571, 2009.

[106] F. McBagonluri, E. Akpan, C. Mercer, W. Shen, and W. O. Soboyejo. An investigation of the effects of microstructure on dwell fatigue crack growth in ti-6242. *Materials Science and Engineering: A*, 405(1-2):111–134, 2005.

[107] H. Mecking and U. F. Kocks. Kinetics of flow and strain-hardening. *Acta Metallurgica*, 29(11):1865–1875, 1981.

[108] H. Mecking and U. F. Kocks. Kinetics of flow and strain-hardening. *Acta metallurgica*, 29(11):1865–1875, 1981.

[109] H. Mecking, U. F. Kocks, and H. Fischer. Hardening, recovery, and creep in fcc mono-and polycrystals. In *Presented at the 4th Intern. Conf. on Strength of Metals and Alloys, Nancy, 30 Aug.-3 Sep. 1976*, 1976.

[110] R. Menikoff and E. Kober. Compaction waves in granular hmx. In *AIP Conference Proceedings*, volume 505, pages 397–400. AIP, 2000.

[111] R. Menikoff and T. D. Sewell. Fitting forms for isothermal data. *International Journal of High Pressure Research*, 21(2):121–138, 2001.

[112] R. Menikoff, J. J. Dick, and D. E.Hooks. Analysis of wave profiles for single-crystal cyclotetramethylene tetranitramine. *Journal of Applied Physics*, 97(2):023529, 2005.

[113] M. A. Meyers, O. Vöhringer, and V. A. Lubarda. The onset of twinning in metals: a constitutive description. *Acta materialia*, 49(19):4025–4039, 2001.

[114] Mechanical Properties Data Center Traverse City Mich. *Aerospace Structural Metals Handbook. Volume III.* Defense Technical Information Center, 1972. URL https://books.google.com/books?id=Y45vSwAACAAJ.

[115] J. K. Miller, J. O. Mares, I. E. Gunduz, S. F. Son, and J. F. Rhoads. The impact of crystal morphology on the thermal responses of ultrasonically-excited energetic materials. *Journal of Applied Physics*, 119(2):024903, 2016.

[116] J. K. Miller, J. O. Mares, I. E. Gunduz, S. F. Son, and J. F. Rhoads. The impact of crystal morphology on the thermal responses of ultrasonically-excited energetic materials. *Journal of Applied Physics*, 119(2):024903, 2016.

[117] M. D. Morris. Factorial sampling plans for preliminary computational experiments. *Technometrics*, 33(2):161–174, 1991.

[118] S. Naka, A. Lasalmonie, P. Costa, and L. P. Kubin. The low-temperature plastic deformation of α-titanium and the core structure of a-type screw dislocations. *Philosophical Magazine A*, 57(5):717–740, 1988.

[119] E. Nes. Modelling of work hardening and stress saturation in fcc metals. *Progress in Materials Science*, 41(3):129–193, 1997.

[120] J. Neyman. On the two different aspects of the representative method: the method of stratified sampling and the method of purposive selection. In *Breakthroughs in Statistics*, pages 123–150. Springer, 1992.

[121] B. Olinger, B. Roof, and H. Cady. The linear and volume compression of β-hmx and rdx. In *Actes du Symposium International sur le Comportement des Milieux Denses*

Sous Hautes Pressions Dynamiques, pages 3–8. Commissariat a l'Energie Atomique Paris, 1978.

[122] A. Pal and C. R. Picu. Peierls–nabarro stresses of dislocations in monoclinic cyclotetramethylene tetranitramine (β-hmx). *Modelling and Simulation in Materials Science and Engineering*, 26(4):045005, 2018.

[123] A. Pal and C. R. Picu. Non-schmid effect of pressure on plastic deformation in molecular crystal hmx. *Journal of Applied Physics*, 125(21):215111, 2019.

[124] S. J. P. Palmer and J. E. Field. The deformation and fracture of β-hmx. *Proc. R. Soc. Lond. A*, 383(1785):399–407, 1982.

[125] R Panchadhara and KA Gonthier. Mesoscale analysis of volumetric and surface dissipation in granular explosive induced by uniaxial deformation waves. *Shock Waves*, 21(1):43–61, 2011.

[126] D. Pelleg and A. W. Moore. X-means: Extending k-means with efficient estimation of the number of clusters. In *Icml*, volume 1, pages 727–734, 2000.

[127] Q. Peng, G. Wang, G. R. Liu, and S. De. Structures, mechanical properties, equations of state, and electronic properties of β-hmx under hydrostatic pressures: a dft-d2 study. *Physical Chemistry Chemical Physics*, 16(37):19972–19983, 2014.

[128] A. L. Pilchak, W. J. Porter, and R. John. Room temperature fracture processes of a near-α titanium alloy following elevated temperature exposure. *Journal of Materials Science*, 47(20):7235–7253, 2012.

[129] ICSU Scientific Freedom Policy. International tables for crystallography volume a: Space-group symmetry. *Acta Cryst*, 2013.

[130] C. Prakash, D. Verma, M. Exner, E. Gunduz, and V. Tomar. Strain rate dependent

failure of interfaces examined via nanoimpact experiments. In *Challenges in Mechanics of Time Dependent Materials, Volume 2*, pages 93–102. Springer, 2017.

[131] C. Prakash, I. E. Gunduz, C. Oskay, and V. Tomar. Effect of interface chemistry and strain rate on particle-matrix delamination in an energetic material. *Engineering Fracture Mechanics*, 191:46–64, 2018.

[132] G. Proust, C. N. Tomé, and G. C. Kaschner. Modeling texture, twinning and hardening evolution during deformation of hexagonal materials. *Acta Materialia*, 55(6): 2137–2148, 2007.

[133] G. Proust, C. N. Tomé, A. Jain, and S. R. Agnew. Modeling the effect of twinning and detwinning during strain-path changes of magnesium alloy az31. *International Journal of Plasticity*, 25(5):861–880, 2009.

[134] C. P. Przybyla and D. L. McDowell. Simulated microstructure-sensitive extreme value probabilities for high cycle fatigue of duplex ti–6al–4v. *International Journal of Plasticity*, 27(12):1871–1895, 2011.

[135] J. K. Qiu, Y. J. Ma, J. F. Lei, Y. Y. Liu, A. J. Huang, D. Rugg, and R. Yang. A comparative study on dwell fatigue of ti-6al-2sn-4zr-xmo (x= 2 to 6) alloys on a microstructure-normalized basis. *Metallurgical and Materials Transactions A*, 45 (13):6075–6087, 2014.

[136] R. Quey, P. R. Dawson, and F. Barbe. Large-scale 3d random polycrystals for the finite element method: Generation, meshing and remeshing. *Computer Methods in Applied Mechanics and Engineering*, 200(17-20):1729–1745, 2011.

[137] H. Rabitz, M. Kramer, and D. Dacol. Sensitivity analysis in chemical kinetics. *Annual Review of Physical Chemistry*, 34(1):419–461, 1983.

[138] P. J. Rae, H. T. Goldrein, S. J. P. Palmer, J. E. Field, and A. L. Lewis. Quasi–static studies of the deformation and failure of β–hmx based polymer bonded explosives. In *Proceedings of the Royal Society of London A: Mathematical, Physical and Engineering Sciences*, volume 458, pages 743–762. The Royal Society, 2002.

[139] P. J. Rae, H. T. Goldrein, S. J. P. Palmer, J. E. Field, and A. L. Lewis. Quasi–static studies of the deformation and failure of beta-hmx based polymer bonded explosives. *Proceedings of the Royal Society of London A: Mathematical, Physical and Engineering Sciences*, 458(2019):743–762, 2002.

[140] E. Rohan and B. Miara. Homogenization and shape sensitivity of microstructures for design of piezoelectric bio-materials. *Mechanics of Advanced Materials and Structures*, 13(6):473–485, 2006.

[141] F. Roters, P. Eisenlohr, L. Hantcherli, D. D. Tjahjanto, T. R. Bieler, and D. Raabe. Overview of constitutive laws, kinematics, homogenization and multiscale methods in crystal plasticity finite-element modeling: Theory, experiments, applications. *Acta Materialia*, 58(4):1152–1211, 2010.

[142] P. J. Rousseeuw. Silhouettes: a graphical aid to the interpretation and validation of cluster analysis. *Journal of computational and applied mathematics*, 20:53–65, 1987.

[143] Y. Sakamoto, M. Ishiguro, and G. Kitagawa. Akaike information criterion statistics. *Dordrecht, The Netherlands: D. Reidel*, 81, 1986.

[144] A. Saltelli and P. Annoni. How to avoid a perfunctory sensitivity analysis. *Environmental Modelling & Software*, 25(12):1508–1517, 2010.

[145] A. Saltelli, K. Chan, and E. M. Scott. *Sensitivity analysis*, volume 1. Wiley New York, 2000.

[146] A. Saltelli, M. Ratto, T. Andres, F. Campolongo, J. Cariboni, D. Gatelli, M. Saisana, and S. Tarantola. *Global sensitivity analysis: the primer*. John Wiley & Sons, 2008.

[147] F. Sansoz and H. Ghonem. Effects of loading frequency on fatigue crack growth mechanisms in α/β ti microstructure with large colony size. *Materials Science and Engineering: A*, 356(1-2):81–92, 2003.

[148] F. Schneider, T. Fellner, J. Wilde, and U. Wallrabe. Mechanical properties of silicones for mems. *Journal of Micromechanics and Microengineering*, 18(6):065008, 2008.

[149] B. Scholkopf, S. Mika, C. J. C. Burges, P. Knirsch, K.-R. Muller, G. Ratsch, and A. J. Smola. Input space versus feature space in kernel-based methods. *IEEE Transactions on Neural Networks*, 10(5):1000–1017, 1999.

[150] K. W. Schuler and J. W. Nunziato. The dynamic mechanical behavior of polymethyl methacrylate. *Rheologica Acta*, 13(2):265–273, 1974.

[151] P. Seuntjens, D. Mallants, J. Šimůnek, J. Patyn, and D.Jacques. Sensitivity analysis of physical and chemical properties affecting field-scale cadmium transport in a heterogeneous soil profile. *Journal of Hydrology*, 264(1-4):185–200, 2002.

[152] T. D. Sewell, D. Bedrov, R. Menikoff, and G. D. Smith. Elastic properties of hmx. In *AIP Conference Proceedings*, volume 620, pages 399–402. AIP, 2002.

[153] T. D. Sewell, R. Menikoff, D. Bedrov, and G. D. Smith. A molecular dynamics simulation study of elastic properties of hmx. *The Journal of Chemical Physics*, 119 (14):7417–7426, 2003.

[154] J. Sharma, R. W. Armstrong, W. L. Elban, C. S. Coffey, and H. W. Sandusky. Nanofractography of shocked rdx explosive crystals with atomic force microscopy. *Applied Physics Letters*, 78(4):457–459, 2001.

[155] J Sieniawski, W Ziaja, K Kubiak, and M Motyka. Microstructure and mechanical properties of high strength two-phase titanium alloys. *Titanium Alloys-Advances in Properties Control*, pages 69–80, 2013.

[156] V. Sinha, M. J. Mills, and J. C. Williams. Understanding the contributions of normal-fatigue and static loading to the dwell fatigue in a near-alpha titanium alloy. *Metallurgical and Materials Transactions A*, 35(10):3141–3148, 2004.

[157] C. B. Skidmore, D. S. Phillips, S. F. Son, and B. W. Asay. Characterization of hmx particles in pbx 9501. In *AIP Conference Proceedings*, volume 429, pages 579–582. AIP, 1998.

[158] I. M. Sobol'. On the distribution of points in a cube and the approximate evaluation of integrals. *Zhurnal Vychislitel'noi Matematiki i Matematicheskoi Fiziki*, 7(4):784–802, 1967.

[159] I. M. Sobol. Sensitivity estimates for nonlinear mathematical models. *Mathematical Modelling and Computational Experiments*, 1(4):407–414, 1993.

[160] S. H. Song, G. H. Paulino, and W. G. Buttlar. A bilinear cohesive zone model tailored for fracture of asphalt concrete considering viscoelastic bulk material. *Engineering Fracture Mechanics*, 73(18):2829–2848, 2006.

[161] D. C. Sorescu, B. M. Rice, and D. L. Thompson. Theoretical studies of the hydrostatic compression of rdx, hmx, hniw, and petn crystals. *The Journal of Physical Chemistry B*, 103(32):6783–6790, 1999.

[162] M. L. Stein. *Interpolation of spatial data: some theory for kriging*. Springer Science & Business Media, 2012.

[163] L. L. Stevens and C. J. Eckhardt. The elastic constants and related properties of β-

hmx determined by brillouin scattering. *The Journal of Chemical Physics*, 122(17): 174701, 2005.

[164] V. Studer, G. Hang, A. Pandolfi, M. Ortiz, W. French Anderson, and S. R. Quake. Scaling properties of a low-actuation pressure microfluidic valve. *Journal of applied physics*, 95(1):393–398, 2004.

[165] B. Sun, J. M. Winey, Y. M. Gupta, and D. E. Hooks. Determination of second-order elastic constants of cyclotetramethylene tetranitramine (β-hmx) using impulsive stimulated thermal scattering. *Journal of Applied Physics*, 106(5):053505, 2009.

[166] J. A. K. Suykens and J. Vandewalle. Least squares support vector machine classifiers. *Neural Processing Letters*, 9(3):293–300, 1999.

[167] B. C. Taylor, J. L. Stott, M. A. Thurmond, and J. P. Picanso. Alteration in lymphocyte subpopulations in bovine leukosis virus-infected cattle. *Veterinary Immunology and Immunopathology*, 31(1-2):35–47, 1992.

[168] U. Teipel. *Energetic materials: particle processing and characterization*. John Wiley & Sons, 2006.

[169] C. N. Tomé, P. J. Maudlin, R. A. Lebensohn, and G. C. Kaschner. Mechanical response of zirconium—i. derivation of a polycrystal constitutive law and finite element analysis. *Acta Materialia*, 49(15):3085–3096, 2001.

[170] E. Tufte and P. G. Morris. The visual display of quantitative information.; 1983, 2014.

[171] Viggo V. Tvergaard and J. W. Hutchinson. The influence of plasticity on mixed mode interface toughness. *Journal of the Mechanics and Physics of Solids*, 41(6): 1119–1135, 1993.

[172] B. Viguier, K. J. Hemker, J. Bonneville, F. Louchet, and J.-L. Martin. Modelling the flow stress anomaly in γ-tial i. experimental observations of dislocation mechanisms. *Philosophical Magazine A*, 71(6):1295–1312, 1995.

[173] G. Z. Voyiadjis and F. H. Abed. Effect of dislocation density evolution on the thermomechanical response of metals with different crystal structures at low and high strain rates and temperatures. *Archives of Mechanics*, 57(4):299–343, 2005.

[174] H. Wadell. Volume, shape, and roundness of quartz particles. *The Journal of Geology*, 43(3):250–280, 1935.

[175] S. Waheed, Z. Zheng, D. S. Balint, and P. E. Dunne. Microstructural effects on strain rate and dwell sensitivity in dual-phase titanium alloys. *Acta Materialia*, 162: 136–148, 2019.

[176] S. M. Walley, J. E. Field, and M. W. Greenaway. Crystal sensitivities of energetic materials. *Materials Science and Technology*, 22(4):402–413, 2006.

[177] D. J. Walters, D. J. Luscher, J. D. Yeager, and B. M. Patterson. Investigating deformation and mesoscale void creation in hmx based composites using tomography based grain scale fem. In *AIP Conference Proceedings*, volume 1979, page 070031. AIP Publishing LLC, 2018.

[178] D. X. Wang, S. S. Chen, Y. Y. Li, J. Y. Yang, T. Y. Wei, and S. H. Jin. An investigation into the effects of additives on crystal characteristics and impact sensitivity of RDX. *Journal of Energetic Materials*, 32(3):184–198, 2014.

[179] H. Wang, P. D. Wu, J. Wang, and C.N. Tomé. A crystal plasticity model for hexagonal close packed (hcp) crystals including twinning and de-twinning mechanisms. *International Journal of Plasticity*, 49:36–52, 2013.

[180] X. Wang, Y. Wu, F. Huang, T. Jiao, and R. J. Clifton. Mesoscale thermal-mechanical analysis of impacted granular and polymer-bonded explosives. *Mechanics of Materials*, 99:68–78, 2016.

[181] X. Wang, Y. Wu, F. Huang, T. Jiao, and R. J. Clifton. Mesoscale thermal-mechanical analysis of impacted granular and polymer-bonded explosives. *Mechanics of Materials*, 99:68 – 78, 2016.

[182] X. Wang, Y. Wu, and F. L. Huang. Thermal–mechanical–chemical responses of polymer-bonded explosives using a mesoscopic reactive model under impact loading. *Journal of hazardous materials*, 321:256–267, 2017.

[183] B. W. White and C. M. Tarver. Ignition and growth modeling of detonation reaction zone experiments on single crystals of petn and hmx. *In AIP Conference Proceedings*, 1793(1):030001, 2017.

[184] R. E. Winter and J. E. Field. The role of localized plastic flow in the impact initiation of explosives. *Proceedings of the Royal Society of London A: Mathematical, Physical and Engineering Sciences*, 343(1634):399–413, 1975.

[185] Y. Wu and F. Huang. Thermal mechanical anisotropic constitutive model and numerical simulations for shocked β-hmx single crystals. *European Journal of Mechanics-A/Solids*, 36:66–82, 2012.

[186] Y. Wu and F. L. Huang. A thermal-mechanical constitutive model for β-hmx single crystal and cohesive interface under dynamic high pressure loading. *Science China Physics, Mechanics and Astronomy*, 53(2):218–226, 2010.

[187] W. Yan-Qing and H. Feng-Lei. A micromechanical model for predicting combined damage of particles and interface debonding in pbx explosives. *Mechanics of Materials*, 41(1):27–47, 2009.

[188] J. D. Yeager, A. L. Higginbotham Duque, M. Shorty, P. R. Bowden, and J. A. Stull. Development of inert density mock materials for hmx. *Journal of Energetic Materials*, 36(3):253–265, 2018.

[189] C.S. Yoo and H. Cynn. Equation of state, phase transition, decomposition of β-hmx (octahydro-1, 3, 5, 7-tetranitro-1, 3, 5, 7-tetrazocine) at high pressures. *The Journal of Chemical Physics*, 111(22):10229–10235, 1999.

[190] M. Yu, P. Zhu, and Y. Ma. Global sensitivity analysis for the elastic properties of hollow spheres filled syntactic foams using high dimensional model representation method. *Computational Materials Science*, 61:89–98, 2012.

[191] F. Yuan, C. Liu, H. Gu, F. Han, Y. Zhang, M. Ali, and G. Li. Effects of mechanical polishing treatments on high cycle fatigue behavior of ti-6al-2sn-4zr-2mo alloy. *International Journal of Fatigue*, 121:55–62, 2019.

[192] A. R. Zamiri and S. De. Deformation distribution maps of β-hmx molecular crystals. *Journal of Physics D: Applied Physics*, 43(3):035404, 2010.

[193] A. R. Zamiri and S. De. Modeling the anisotropic deformation response of β-hmx molecular crystals. *Propellants, Explosives, Pyrotechnics*, 36(3):247–251, 2011.

[194] J. M. Zaug. Elastic constants of β-hmx and tantalum, equations of state of supercritical fluids and fluid mixtures and thermal transport determinations. In *Proceedings of the 11th Detonation Symposium*, volume 498, 1998.

[195] J. M. Zaug, M. R. Armstrong, J. C. Crowhurst, L. Feranti, R. Swan, R. Gross, N. E. Teshlich, M. Wall, R. A. Austin, and L. E. Fried. Ultrafast dynamic response of single crystal petn and beta-hmx. *No. LLNL-CONF-656341. Lawrence Livermore National Lab.*, 2014.

[196] J. M. Zaug, R. A. Austin, M. R. Armstrong, J. C. Crowhurst, N. Goldman, L. Ferranti, C. K. Saw, R. A. Swan, R. Gross, and L. E. Fried. Ultrafast dynamic response of single-crystal β-hmx (octahydro-1, 3, 5, 7-tetranitro-1, 3, 5, 7-tetrazocine). *Journal of Applied Physics*, 123(20):205902, 2018.

[197] M. Zecevic and M. Knezevic. A dislocation density based elasto-plastic self-consistent model for the prediction of cyclic deformation: Application to aa6022-t4. *International Journal of Plasticity*, 72:200–217, 2015.

[198] X. Zhang and C. Oskay. Material and morphology parameter sensitivity analysis in particulate composite materials. *Computational Mechanics*, 62(3):543–561, 2018.

[199] X. Zhang and C. Oskay. Plastic dissipation sensitivity to mechanical properties in polycrystalline β-hmx subjected to impact loading. *Mechanics of Materials*, ?(?):?, 2019.

[200] Xiang Zhang and Caglar Oskay. Eigenstrain based reduced order homogenization for polycrystalline materials. *Computer Methods in Applied Mechanics and Engineering*, 297:408–436, 2015.

[201] Xiang Zhang and Caglar Oskay. Sparse and scalable eigenstrain-based reduced order homogenization models for polycrystal plasticity. *Computer Methods in Applied Mechanics and Engineering*, 326:241–269, 2017.

[202] Xiaoyu Zhang and Caglar Oskay. Material and morphology parameter sensitivity analysis in particulate composite materials. *Computational Mechanics*, 62(3):543–561, 2018.

[203] Xiaoyu Zhang and Caglar Oskay. Plastic dissipation sensitivity to mechanical properties in polycrystalline β-hmx subjected to impact loading. *Mechanics of Materials*, 138:103079, 2019.

[204] Z. Zhang and F. P. Dunne. Microstructural heterogeneity in rate-dependent plasticity of multiphase titanium alloys. *Journal of the Mechanics and Physics of Solids*, 103: 199–220, 2017.

[205] Z. Zhang and F. P. Dunne. Phase morphology, variants and crystallography of alloy microstructures in cold dwell fatigue. *International Journal of Fatigue*, 113:324–334, 2018.

[206] Z. Zhou, P. Chen, F. Huang, and S. Liu. Experimental study on the micromechanical behavior of a PBX simulant using SEM and digital image correlation method. *Optics and Lasers in Engineering*, 49(3):366 – 370, 2011.

[207] S. Zhu, H. Huang, W. Peng, H. Wang, and S. Mahadevan. Probabilistic physics of failure-based framework for fatigue life prediction of aircraft gas turbine discs under uncertainty. *Reliability Engineering & System Safety*, 146:1–12, 2016.

[208] T. I. Zohdi. Modeling and simulation of laser processing of particulate-functionalized materials. *Archives of Computational Methods in Engineering*, 24 (1):89–113, 2017.